

---

# Modeling Light-Field-Controlled Electron Motion in Atoms and Solids

Michael Korbman

---



München



---

# **Modeling Light-Field-Controlled Electron Motion in Atoms and Solids**

**Michael Korbman**

---

Dissertation  
an der Fakultät für Physik  
der Ludwig–Maximilians–Universität  
München

vorgelegt von  
Michael Korbman  
aus Mailand, Italien

München, den 23. Juli 2012

Erstgutachter: Prof. Dr. Ferencz Krausz

Zweitgutachter: Prof. Dr. Armin Scrinzi

Tag der mündlichen Prüfung: 4. September 2012

# Contents

<b>Abstract</b>	<b>ix</b>
<b>Introduction</b>	<b>1</b>
<b>1 Overview of Atomic Ionization</b>	<b>5</b>
1.1 The Time Dependent Schrödinger Equation . . . . .	5
1.2 S-matrix Approach . . . . .	6
1.3 Length and Velocity Gauge . . . . .	7
1.4 Electrons in a Coulomb Potential . . . . .	10
1.4.1 Hydrogenic Wavefunctions . . . . .	10
1.4.2 Phases of Coulomb Wavefunctions . . . . .	11
1.4.3 Scattering States . . . . .	12
1.5 Electrons in a Homogeneous Time-Dependent Electric Field . . . . .	14
1.5.1 Free Electrons . . . . .	14
1.5.2 Field-Electron Interaction in a Coulomb Potential . . . . .	15
1.6 Measurement Techniques . . . . .	15
1.6.1 Cross-Section . . . . .	15
1.6.2 Streaking Camera . . . . .	16
<b>2 Laser-Dressed photoionization of Many-Electron Atoms</b>	<b>19</b>
2.1 Modeling the Ionization Process . . . . .	20
2.1.1 Neon . . . . .	23
2.2 Delay in Photoemission . . . . .	26
2.2.1 The Phase of Dipole Matrix Elements . . . . .	27
2.2.2 Attosecond Streaking on Neon . . . . .	28
2.3 Angular Streaking . . . . .	31
2.3.1 Analysis of Experimental Data . . . . .	33
<b>3 Overview of Field Interaction with Solids</b>	<b>37</b>
3.1 Electrons in a Periodic Potential . . . . .	38
3.2 Semiclassical Picture . . . . .	39
3.3 Interband Transitions . . . . .	41
3.4 Current and Polarization . . . . .	41

3.5	Classical Light-Matter Interaction . . . . .	43
3.5.1	Nonlinear, Noninstantaneous Response . . . . .	43
3.5.2	Reflection and Transmission . . . . .	45
<b>4</b>	<b>Interaction of a Dielectric with a Strong Field</b>	<b>47</b>
4.1	Numerical Solver of the TDSE . . . . .	48
4.2	Steering Current in a Dielectric . . . . .	54
4.2.1	Theoretical Analysis . . . . .	55
4.2.2	Comparison with the Experiment . . . . .	57
4.3	Highly Nonlinear Polarization Response . . . . .	58
4.3.1	Real Time Interband Excitation . . . . .	60
4.4	Transmitted and Reflected Field . . . . .	63
4.4.1	Approximate Solution of the Scalar Wave Equation . . . . .	63
4.4.2	Self Consistent Calculation . . . . .	66
4.5	Field Dressed States . . . . .	68
4.5.1	Kane and Houston Functions . . . . .	69
4.5.2	Accelerated Bloch States . . . . .	72
	<b>Conclusions</b>	<b>75</b>
	<b>Acknowledgement</b>	<b>85</b>

# List of Figures

1.1	Streaking ejected electrons . . . . .	17
2.1	Outline of the streaking process . . . . .	20
2.2	Cross Section and $\beta$ -parameter . . . . .	25
2.3	Group delay in neon . . . . .	29
2.4	Streaking spectrogram . . . . .	30
2.5	Delay measurement . . . . .	30
2.6	Comparison of helium spectra . . . . .	31
2.7	Different definitions of the asymmetry parameter . . . . .	33
2.8	Test of the Coulomb-Volkov approximation . . . . .	34
2.9	Schematic of the attosecond VMI . . . . .	34
2.10	Angular electron spectrum . . . . .	35
2.11	“Mask” to account for the non-uniformity of the detector . . . . .	36
3.1	Reflection and Transmission . . . . .	45
4.1	Band Structure . . . . .	50
4.2	Finite and bulk solid . . . . .	54
4.3	Low-pass Filter . . . . .	56
4.4	CEP dependence of the displaced charge . . . . .	57
4.5	Intensity dependence of the displaced charge. . . . .	57
4.6	Schematic of the metal-dielectric nanojunction . . . . .	58
4.7	Displaced charge comparison with experimental data . . . . .	59
4.8	Isolating polarization signal . . . . .	60
4.9	Time frequency analysis of the polarization . . . . .	62
4.10	Phase shifted electron response . . . . .	62
4.11	Outline of the dielectric . . . . .	64
4.12	Reflected field . . . . .	66
4.13	Plasma frequency . . . . .	67
4.14	Reflectivity . . . . .	68
4.15	Assessment of accelerated Bloch states . . . . .	72
4.16	Comparison of Probabilities . . . . .	74





# Abstract

Recent advancements in laser technology are quickly moving the frontiers of research: quantum dynamics can now be investigated in more detail, on new timescales, with an unprecedented level of control. These new possibilities offer a new ground for the theoretical study of fundamental processes; at the same time, a proper understanding of phenomena involved is necessary to explain measurements, and to indicate directions for further experiments. This Thesis deals with the theoretical investigation of particular cases of light-matter interaction, in atoms and in dielectrics. Regimes considered here have just become a subject of intensive investigation: they are acquiring more and more relevance as technological advancements make them experimentally accessible.

In the first part of the Thesis I consider a process as fundamental as the single-photon ionization of atoms: my modeling will include an ultrashort pulse (full width half maximum  $\sim 100$  as =  $10^{-16}$  s) exciting an electron to the continuum, and a strong few-cycle near-infrared laser field. This configuration is suitable to reproduce recent streaking experiments on atoms. I developed a numerical tool to simulate these dynamics in three dimensions: the process is quite elaborate and requires an adequate description of multi-electron atoms. With proper approximations I was able to calculate photoelectron spectra using just a few dipole matrix elements, which were obtained with the aid of our external collaborators, from refined atomic structure calculations. The results of our relatively simple tool are in very good agreement with more sophisticated numerical calculations. In addition to that, I discuss my contribution to the theoretical support of a fundamental experiment [I]: both simulations and measurements indicate a delay between two different channel of photoemission in neon. A careful investigation of the limit of validity of approximations employed reveals that the Coulomb-Volkov approximation is not suitable to describe fine details of the interaction with the laser pulse. I also report on our analysis of experimental data from angle-resolved attosecond streaking [II].

The second part of the Thesis is devoted to the investigation of inter-band excitations in dielectrics; driving this process with a high degree of control is on the edge of current technology. The ultrafast creation of charge carriers in an insulator is intriguing: dielectric properties of the medium change drastically, revealing features of the peculiar electron dynamics in such a situation. I have simulated this process solving the time dependent Schrödinger equation for a single electron in a one-dimensional lattice and analyzed how the charge  $Q$  displaced during the interaction with the pulse depends on laser parameters. These calculations reproduce to a good extent the behavior observed in the experiment [III]. Both the theory and the experiment point out a strong dependence of  $Q$  on laser parameters: this promises a high degree of control, and at the same time suggests the possibility of a solid-state device to characterize an optical pulse. I also study in detail the modification occurring in the electric response of the sample to the electric field. The purpose of this analysis is to identify some features directly related to dynamics of newly created charge carriers.

During my investigation of electron dynamics during an excitation process, I have often faced the difficulty to identify quantities which might resemble eigenstates of the time-dependent Hamiltonian. Similar field-dressed states would describe the distortion due to the field, of eigenstates of the field-free Hamiltonian [IV]. A proper definition of field-dressed states would allow a correct interpretation of the wavefunction in terms of instantaneous excited population, which is otherwise impossible to define.



# Zusammenfassung

Neueste Fortschritte im Bereich der Lasertechnologie erweitern schnell die Grenzen der Forschung. Quantendynamiken können genauer den je untersucht werden, aus kürzeren Zeitskalen und mit einer höheren Kontrollebene. Diese Entwicklung bietet neue Möglichkeiten, fundamentale Prozesse theoretisch zu untersuchen; darüber hinaus ist ein Verständnis der zu Grunde liegenden physikalischen Vorgänge erforderlich, um Messresultate zu erklären und mögliche Richtungen für künftige Experimente aufzuzeigen. Diese Doktorarbeit befasst sich mit der theoretischen Analyse bestimmter Licht-Materie-Wechselwirkungen in Atomen und Dielektrika. Die im Rahmen dieser Thesis untersuchten Bereiche sind aktuell Thema intensiver Forschung. Dank weiterer technologischer Entwicklungen, die Experimente in diesen Bereichen ausführbar machen, gewinnen sie immer weiter an Relevanz.

Im ersten Teil der Arbeit beschreibe ich den fundamentalen Prozess der atomaren Ionisation durch ein einzelnes Photon. Mein Model enthält einen ultrakurzen Lichtpuls mit einer Halbwertsbreite von  $\sim 100 \text{ as} = 10^{-16} \text{ s}$ , der ein Elektron in das Kontinuum anregt, sowie ein starkes Laserfeld im nahen infraroten Spektralbereich mit wenigen Zyklen. Diese Konfiguration erlaubt die Nachbildung von neuesten Streaking Experimenten an Atomen. Ich habe ein numerisches Werkzeug entwickelt, um diese Dynamiken in drei Dimensionen zu simulieren. Der Prozess ist sehr komplex und bedarf einer hinreichenden Beschreibung von Atomen mit mehreren Elektronen. Unter Berücksichtigung geeigneter Näherungen war es mir möglich, Photoelektronenspektren mit Hilfe nur weniger Dipolmatrixelemente zu berechnen, welche in Zusammenarbeit mit unseren externen Kollaborationspartnern durch verfeinerte Atomstruktur-Berechnungen bestimmt wurden. Die Ergebnisse unseres verhältnismäßig einfachen Vorgehens stimmen in einem hohen Grad mit fortgeschritteneren numerischen Methoden überein. Darüber hinaus diskutiere ich meinen Beitrag zur theoretischen Unterstützung eines grundlegenden Experiments [I]. Sowohl Simulationen als auch Messungen weisen auf eine Verzögerung zwischen zwei Photoemissionsskanälen in Neon hin. Eine sorgfältige Prüfung der Gültigkeit der verwendeten Näherungen verrät, dass die Coulomb-Volkov Näherung nicht geeignet ist, um feine Einzelheiten in der Wechselwirkung mit dem Laserpuls zu beschreiben. Außerdem berichte ich über unsere Analyse der Messdaten der winkelaufgelösten Attosekunden Streaking Experimente [II].

Der zweite Teil der Thesis widmet sich der Untersuchung von Interband-Anregungen in Dielektrika. Die kontrollierte Lenkung dieser Übergänge wurde erst mit aktuellster Technologie ermöglicht. Die ultraschnelle Erzeugung von Ladungsträgern in einem Isolator ist bemerkenswert. Die dielektrischen Eigenschaften ändern sich dramatisch, was Rückschlüsse auf die Elektronendynamik während dieser Anregung zulässt. Ich habe diesen Prozess durch Lösung der zeitabhängigen Schrödingergleichung für ein einzelnes Elektron in einem eindimensionalen Gitter simuliert und untersucht, wie sich die während des Lichtpulses verlagerte Ladung mit den Laserparametern ändert. Diese Berechnungen reproduzieren in hohem Maße das im Experiment beobachtete Verhalten [III]. Sowohl Theorie als auch Experiment weisen auf eine starke Abhängigkeit der Ladung von den Laserparametern hin. Dies verspricht ein hohes Maß an Kontrolle und deutet auf eine mögliche Anwendung eines Festkörperbauelements für die Charakterisierung eines optischen Pulses hin. Außerdem untersuche ich detailliert die Modifikationen der elektrischen Antwort des Samples auf ein externes elektrisches Feld. Das Ziel dieser Analyse ist die Identifikation einiger Eigenschaften die direkt mit der Dynamik der erzeugten Ladungsträger zusammenhängen.

Während der Untersuchung der Elektronendynamiken in einem Anregungsprozeß, stieß ich

oft auf die Problematik, Größen zu ermitteln, die Eigenzuständen des zeitabhängigen Hamilton-Operators ähneln könnten. Ähnliche “Field-dressed States” würden die Verzerrung der Eigenzustände des feldfreien Hamiltonoperators aufgrund des Felds beschreiben [IV]. Eine geeignete Definition der Field-dressed States würde eine korrekte Interpretation der Wellenfunktion in Abhängigkeit der instantanen angeregten Besetzung ermöglichen, welche sich auf anderem Wege nicht bestimmen lässt.

# List of Contributions by the Author

- [I] M. Schultze, M. Fiess, N. Karpowicz, J. Gagnon, M. Korbman, M. Hofstetter, S. Neppl, A. L. Cavalieri, Y. Komninos, Th. Mercouris, C. A. Nicolaides, R. Pazourek, S. Nagele, J. Feist, J. Burgdoerfer, A. M. Azzeer, R. Ernstorfer, R. Kienberger, U. Kleineberg, E. Goulielmakis, F. Krausz, and V. S. Yakovlev. Delay in photoemission. *Science*, **328**(5986):1658–1662, JUN 25 2010.

★ For this paper I have developed a numerical tool to simulate streaking in three dimension, providing the experiment with a theoretical comparison. Results of the calculations have also been employed to investigate the effect of the electron lens on electron spectra.

- [II] S. Zherebtsov, A. Wirth, T. Uphues, I. Znakovskaya, O. Herrwerth, J. Gagnon, M. Korbman, V. S. Yakovlev, M. J. J. Vrakking, M. Drescher, and M. F. Kling. Attosecond imaging of xuv-induced atomic photoemission and auger decay in strong laser fields. *Journal of Physics B: Atomic, Molecular and Optical Physics*, **44**(10):105601, 2011.

★ I have taken part in the discussions concerning the data analysis, and performed part of it.

- [III] A. Schiffrin, T. Paasch-Colberg, N. Karpowicz, V. Apalkov, D. Gerster, S. Mühlbrandt, M. Korbman, J. Reichert, M. Schultze, S. Holzner, J. Barth, R. Kienberger, R. Ernstorfer, V. S. Yakovlev, M. I. Stockman, and F. Krausz. Optical field-induced current in dielectrics. Submitted to Nature

★ I was involved in the study concerning the modeling of the system. I have developed a code for numerical simulations of relevant dynamics, which has helped the interpretation of the measurements.

- [IV] V.S. Yakovlev, M. Korbman, and A. Scrinzi. Dressed bound states for attosecond dynamics in strong laser fields. *Chemical Physics*, 2012.

In press.

★ I have worked on the same concept treated in the paper, for the case of a lattice potential. I have taken part in the investigation and in the attempts aimed at finding a proper definition of field-dressed states.



# Introduction

When the first evidence of laser radiation was reported, it was called “a solution looking for a problem”. However, it did not take long for the laser to find application in almost every branch of research. In fact, the technological development of coherent sources has been constantly joined by an advance of our knowledge of nature. Investigation tools offered by laser technology are unique, and often represent the current frontier of our ability in controlling natural phenomena: the largest intensity achieved, the narrowest frequency range, the shortest event created.

In the research group of Prof. Dr. Krausz these possibilities are on the edge of current technology: the “toolbox” available for the experimental investigation is surprising. Isolated bursts of light as short as a few tens of attoseconds [1] probe quantum phenomena, on a time scale which was technically out of reach when quantum mechanics was formulated. An extreme degree of control on the motion of quantum particles is offered by few-cycles intense pulses with a stabilized carrier envelope phase [2]; even the waveform of the pulse can now be controlled [3]. Working here as a theorist is a big opportunity and a challenge. A similar chance to penetrate the core of many well-known quantum phenomena is invaluable; it comes together with the exciting demand of reconsidering established descriptions of reality, and to formulate brand new ones. Time-honored models are continuously put in doubt in these new regimes: often they need to be adjusted, often they just become inappropriate and a new physical picture is requested. Finely tuned quantum dynamics on attosecond time-scale reveal the complicated interplay of many particles, and approximations commonly used may become inadequate. Finding the proper balance between the simplicity of the physical picture and the completeness of the underlying mathematical formulation is a non-trivial task. A few times we had to abandon an investigation path, with the bitter outcome that the approximations used were inappropriate. However our perseverance has yielded results, and we have reached some meaningful goals.

A big advantage offered by this field of research is that theory and experiment proceed often at the same pace. Theoretical hypothesis can be (relatively) quickly verified and implemented in the laboratory, and experimental results often stimulate theoretical advancements. Since we had the opportunity to work in close contact with groundbreaking measurements, our work has been triggered mainly by the necessity to model an experiment, analyze the data, explain the result. However, this has been the starting point, and sometimes the motivation, for an independent theoretical investigation, addressing fundamental questions.

## Investigation Topics and Motivation

Generally speaking, the research done during the PhD was devoted to the study of the interaction between electrons and a strong field. The Thesis treats two separate projects: the study of electron ionization in atoms with attosecond resolution (Ch. 1 and 2) and the investigation of inter-band transitions in a dielectric (Ch. 3 and 4). Both these topics deal with unexplored regimes. Theoretical support is required to supply a proper modeling of the systems, and to determine which effects are responsible for the observed behavior; at the same time, this basic comprehension of the system can suggest promising directions for subsequent measurements. The ability to predict the response of the system may increase our degree of control over the electron motion: the possibilities with the tools mentioned are extraordinary.

In both projects, a code was developed to simulate relevant dynamics. Results of the simulations were then used as a basis for the subsequent physical analysis and for testing analytical models. The numerical approach was similar in both cases. We have tried to avoid complex algorithms, favoring instead approximations in the modeling of dynamics: in this way we have saved coding and computational time, obtaining agile numerical tools whose results were more immediate to interpret. On the other hand, sometimes approximations turned out to be more severe than expected, and we had to find a way to adjust them.

**Attosecond ionization** For the ionization process, we have considered a scenario which is common in many recent experiments in attosecond science. A high-frequency pulse, as short as few tens of attoseconds, ionizes the atom in a single-photon transition; this happens in the presence of a strong, few-cycle near-infrared (NIR) field. After the ionization, the electron emitted is accelerated by the NIR field. This is the typical scheme of a pump-probe measurement: the ionization process (pump) is investigated by means of the subsequent acceleration (probe). Varying the delay between the pump and the probe enables a time resolution of the measurement. The possibility to explore an ionization experiment in real time is indeed intriguing: ionization is one of the most fundamental, and yet not completely understood, mechanisms in atoms. It has already revealed a lot about the structure of elements and molecules, and unraveling its temporal evolution can provide even more. It is well known that the ionization involves many-electron dynamics, which we expect to directly affect the motion of the ejected electron. The temporal information will be encoded in different scans – corresponding to different delays – of the electrons momentum distribution: in order to collect as much information as possible, our calculations will provide three-dimensional resolution, giving access to details hidden in the angular distribution. Our numerical simulation of these elaborate dynamics was based on the combination of refined many-electrons atomic structure calculations (provided by external collaborators), and a numerical solution of the time dependent Schrödinger equation for the ejected electron. These results were used in the first place to offer support to the fundamental experiment which has revealed for the first time a delay between two different photoionization channels. We have wondered, up to which level of detail our model worked. Among the approximations involved, the most critical is the one describing the acceleration of the ejected electron by the strong field: while the overall momentum shift is described correctly, modifications in the spectra due to the combined interaction with the field and with the parent ion may be not exactly reproduced. We looked for



---

traces of this non-trivial interaction and compared our tool with that of different calculations, some using a more refined approach. Analyzing the signal is not trivial, as a major effect is played by rather uninteresting, classical effects. We managed to point out a small modulation occurring in electron distributions due to the laser field: it represents the limit of our model, as it is not able to correctly reproduce the dependence of the modulation on the field.

**Inter-band excitation** The excitation between the valence and conduction bands of a dielectric – the other process which we have dealt with – is not less fascinating. Again, the feasibility of the measurement depends on very recent improvements in laser technology i.e. the capability to produce ultrashort, very strong laser pulses: a longer pulse, with an intensity large enough to excite a significant fraction of electrons, would destroy the sample. Modifications occurring in the sample after a similar excitation are radical, and involve all the optical and electrical properties of the medium. For a very short period of time, the dielectric acquires the capability to conduct electric current: being able to steer electrons in a medium on a femtosecond time scale would open new perspectives for signal processing. However, electrical conductivity is just one of the consequences. Electrons in the conduction band offer a different response to the electric field, changing drastically the dielectric properties of the sample; in addition to that, the wavepacket happens to be in a superposition of conduction and valence band states, resulting in quantum beating. All these effects deserve a proper theoretical analysis. Apart from the necessity to establish a firm control on the induced current, some fundamental questions raise in this extreme regime. The tunneling of an electron between bands has already been approached theoretically, but it is the first time that it is possible to have an experimental counterpart, performing a systematical investigation. It would be meaningful to reveal which details of the inter-band excitation can be found in the radiation emitted: this may suggest new experimental perspectives, and help the interpretation of the numerical calculations. In order to face this questions we have numerically solved the time dependent Schrödinger equation for a single electron in a lattice, and obtained response functions (current, polarization) from it. Our simple model did not reproduce all the features of the measurement; however, the comparison of the induced current is a first validation of our results. We have employed our numerical tool for the calculation of the dielectric response during inter-band excitation, pointing out several features which carry a trace of the nonlinear process; we have also studied how these features would appear in the reflected pulse.

A problem that we have often faced during the research, was to separate an electron wavefunction into its conduction- and valence-band components in the presence of an external electric field. This problem is equivalent to finding a proper approximate definition of eigenstates when the Hamiltonian depends explicitly on time. In the Thesis we present a short overview of similar definitions and implement one of them, showing how it performs.

The development of the numerical tool went hand in hand with the modeling and interpretation of the experiment; a controversy, which is still ongoing, has raised with another theoretical group, about the correct physical picture suitable to interpret the outcome of the experiment. In the Thesis we do not discuss in detail the matters under dispute, but we adopt our own perspective in discussing physical phenomena.



# Chapter 1

## Overview of Atomic Ionization

In this chapter we introduce well-known notions of the field-electron interaction in atoms. These fundamental concepts are here formulated to serve as a basis for the subsequent research (Ch. 2): for this goal we highlight some aspects usually regarded as less relevant, elaborating on them, while more general topics will be summarized or skipped. A more detailed coverage can be found in [4] and [5], which were also used for reference during the writing.

In Sec. 1.2 and Sec. 1.3 we describe different forms of the time dependent Schrödinger equation for different gauge choices. In Sec. 1.4 we obtain the continuum eigenstates for the field-free Hamiltonian in the Coulomb potential, and discuss aspects relevant for the ionization; the interaction with the field is introduced in Sec. 1.5. Finally in Sec. 1.6 we will briefly present techniques used in photoionization measurements. Atomic units are used throughout the Thesis, except where stated otherwise.

### 1.1 The Time Dependent Schrödinger Equation

Let us consider a quantum system which at time  $t_0$  is in a state  $|\psi(t_0)\rangle$ . This state represents the whole knowledge that we can have of the system and also the limit to it: once the quantum state of the system is determined we have in our hands all the possible information about its physical properties, and any finer-grained investigation is impossible according to laws of quantum mechanics. The spatial distribution of the system is provided by the decomposition in coordinate space

$$\langle \mathbf{r} | \psi(t_0) \rangle = \psi(\mathbf{r}, t_0), \quad (1.1)$$

while the momentum distribution comes from the decomposition on eigenstates of the momentum operator

$$\langle \mathbf{p} | \psi(t_0) \rangle = \psi(\mathbf{p}, t_0). \quad (1.2)$$

The two representations are connected by

$$\langle \mathbf{r} | \psi(t_0) \rangle = \int d^3\mathbf{p} \langle \mathbf{r} | \mathbf{p} \rangle \langle \mathbf{p} | \psi(t_0) \rangle = \frac{1}{\sqrt{(2\pi)^3}} \int d^3\mathbf{p} e^{i\mathbf{p}\cdot\mathbf{r}} \langle \mathbf{p} | \psi(t_0) \rangle. \quad (1.3)$$

The time-evolution of the quantum state is formally determined by the Hamiltonian  $\hat{H}$  according to the Time Dependent Schrödinger Equation (TDSE)

$$i \frac{d}{dt} |\psi(t)\rangle = \hat{H} |\psi(t)\rangle . \quad (1.4)$$

The analytical solution of this equation is possible just in few textbook examples. Solving it exactly with a numerical approach is feasible in very simple cases as well. In general, all the cases where the Hamiltonian depends explicitly on time and the system includes more than two particles can be solved numerically after an approximate modeling. All the physical questions that we will address in this Thesis will require the solution of the TDSE for many-particle systems interacting with an electric field: the Hamiltonian will depend on time through the interaction with the field. Our approach will be to identify the core of the problem, and to model it in the simplest possible way trying to include all relevant physical details. Particles will be modeled as quantum objects, but the field will not be quantized. Eq. (1.4) will be then numerically propagated within the model developed. The software is developed in C++ taking advantage of some algorithms from GSL and LAPACK libraries.

## 1.2 S-matrix Approach

Sometimes it is more convenient to rewrite the TDSE in different forms, highlighting some aspects of the evolution with respect to others. Following [6] the so-called ‘‘S-matrix’’ expression is derived, for the probability amplitude of the transition from the initial state  $|i\rangle$  to the final state  $|f\rangle$ , under the action of the time-dependent Hamiltonian  $\hat{H}(t)$ . Formally, this probability amplitude is  $a_{i,f} = \langle f | \hat{U}(t_f, t_i) | i \rangle$ , where  $t_i$  and  $t_f$  are usually chosen before the beginning and after the end of the time-dependent interaction. The S-matrix expression is obtained elaborating on the time evolution operator  $\hat{U}(t, t_i)$  associated with the Hamiltonian  $\hat{H}(t)$ . The TDSE can be equally written as

$$i \frac{d}{dt} \hat{U}(t, t_i) = \hat{H}(t) \hat{U}(t, t_i) . \quad (1.5)$$

The Hamiltonian is separated in two parts

$$\hat{H} = \hat{H}_0(t) + \hat{V}(t) , \quad (1.6)$$

assuming that the propagator  $\hat{U}_0$  relative to  $\hat{H}_0$  is known. Eq. (1.5) is exactly equivalent to the Schrödinger equation and we can rewrite it in an integral form without any approximation:

$$\hat{U}(t, t_i) = \hat{U}_0(t, t_i) - i \int_{t_i}^t dt' \hat{U}(t, t') \hat{V}(t') \hat{U}_0(t', t_i) . \quad (1.7)$$

The physical meaning of this equation will be discussed later, now we show that it is indeed equivalent to the TDSE, explicitly evaluating the derivative of  $\hat{U}$ :

$$i \frac{d}{dt} \hat{U}(t, t_i) = \hat{H}_0(t) \hat{U}_0(t, t_i) + \hat{V}(t) \hat{U}_0(t, t_i) - i \hat{H}(t) \int_{t_i}^t dt' \hat{U}(t, t') \hat{V}(t') \hat{U}_0(t', t_i) , \quad (1.8)$$

where we have used Eq.(1.5) to express the derivatives of  $\hat{U}$  and  $\hat{U}_0$ ; evaluating the derivative of the integral a term  $U(t, t) = 1$  appears. In the first two terms of the right hand side we recognize the full Hamiltonian, and the term in the integral is exactly what appears in Eq. (1.7). We can rewrite the above equation as

$$i \frac{d}{dt} \hat{U}(t, t_i) = \hat{H}(t) \left( \hat{U}_0(t, t_i) - i \int_{t_i}^t dt' \hat{U}(t, t') \hat{V}(t') \hat{U}_0(t', t_i) \right) = \hat{H}(t) \hat{U}(t, t_i), \quad (1.9)$$

proving that our claim (1.7) is correct. We can apply it to formally evaluate the probability amplitude,

$$a_{i,f} = \langle f | \hat{U}_0(t_f, t_i) | i \rangle - i \int_{t_i}^{t_f} dt' \langle f | \hat{U}(t, t') \hat{V}(t') \hat{U}_0(t', t_i) | i \rangle. \quad (1.10)$$

The integrand represents the evolution until  $t'$  with the Hamiltonian  $H_0$ , the interaction with  $V(t')$  at that particular moment, and then the full propagation: the probability amplitude is the sum over all possible paths i.e. moments at which the system interacts with  $\hat{V}$ . Eq. (1.10) is very useful as a starting point for simplifying the mathematical description of the evolution, for example if one wants to introduce approximations in the full propagator  $\hat{U}$ .

## 1.3 Length and Velocity Gauge

The Hamiltonian for the interaction of a charged particle with an electric field has different expressions, related by unitary transformations. Let us consider a field with scalar potential  $V$  and vector potential  $\mathbf{A}$ ; in classical mechanics, the Lagrangian and the Hamiltonian of interaction are

$$\mathcal{L} = \frac{\dot{\mathbf{x}}^2}{2} + q \dot{\mathbf{x}} \cdot \mathbf{A} - qV \quad \text{and} \quad \mathcal{H} = \frac{1}{2}(\mathbf{p} - q\mathbf{A})^2 + qV, \quad (1.11)$$

where  $q$  is the charge of the particle. We will be dealing mainly with electrons: therefore in the following we will always take  $q = -1$  (in atomic units). The classical equation can be translated in the quantum picture, taking into account that operators do not commute; the Hamiltonian is

$$\hat{H} = \frac{1}{2} \left( \hat{p}^2 + \mathbf{A} \cdot \hat{\mathbf{p}} + \hat{\mathbf{p}} \cdot \mathbf{A} + A^2 \right) + V(\hat{\mathbf{x}}). \quad (1.12)$$

Maxwell equations leave some freedom in adjusting the potentials. Imposing  $\nabla \cdot \mathbf{A} = 0$  (Coulomb gauge),  $\hat{\mathbf{p}}$  and  $\mathbf{A}$  commute,

$$[\hat{\mathbf{p}}, \mathbf{A}] = -i \nabla \cdot \mathbf{A} = 0. \quad (1.13)$$

In the coordinate representation, the TDSE assumes the form

$$i \frac{d}{dt} \Psi(\mathbf{r}, t) = \left[ -\frac{\nabla^2}{2} - i\mathbf{A} \cdot \nabla + \frac{A^2}{2} + V(\mathbf{x}) \right] \Psi(\mathbf{r}, t). \quad (1.14)$$

The derivation until now is quite general, as it depends just on a gauge choice. A further simplification arises if we are allowed to assume that the field is uniform. In the cases under

examination in this thesis we will consider fields with wavelengths from 10 nm (far ultraviolet) to 700 nm (near infrared): these wavelengths are large compared with the Bohr radius 0.053 nm or with the size of a unit cell in solids  $\sim 1$  nm. We will continue the derivation, and subsequent calculations, in the dipole approximation, assuming that the external field is uniform. The reason why we need this additional condition is that

$$\nabla^2 \mathbf{A} = \nabla(\nabla \cdot \mathbf{A}) - \nabla \times (\nabla \times \mathbf{A}) ,$$

therefore  $\nabla \cdot \mathbf{A} = 0$  is not sufficient to infer that  $\nabla^2 \mathbf{A} = 0$ . Two gauge transformations are presented: the first one is a simplification of Eq. 1.14, the second one is more properly a change of frame of reference.

- **Canceling  $A^2$ :**

Unitary transformation  $\Psi(\mathbf{r}, t) = \psi(\mathbf{r}, t) e^{(-\frac{i}{2} \int_{-\infty}^t A^2(t') dt')}$ . Substituting it in the TDSE all the spatial derivatives are zero, and the time derivative provides a term which exactly cancels  $A^2/2$ . The evolution of the wavefunction  $\psi$  is governed by

$$i \frac{d}{dt} \psi(\mathbf{r}, t) = \left[ -\frac{\nabla^2}{2} - i \mathbf{A} \cdot \nabla + V(\mathbf{x}) \right] \psi(\mathbf{r}, t) . \quad (1.15)$$

We will refer to it as the *velocity gauge* Hamiltonian.

- **Length Gauge:**

Unitary transformation  $\Phi(\mathbf{r}, t) = \Psi(\mathbf{r}, t) e^{i \mathbf{A}(t) \cdot \mathbf{r}}$ . The time derivative and the Laplacian of the transformed wavefunction are

$$\begin{aligned} i \frac{d}{dt} \Phi(\mathbf{r}, t) &= e^{i \mathbf{A}(t) \cdot \mathbf{r}} \left[ \frac{d}{dt} + \mathbf{E}(t) \right] \Psi(\mathbf{r}, t) \\ \frac{\nabla^2}{2} \Phi(\mathbf{r}, t) &= e^{i \mathbf{A}(t) \cdot \mathbf{r}} \left[ \frac{\nabla^2}{2} + i \mathbf{A}(t) \cdot \nabla - \frac{A^2(t)}{2} \right] \Psi(\mathbf{r}, t) , \end{aligned}$$

where the electric field  $\mathbf{E}(t) = -\frac{d}{dt} \mathbf{A}(t)$ . The TDSE in this gauge is

$$i \frac{d}{dt} \Phi(\mathbf{r}, t) = \left[ -\frac{\nabla^2}{2} + \mathbf{E} \cdot \mathbf{r} + V(\mathbf{x}) \right] \Phi(\mathbf{r}, t) . \quad (1.16)$$

We will refer to it as the *length gauge* Hamiltonian.

The Hamiltonians obtained in the two gauges are quite symmetric: in the first one we recognize the momentum operator  $\hat{\mathbf{p}} = -i \nabla$  coupling the interaction with the vector potential, while in the second one the coordinate operator  $\hat{\mathbf{r}}$  couples the interaction with the electric field. Let us consider the physical meaning of the unitary transformation  $e^{-i \mathbf{A}(t) \cdot \mathbf{r}}$ . Its action on a plane wave is to shift the momentum

$$\langle \mathbf{r} | \mathbf{p} \rangle e^{-i \mathbf{A}(t) \cdot \mathbf{r}} = \frac{1}{\sqrt{(2\pi)^3}} e^{i(\mathbf{p} - \mathbf{A}(t)) \cdot \mathbf{r}} = \langle \mathbf{r} | \mathbf{p} - \mathbf{A}(t) \rangle ,$$

and indeed the operator  $\hat{T}(\alpha) = e^{i \alpha \mathbf{r}}$  is the translation operator in the momentum representation. The momentum of a classical electron in an electric field is  $\mathbf{p}(t) = \mathbf{p}(-\infty) + \mathbf{A}(t)$ : going from the

length to the velocity gauge we are canceling the acceleration that the electron experiences from the field. In other words the unitary transformation considered can be interpreted as switching between a static frame of reference (length gauge) to a frame of reference which moves according to the expected motion of a free electron (velocity gauge).

The transformations considered are unitary: they will not change the scalar product

$$\langle \psi_2 | \hat{U}^\dagger \hat{U} | \psi_1 \rangle = \langle \psi_2 | \psi_1 \rangle , \quad (1.17)$$

but it is necessary to pay attention to how we manage the observables. The recipe is straightforward for time-independent operators  $\hat{O}$ . If we apply the unitary transformation  $\hat{U}$  to the Hilbert space, we have to transform operators accordingly,  $\hat{O}' = \hat{U} \hat{O} \hat{U}^\dagger$ : in this way the matrix elements of the operator are conserved in the transformation,

$$\langle \psi_2 | \hat{U}^\dagger \hat{O}' \hat{U} | \psi_1 \rangle = \langle \psi_2 | \hat{O} | \psi_1 \rangle . \quad (1.18)$$

For the particular case considered here, we can take advantage of the classical analogy to better understand which observables to use in different gauges. In Hamiltonian mechanics the canonical momentum defined from Eq. (1.11) is

$$\mathbf{p}_c = \frac{\partial}{\partial \dot{\mathbf{x}}} \mathcal{L} = \dot{\mathbf{x}} - \mathbf{A} , \quad (1.19)$$

and therefore the velocity is  $\dot{\mathbf{x}} = \mathbf{p}_c + \mathbf{A}$ . In the quantum case the momentum operator corresponds to the canonical momentum. Its value in the velocity gauge is  $\langle \psi | -i \nabla | \psi \rangle = \langle \hat{\mathbf{p}}_c \rangle$  and in the length gauge  $\langle \Phi | -i \nabla | \Phi \rangle = \langle \hat{\mathbf{p}}_c \rangle + \mathbf{A}$ : the canonical momentum corresponds to the velocity of the electron in the lab frame (length gauge), but not in the velocity gauge.

We have to be particularly careful with quantities which do not correspond to Hermitian operators. The electric current in the length gauge is defined as

$$\mathbf{J}(\mathbf{r}) = \frac{i}{2} [\Phi^*(\mathbf{r}) \nabla \Phi(\mathbf{r}) - \Phi(\mathbf{r}) \nabla \Phi^*(\mathbf{r})] = -\text{Im} [\Phi^*(\mathbf{r}) \nabla \Phi(\mathbf{r})] , \quad (1.20)$$

i.e. the opposite of the probability current because the charge of the electron is  $-1$ . This expression is not invariant under gauge transformations; let us consider the generic change of basis

$$\psi_\beta(\mathbf{r}) = e^{-i(1-\beta)\mathbf{A}\cdot\mathbf{r}} \Phi(\mathbf{r}) , \quad (1.21)$$

which reduces to the velocity gauge if  $\beta = 0$ . The electric current in terms of the transformed wavefunction is

$$\mathbf{J}_\beta(\mathbf{r}) = -\text{Im} [\psi^*(\mathbf{r}) \nabla \psi(\mathbf{r})] - (1 - \beta) \mathbf{A}(t) |\psi(\mathbf{r})|^2 : \quad (1.22)$$

calculating the current in the velocity gauge, one has to pay attention and include the last factor, which accounts for the unphysical contribution due to the frame of reference which moves with the electron. For example, in the fictitious case of a constant vector potential, if we used Eq. (1.20) we would observe a non-zero current in the velocity gauge, even though the electric field  $E = -\frac{dA}{dt}$  is zero. We define the current in the velocity gauge as

$$\mathbf{J}_V(\mathbf{r}) = -\text{Im} [\psi^*(\mathbf{r}) \nabla \psi(\mathbf{r})] - \mathbf{A}(t) |\psi(\mathbf{r})|^2 . \quad (1.23)$$

## 1.4 Electrons in a Coulomb Potential

The case of a single electron in a Coulomb potential is of great importance, as it can be solved analytically. Concepts commonly used to describe many-electron atoms have their foundation and exact mathematical expression here. Even further, many-electron atoms are often described in terms of one electron feeling the Coulomb potential of a “total charge”, which contains the nucleus and the other electrons: this approximation becomes exact if the electron is far enough from the nucleus, for example after ionization. In our investigation of the ionization process we will use many of the notions introduced here. The Hamiltonian is

$$\hat{H} = \frac{\hat{\mathbf{p}}^2}{2} - \frac{Z}{r}, \quad (1.24)$$

where  $Z$  is the charge generating the Coulomb potential; this equation describes the hydrogen atom if we neglect the mass of the electron ( $= 1$ ) with respect to the mass of the proton ( $\sim 1800$ ), and in general any single-electron motion in an atomic potential (hydrogenic atoms).

### 1.4.1 Hydrogenic Wavefunctions

The eigenvalue equation for the Hamiltonian Eq. (1.24), assuming  $Z = 1$  is

$$\left[ -\frac{\nabla^2}{2} - \frac{1}{r} \right] \psi(\mathbf{r}) = \mathcal{E} \psi(\mathbf{r}). \quad (1.25)$$

Since the Coulomb potential is central, it is convenient to express the Laplacian in polar coordinates

$$\left[ -\frac{1}{2r} \left( \frac{\partial^2}{\partial r^2} r \right) + \frac{\hat{L}^2}{2r^2} - \frac{1}{r} \right] \psi(\mathbf{r}) = \mathcal{E} \psi(\mathbf{r}), \quad (1.26)$$

where  $\hat{L}^2$  is the angular part of the Laplacian

$$\hat{L}^2 = -\frac{1}{\sin(\theta)} \frac{\partial}{\partial \theta} \left( \sin(\theta) \frac{\partial}{\partial \theta} \right) - \frac{1}{\sin^2(\theta)} \frac{\partial^2}{\partial \varphi^2}. \quad (1.27)$$

The solutions of Eq. (1.26) have the separable form

$$\psi_{\mathcal{E}lm}(\mathbf{r}) = R_{\mathcal{E}l}(r) Y_{lm}(\theta, \varphi); \quad (1.28)$$

$l$ ,  $m$  are respectively the azimuthal and the magnetic quantum number, and  $Y_{lm}(\theta, \varphi)$  are the spherical harmonics, eigenfunctions of  $\hat{L}^2$  with eigenvalue  $l(l+1)$ . Inserting the ansatz above in Eq. (1.26) we obtain the Schrödinger equation for the radial wavefunctions

$$\left[ -\frac{1}{2r} \left( \frac{\partial^2}{\partial r^2} r \right) + \frac{l(l+1)}{2r^2} - \frac{1}{r} \right] R_{\mathcal{E}l}(r) = \mathcal{E} R_{\mathcal{E}l}(r). \quad (1.29)$$

Eigenfunctions corresponding to negative eigenvalues (discrete spectrum) can be expressed in terms of Laguerre polynomials: they are of limited interest in our case and we will not discuss



them. Let us focus on the continuous spectrum, corresponding to positive values of the energy  $\mathcal{E} = \frac{p^2}{2}$ . It is convenient to rewrite Eq. (1.29) in terms of the function  $\rho(r) = rR_{pl}(r)$ :

$$-\frac{1}{2} \left( \frac{\partial^2}{\partial r^2} \rho(r) \right) + \left[ \frac{l(l+1)}{2r^2} - \frac{1}{r} \right] \rho(r) = \mathcal{E} \rho(r). \quad (1.30)$$

Solutions of this equation have the form

$$R_{pl}(r) = \frac{C_{pl}}{(2l+1)!} (2pr)^l e^{-ipr} F \left( \frac{i}{p} + l + 1, 2l + 2, 2ipr \right), \quad (1.31)$$

where  $F$  is the confluent hypergeometric functions [4], and  $C_{pl}$  are normalization coefficients. There are two possible normalization choices for the radial part of continuum eigenfunctions:

$$\text{on the energy scale} \quad \int_0^{+\infty} dr r^2 R_{\mathcal{E}'l} R_{\mathcal{E}l} = \delta(\mathcal{E}' - \mathcal{E}) \quad (1.32)$$

$$\text{and on the momentum scale} \quad \int_0^{+\infty} dr r^2 R_{p'l} R_{pl} = 2\pi \delta(p' - p). \quad (1.33)$$

For general properties of the delta function, these wavefunctions are related by

$$R_{\mathcal{E}l} = \sqrt{\frac{1}{2\pi p}} R_{pl}. \quad (1.34)$$

We will always consider wavefunctions normalized on the momentum scale. The asymptotic behavior of Eq. (1.31) is needed for determining coefficients  $C_{pl}$ , but it is also intrinsically important for the study of the photoionization; for  $r \rightarrow \infty$

$$R_{pl} \approx \frac{2}{r} \sin \left( pr + \frac{1}{p} \ln(2pr) - \frac{\pi}{2} l + \sigma_l \right), \quad (1.35)$$

$$\sigma_l = \arg \left[ \Gamma \left( l + 1 - \frac{i}{p} \right) \right]$$

where  $\Gamma$  is the gamma function. If we had solved the same problem without the Coulomb potential, we would have obtained spherical Bessel functions as radial solutions [5]: their asymptotic behavior is very similar to Eq. (1.35), without the logarithmic term and the phase shift  $\sigma_l$ . These two terms are consequence of the long-range potential considered, which has a non-negligible contribution also at the infinity. As we will see in the following, the phase shift of the wavefunction plays a major role in determining electron dynamics and we will determine it as accurately as possible in the numerical calculations. The next section deals specifically with this topic.

## 1.4.2 Phases of Coulomb Wavefunctions

In Ch. 2 we will discuss the use of atomic structure calculations to determine eigenstates and dipole matrix elements in atoms. The phase shift of the continuum wavefunction is an important

outcome of these calculations: it will be obtained by joining the calculated wavefunction with the expected solution for the single electron. In this section we determine the phase shift for the single electron case: the derivation is based on [7] and [8], which are also part of the theoretical foundation of the atomic structure calculations.

Let us write Eq. (1.30) in terms of a total effective potential

$$\begin{aligned} \left[ \frac{\partial^2}{\partial r^2} + w(r) \right] \rho(r) &= 0 \\ w(r) &= p^2 - \frac{l(l+1)}{r^2} + \frac{2}{r} \quad . \end{aligned} \quad (1.36)$$

In the WKB approximation [9] we can write the the solution as

$$\rho(r) = \frac{C}{\sqrt[4]{w(r)}} e^{i\phi(r) - iEt} \quad , \quad (1.37)$$

where  $\phi(r) = \int_0^r \sqrt{w(r')} dr'$ . This expression can be integrated analytically, choosing the integration constant in such a way that at large distances  $\phi(r) \approx pr + \frac{1}{p} \ln(2pr) - \frac{\pi}{2}l + \sigma_l$  as expected from the asymptotic behavior of the exact solution Eq. (1.35). The result of the integration is

$$\phi(r) = \varsigma_l + \phi_0(r) \quad (1.38)$$

where

$$\begin{aligned} \varsigma_l &= \left( \sigma_l - \frac{\pi}{2}l - \frac{1}{p} - \frac{1}{p} \ln p \right) \\ \phi_0(r) &= \chi(r) + \frac{1}{p} \ln \left( 1 + p^2 r + p\chi(r) \right) + \sqrt{L} \arccos \left[ \frac{r - L + pL\chi(r)}{r(1 + p^2 L)} \right] \\ \chi(r) &= \sqrt{p^2 \rho^2 + 2\rho - L} \\ L &= l(l+1) \quad . \end{aligned} \quad (1.39)$$

The term relevant for us is  $\varsigma_l$ : it does not depend on  $r$  (and therefore it does not vanish at the infinity), and represents the phase shift of the wavefunction.

### 1.4.3 Scattering States

The motion of a free electron in the proximity of a Coulomb potential is an important part of photoionization dynamics. We consider here the scattering process of an electronic plane wave  $e^{i\mathbf{p}\cdot\mathbf{r}}$  on an atomic nucleus. Scattered waves  $\xi_{\mathbf{p}}(\mathbf{r})$  originating in such a process, asymptotically contain a plane wave propagating in direction  $\mathbf{p}$  and an outgoing spherical wave

$$\xi_{\mathbf{p}}(r) \approx e^{i\mathbf{p}\cdot\mathbf{r}} + \frac{1}{r} f \left( \frac{\mathbf{p} \cdot \mathbf{r}}{pr} \right) e^{ipr} \quad , \quad (1.40)$$

where  $\frac{\mathbf{p}\cdot\mathbf{r}}{pr}$  is the cosine of the propagation angle (independent on the choice of the axes). Since the potential is central, these states are axially symmetric with respect to the propagation direction.

They can be expressed in terms of functions Eq. (1.31), which form a complete basis if the azimuthal part of spherical harmonics (Legendre polynomial  $P_l$ ) is included:

$$\xi_{\mathbf{p}}(\mathbf{r}) = \sum_{l=0}^{\infty} A_l P_l \left( \frac{\mathbf{p} \cdot \mathbf{r}}{pr} \right) R_{pl}(r), \quad (1.41)$$

$A_l$  are coefficients which at large distances must give the expected form Eq. (1.40). It is possible to show that

$$A_l = \frac{1}{2p} (2l+1) i^l e^{i\delta_l} \quad (1.42)$$

fulfill this request. To verify it, let us write the asymptotic form of the Coulomb wavefunction Eq. (1.35) – neglecting the logarithmic term with respect to the linear one – as

$$R_{pl}(r) \approx \frac{1}{ir} \left[ (-i)^l e^{i(pr+\delta_l)} - i^l e^{-i(pr+\delta_l)} \right]. \quad (1.43)$$

Substituting this expression and the guess Eq. (1.42) into Eq. (1.41), we obtain the asymptotic expansion of the scattered wavefunction

$$\xi_{\mathbf{p}}(\mathbf{r}) \approx \frac{1}{2i pr} \sum_{l=0}^{\infty} (2l+1) P_l \left( \frac{\mathbf{p} \cdot \mathbf{r}}{pr} \right) \left[ (-1)^{l+1} e^{-ipr} + e^{2i\delta_l} e^{ipr} \right]. \quad (1.44)$$

For comparison, the decomposition of the plane wave in spherical waves is

$$e^{i\mathbf{p} \cdot \mathbf{r}} = \sum_{l=0}^{\infty} (2l+1) i^l P_l \left( \frac{\mathbf{p} \cdot \mathbf{r}}{pr} \right) j_l(pr), \quad (1.45)$$

where  $j_l$  are the spherical Bessel functions; its asymptotic form is

$$e^{i\mathbf{p} \cdot \mathbf{r}} \approx \frac{1}{2i pr} \sum_{l=0}^{\infty} (2l+1) P_l \left( \frac{\mathbf{p} \cdot \mathbf{r}}{pr} \right) \left[ (-1)^{l+1} e^{-ipr} + e^{ipr} \right]. \quad (1.46)$$

Considering the difference  $\xi_{\mathbf{p}}(r) - e^{ipr}$  we notice that indeed all the terms relative to incoming spherical waves disappear and the remaining expression has the form Eq. (1.40), validating the guess Eq. (1.42).

Using coefficients  $A_l$  we can introduce the set of outgoing scattering waves

$$\xi_{\mathbf{p}}^+(\mathbf{r}) = \frac{1}{2p} \sum_{l=0}^{\infty} i^l (2l+1) e^{i\delta_l} P_l \left( \frac{\mathbf{p} \cdot \mathbf{r}}{pr} \right) R_{pl}(r), \quad (1.47)$$

which are orthonormal on  $\mathbf{p}$ . The + sign represents our initial request, that at the infinity they propagate as an outgoing spherical wave. Beside these functions, we can introduce a set corresponding to states which asymptotically have a plane wave and an incoming spherical wave. They are defined as

$$\xi_{\mathbf{p}}^-(\mathbf{r}) = \left( \xi_{-\mathbf{p}}^+(\mathbf{r}) \right)^*, \quad (1.48)$$

because the complex conjugation transforms an outgoing wave into an ingoing one; to keep the definition of a plane wave  $e^{i\mathbf{p}\cdot\mathbf{r}}$  we have to change the sign of the vector  $\mathbf{p}$ . Using the property of Legendre polynomials  $P_l(-\cos\theta) = (-1)^l P_l(\cos\theta)$ , the explicit form of the incoming scattering waves is

$$\xi_{\mathbf{p}}^-(\mathbf{r}) = \frac{1}{2p} \sum_{l=0}^{\infty} i^l (2l+1) e^{-i\delta_l} P_l\left(\frac{\mathbf{p}\cdot\mathbf{r}}{pr}\right) R_{pl}(r). \quad (1.49)$$

## 1.5 Electrons in a Homogeneous Time-Dependent Electric Field

### 1.5.1 Free Electrons

Our main investigation probe for electron dynamics will be an electric field. It makes sense to analyze the behavior of a free electron interacting with an electric field: its analytical solution [10, 11] will be a frequent ingredient in representing dynamics, and we will often use it as test ground for models.

Since the only interaction is with the electric field, the most convenient system of reference is that of the electron and the velocity gauge Eq. (1.14) is used. Its expression in Fourier space is

$$i\frac{d}{dt}\tilde{\psi}(\mathbf{p}, t) = \frac{1}{2} [p^2 + 2\mathbf{A}(t)\cdot\mathbf{p} + A(t)^2] \tilde{\psi}(\mathbf{p}, t) \quad (1.50)$$

where  $\tilde{\psi}(\mathbf{p}, t)$  is the Fourier transform of the wavefunction,

$$\tilde{\psi}(\mathbf{p}, t) = \langle \mathbf{p} | \psi(t) \rangle = \int d^3\mathbf{r} \langle \mathbf{p} | \mathbf{r} \rangle \langle \mathbf{r} | \psi(t) \rangle = \frac{1}{\sqrt{(2\pi)^3}} \int d^3\mathbf{r} e^{-i\mathbf{p}\cdot\mathbf{r}} \psi(\mathbf{r}, t). \quad (1.51)$$

The differential equation is easily solved,

$$\tilde{\psi}(\mathbf{p}, t) = \tilde{\psi}(\mathbf{p}, t_0) e^{-\frac{i}{2} \int_{t_0}^t dt' [\mathbf{p} + \mathbf{A}(t')]^2}. \quad (1.52)$$

The solution in coordinate space is

$$\psi(\mathbf{r}, t) = \frac{1}{\sqrt{(2\pi)^3}} \int d^3\mathbf{p} e^{i\mathbf{p}\cdot\mathbf{r}} e^{i\phi_V(\mathbf{p}, t)} \tilde{\psi}(\mathbf{p}, t_0), \quad (1.53)$$

where we have isolated the phase factor

$$\phi_V(\mathbf{p}, t) = -\frac{1}{2} \int_{t_0}^t dt' [\mathbf{p} + \mathbf{A}(t')]^2. \quad (1.54)$$

Wavefunctions in Eq. (1.53) are known as ‘‘Volkov solutions’’, and the phase factor in Eq. (1.54) as ‘‘Volkov phase’’. The result obtained fits in the picture of a system of reference moving with the electron: the momentum is not modified by the field, but Volkov solutions acquire a time-dependent phase during the interaction.

### 1.5.2 Field-Electron Interaction in a Coulomb Potential

Exact eigenstates for a single electron in a Coulomb potential were presented, together with the solutions of the TDSE for a free electron accelerated by a field. In our investigation of the ionization we will be interested in the combination of the two processes: an electron interacting with a Coulomb potential in the presence of an electric field. Since an exact solution of the Schrödinger equation for this problem is unknown, many attempts have been made to find a proper ansatz approximating the wavefunction. At the very least, the guessed wavefunction should reduce to the Volkov solution if the Coulomb potential is zero, and to the Coulomb continuum state if the electric field is turned off. The Coulomb-Volkov functions [12, 13] are the simplest solution to the problem; as the name suggests they are a combination of Coulomb eigenstates and Volkov solutions. The ansatz is that the Coulomb wavefunction Eq. (1.31) acquire the Volkov phase Eq. (1.54):

$$\psi_{\mathbf{p}}^{\text{CV}}(r, t) = e^{i\phi_V(\mathbf{p}, t)} R_{pl}(r) . \quad (1.55)$$

If there is no electric field, the time evolution becomes the simple phase factor acquired by an eigenstate of the Hamiltonian; if the potential is zero, the wavefunction becomes a plane wave with the Volkov phase. Solutions (1.55) have found wide application [14, 15, 16]; at the same time many ways have been proposed to assess their accuracy and to improve them [17, 18, 19]. We will use them to describe the motion of the electron far from the ion, and it will be one of our major approximations.

## 1.6 Measurement Techniques

One of the main branch of our work was to study what kind of information is possible to obtain from ionization experiments once they are performed on an attosecond time-scale. Here we will briefly discuss relevant notions about ionization measurements, and the Attosecond Streak Camera, which is one of the most important tools for time-resolved attosecond measurements with attosecond isolated pulses.

### 1.6.1 Cross-Section

The most natural quantity to measure in an ionization experiment is the total yield of electrons  $N$ ; we define the total cross-section dividing it by the flux  $F$  of incident particles (intensity of the laser beam),  $\sigma_{\text{tot}} = N/F$ . Dividing the ejected electrons according to the channel, the kinetic energy, and the angle of emission will provide a better insight into the atomic structure. In the dipole approximation, the cross-section for the ionization process between an initial state  $|i\rangle$  and a final state  $|f\rangle$  is

$$\sigma_{\text{if}} = \frac{4\pi^2 \alpha a_0^2}{3} h\nu |D_{\text{if}}|^2 , \quad (1.56)$$

where  $\alpha$  is the fine structure constant,  $a_0$  the Bohr radius and  $h\nu$  the photon energy.  $D_{\text{if}}$  is the dipole matrix element for the considered transition  $D_{\text{if}} = \langle f | \mathbf{r} | i \rangle$ . The distinction between ionization channels usually occurs through the energy resolution of emitted electrons: the kinetic

energy of the electron is equal to the photon energy minus the binding energy. This kind of partial cross-sections reflect not only the orbital structure of a particular shell, but also interactions triggered by the ionization, as shake-up and Auger decay. However, components corresponding to different azimuthal numbers  $l$  are not separated in energy: since they correspond to different symmetry of the outgoing electron wave, angle-resolved measurements are a way to resolve these finer details. If an atom is initially spherical symmetric, the distribution of the electron yield will be symmetric around the angle  $\varphi$  spanning the plane perpendicular to the polarization direction  $z$  (see Fig. 2.1). The differential partial cross-section is defined as the number of electrons reaching a detector at an angle  $\theta$  with respect to the axis  $z$ , divided by the incident flux. It is convenient to express the angular dependence of the cross section in terms of Legendre polynomials; given the symmetry of wavepackets (determined by the quantum number  $l$ ) an expansion to the second order is sufficient

$$\frac{d\sigma_{\text{if}}(h\nu, \theta)}{d\Omega} = \frac{\sigma_{\text{if}}(h\nu)}{4\pi} [1 + \beta_{\text{if}}(h\nu) P_2(\cos \theta)] . \quad (1.57)$$

The angular information is entirely contained into the *asymmetry parameter*  $\beta$ . The Legendre polynomial of second degree becomes zero at  $\theta = 54.7^\circ$ : at this so-called “magic angle” the differential partial cross section becomes proportional to the integral partial cross-section.

### 1.6.2 Streaking Camera

A necessary staging post to produce ultrashort pulses was the generation of radiation with a frequency high enough, so that an attosecond pulse would contain more than one cycle [20]. Once it became possible to generate high harmonics in the XUV range and to properly filter them, the problem raised of how to characterize the pulse obtained, and how to use it to time-resolve an experiment on the attosecond time scale. Attosecond streaking [21], together with a proper algorithm for its analysis [22, 23, 24] offers a good solution to both problems. The attosecond pulse is generated in presence of a strong NIR field, used to stimulate high-harmonics emission: the delay  $\tau$  between the NIR field and the XUV pulse can be adjusted with a mirror. The idea behind streaking is to use these ingredients to characterize the XUV and the NIR pulse. If the XUV pulse is focused on a gas of atoms, it will promote some electrons to the continuum: once they are ejected, they will be accelerated by the streaking field (see Fig. 2.1) acquiring a final momentum  $p_f$  which depends on the the moment of ionization  $t_i$

$$\mathbf{p}_f = \mathbf{p}(t_i) - \mathbf{A}(t_i) , \quad (1.58)$$

where  $\mathbf{A}(t_i)$  is the vector potential of the NIR field. We will also refer to this field as “streaking field” in the following. The kinetic energy distribution of emitted electrons is measured – e.g. with a time-of-flight spectrometer – in direction parallel to the polarization of the streaking field. In this way the temporal emission profile is mapped onto an energy profile (See Fig.1.1): the mapping depends on the delay between the NIR and the XUV pulse. A *streaking spectrogram* is a set of similar energy distributions as a function of the delay (See Fig. 2.4): it clearly contains a lot of information about the pulses which generated it. With the use of a retrieval algorithm [22, 23] it is possible to characterize both fields in a very good detail, obtaining the duration and

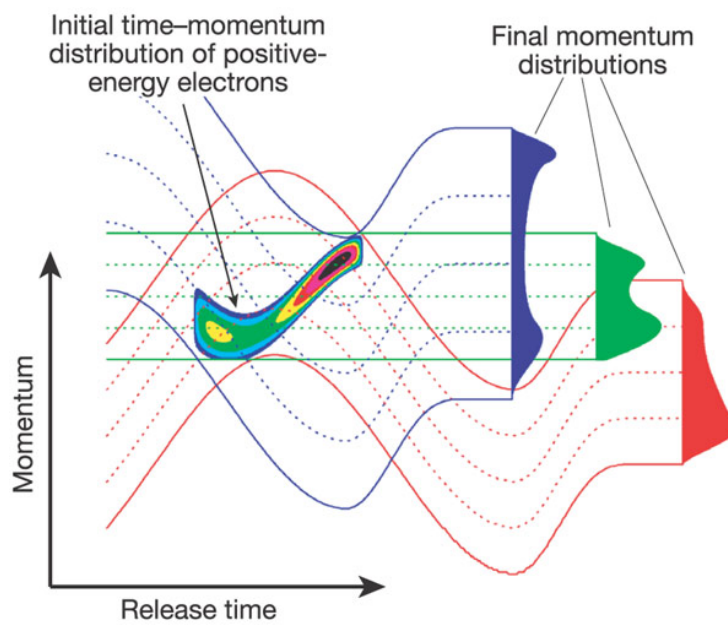


Figure 1.1: **Streaking ejected electrons.** From [25]. In the absence of the streaking field the electron momenta do not change after the ionization and their initial momentum distribution is recorded: information about the release time are lost, as the measurement implies an integration over time (green distribution). With the probing field, electrons emitted at different times feel a different acceleration according to Eq. (1.58) (red and blue distributions). From a suitable set of such tomographic projections the time-momentum distribution of electron emission can be retrieved, providing direct time-domain insight into atomic dynamics triggered by an attosecond excitation synchronized to the probing laser field.

the chirp of the XUV pulse [25] [26]. On the other hand, the very same measured spectrogram provides information about the temporal evolution of electron dynamics, encoding it into the measured energy distribution. A large part of this thesis (see Ch. 2) will be devoted to the study of electron dynamics by means of the streaking process.



## Chapter 2

# Laser-Dressed photoionization of Many-Electron Atoms

Ionizing an atom and analyzing the ejected electrons is a fundamental investigation tool, and a large amount of our current knowledge of the elements comes from ionization spectroscopy. Advancements in this field are closely connected to the technological development of laser sources. The availability of attosecond pulses has opened the possibility to perform spectroscopy on the time scale of electron dynamics [27]. Different technologies have been developed, which effectively time-resolve electron dynamics using isolated attosecond pulses [21], and trains of attosecond pulses [28]. These new regimes call for a proper modeling, and experiments unraveling new dynamics need theoretical support.

We have focused on the investigation of electron dynamics during ionization, probed by streaking measurements (see Sec. 1.6.2). This kind of experiment probes the electron on its own time-scale: we expect the complicated interaction with other electrons to affect the outcome in a relevant way. We model the ionization process taking advantage of atomic structure calculations, in order to account for multi-electron dynamics. While in usual ionization spectroscopy the angular information is contained in the  $\beta$  parameter (see Sec. 1.6.1), we expect the streaking measurement to transfer part of the non-trivial ionization dynamics into the angular distribution. We manage to calculate the ionization yield with three dimensional resolution i.e. we calculate the probability that an electron, ionized from an attosecond pulse and accelerated from the streaking field, is measured with momentum  $p$  in direction  $\mathbf{p}/p$  (see Fig. 2.1). This is accomplished in Sec. 2.1 by properly combining outgoing continuum electron waves in such a way that they give a plane wave propagating in a certain direction at the infinity. Our results show that within our numerical scheme, just few dipole matrix elements are enough to properly reproduce the entangled dynamics involved in a streaking process. However, considering the relative simplicity of our tool, we wonder to which extent it is able to predict the interplay with the streaking field during ionization. In Sec. 2.3 we dig into fine modifications of the 3D spectrum due to the strong field, comparing results of our tool with the solution of the 3D TDSE for an electron in a potential well. We point out a non-trivial modulation of the electron distribution, but at the same time the comparison shows that the Coulomb-Volkov approximation (CVA, see Sec. 1.5.2) is inappropriate if one wants to describe these fine details.

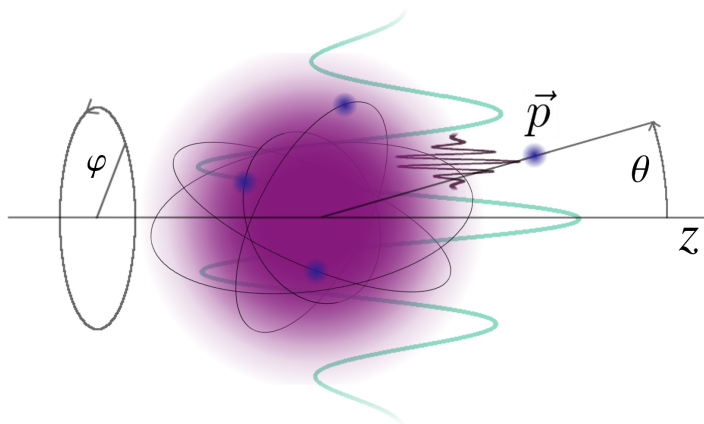


Figure 2.1: **Outline of the streaking process.** Simplistic schematic of the streaking process. The electron is ejected by the XUV pulse and accelerated by the streaking field: both fields are polarized in the  $z$  direction. Our goal is to calculate the detection probability for all angles and momenta. If the atom is spherically symmetric (e.g. noble gases) the whole system is symmetric around  $\varphi$ .

The mathematical theory that we present can be applied to every atomic system, but for our simulations we will focus on neon (Ne), which is often used in experiments. Besides its own intrinsic relevance, our model has supported some fundamental measurements. In Sec. 2.2 we report on the experiment which has questioned for the first time whether the ionization process is instantaneous or not [29]: a non-zero delay between different ionization channels was observed. We relate the group delay of the electron wavepacket to the phase of the dipole matrix elements that we calculate, achieving a direct connection between our model and the experiment. In addition to that, our simulations were used to mimic the effect of the electron lens and study its effect on the measured spectra. We also had the opportunity to compare our simulations with an experiment, where the angular distribution of streaked electrons was actually measured by means of the velocity-map imaging [30]. We have noticed some flaws in the measured data and applied different techniques to fix them; unfortunately we did not manage to achieve a direct comparison.

## 2.1 Modeling the Ionization Process

Describing the interaction of atoms and electrons with a strong field during the ionization is not a trivial task; moreover for our purposes a high degree of precision is required, and we have to limit as much as possible the use of approximations in modeling multi-electron dynamics. We derive here an expression for the laser-dressed ionization probability, where just few dipole matrix elements appear: the computational effort is extremely reduced with respect to many-electron simulations of the process. Up to which point the approximations hereafter employed still work will be studied in following sections.

Since the dipole matrix elements will be the core of our description of the interaction with the electric field, their reliability is essential. The dipole matrix elements that we use are provided from atomic structure calculations, based on the State Specific Expansion Approach (SSEA)

[31]: this is basically a multi-configuration time-dependent Hartree-Fock algorithm, where the states of the basis are carefully optimized. To describe the streaking process we have to consider the interaction with the XUV pulse  $\mathbf{E}_x(t)$ , which ionizes the atom, and with the strong (streaking) field which will accelerate the electron after the ionization. The streaking field will be represented by its vector potential  $\mathbf{A}(t)$ . We assume that both fields are linearly polarized in the same direction. Within the framework laid out in Sec. 1.2 we divide the Hamiltonian  $\hat{H}$  into an “unperturbed” part  $\hat{H}_0$ , interacting just with the laser field, and the interaction with the XUV pulse

$$\hat{V}(t) = \mathbf{E}_x(t) \hat{z}; \quad (2.1)$$

we will therefore have the propagator associated with the full Hamiltonian  $\hat{U}$  and the one associated with the Hamiltonian with no attosecond pulse  $\hat{U}_0$ . The initial state is the ground state of the atom  $|g\rangle$  and we calculate the transition probability to a final state where one electron is free  $\langle e^-, \text{ion} |$ : this final state is not unique, it determines the ionization channel. The momentum of the electron is measured, and therefore its final state is an eigenstate of the momentum operator, i.e. a plane wave  $|\mathbf{p}\rangle$ . According to Eq. (1.10), the probability to measure an electron with kinetic energy  $\frac{p^2}{2}$  in the direction  $\mathbf{p}/p$  is

$$a(\mathbf{p}) = \langle \mathbf{p}, \text{ion} | \hat{U}_0(+\infty, -\infty) | g \rangle - i \int_{-\infty}^{+\infty} dt \langle \mathbf{p}, \text{ion} | \hat{U}(+\infty, t) \hat{V}(t) \hat{U}_0(t, -\infty) | g \rangle; \quad (2.2)$$

we consider the first term to be zero, assuming that the laser pulse is not strong enough to ionize electrons via a multi-photon transition or tunneling; this assumption is equivalent to neglecting ATI electrons. Even if the laser field is not strong enough to ionize the atom, it can still polarize it: this would result in a more complicated initial state  $\hat{U}_0(t, -\infty) | g \rangle$ . For the following derivation we assume the polarizability of the atom to be negligible, it will be always the case in our investigation. Therefore, the action of  $\hat{U}_0$  on the ground state results just in a phase factor

$$\hat{U}_0 | g \rangle = e^{-i\mathcal{E}_g t} | g \rangle \quad (2.3)$$

because the ground state is an eigenstate of the atomic Hamiltonian  $\hat{H}_{\text{at}}$  with energy  $\mathcal{E}_g$ . The dipole matrix elements that we obtain from atomic structure calculations are for a final state  $|p, l, m\rangle$ , where the electron is in a continuum state of the atomic Hamiltonian  $\hat{H}_{\text{at}}$ : to take advantage of them we must express the final state appearing in the integral in Eq. (2.2) in terms of continuum waves  $|p, l, m\rangle$ . Let us analyze this state, including the evolution from  $t$  to the infinity with the full propagator, and let us consider its Hermitian conjugate:  $\langle \mathbf{p}, \text{ion} | \hat{U}(+\infty, t) = (\hat{U}(t, +\infty) | \mathbf{p}, \text{ion} \rangle)^*$ . The expression in brackets represents a plane wave (back) propagated against the atom. In Sec. 1.4.3 we have reported the well-known combination of continuum states giving a scattering state. For the moment we ignore the presence of the NIR field, and we introduce the propagator of the atomic Hamiltonian  $\hat{U}_{\text{at}}$ . With this propagator, the state of the electron in the vicinity of the scatterer – which is the relevant region for the calculation of dipole matrix elements – has the form of a scattering state:

$$\hat{U}_{\text{at}}(t, +\infty) | \mathbf{p} \rangle = \frac{1}{2k} \sum_l i^l (2l+1) e^{-i\delta_l} P_l(\mathbf{p}/p) | p_l \rangle, \quad (2.4)$$

we have used the decomposition of  $\psi^-$  in Eq. (1.49) because the wave is back-propagated. States  $|p_l\rangle$  are exact eigenstates of the atomic Hamiltonian  $H_{\text{at}}$  obtained from the SSEA. Extracting phase shifts  $\delta_l$  is not trivial: the SSEA code calculates the continuum wavefunction, and then compares its phase with the expected  $\zeta_l$  Eq. (1.39) extracting the difference  $\Delta$ . The total phase shift is  $\delta_l = \zeta_l + \Delta$ . The final step is to express Eq. (2.4) in terms of spherical harmonics [5]

$$\hat{U}(t, +\infty) |\mathbf{p}\rangle = \sum_{l,m} c_{l,m} |p, l, m\rangle, \quad (2.5)$$

where  $c_{l,m} = \frac{4\pi}{2k} i^l Y_{l,m}^*(\mathbf{p}/p) e^{-i\delta_l}$ . We have thus achieved our goal and decomposed the final state in continuum eigenstates of the atomic Hamiltonian; Eq. 2.5 is the key to a three dimensional description of streaking. Eq. 2.4 provided us with the propagation of the plane wave against the atom neglecting the streaking field; on the other hand, a free electron accelerated by an electric field is described by a Volkov wave (see Sec. 1.5). Our ansatz is to combine the two approaches, in a way similar to the Coulomb-Volkov approximation (CVA). We will account for the NIR pulse – assuming it starts interacting with the electron at the moment of ionization  $t$  – approximating the final state with a Volkov state  $|\mathbf{p} + \mathbf{A}\rangle e^{i\phi(\mathbf{p}, t)}$  (see Sec. 1.5). The interaction with the other electrons are neglected, starting from the moment of ionization.

Now we have to analyze a bit more in detail the quantum expression of the ground state  $|g\rangle$  and of the final state  $\langle e^-, \text{ion} |$ . The atomic ground state is fully described by its azimuthal and magnetic quantum number,  $|L_{\text{at}}, M_{\text{at}}\rangle$ . For the ionized state we drop the momentum of the electron  $p$  in the following discussion, focusing on its angular numbers. Having two particles we have different options: the first one is to separately characterize the free electron with quantum numbers  $l, m$  and the ion with  $L_{\text{ion}}, M_{\text{ion}}$ . However, the two-particle quantum state with  $l, L_{\text{ion}}$  fixed can be decomposed on a second basis using the total angular numbers of the composed system ( $e^- + \text{ion}$ ), i.e.  $L_{\text{tot}}$  and  $M_{\text{tot}}$ . The two bases are connected by Clebsch-Gordan coefficients:

$$\begin{aligned} |l, L_{\text{ion}}, L_{\text{tot}}, M_{\text{tot}}\rangle &= \sum_{m, M_{\text{ion}}} \langle l, L_{\text{ion}}, m, M_{\text{ion}} | l, L_{\text{ion}}, L_{\text{tot}}, M_{\text{tot}}\rangle |l, L_{\text{ion}}, m, M_{\text{ion}}\rangle \\ &= \sum_{m, M_{\text{ion}}} G_{m M_{\text{ion}} L_{\text{tot}} M_{\text{tot}}}^{l L_{\text{ion}}} |l, L_{\text{ion}}, m, M_{\text{ion}}\rangle. \end{aligned} \quad (2.6)$$

For our purposes it is more convenient to compose the plane waves Eq. (2.5) on the first basis, but to calculate the transition for a final states expressed on the second basis using total quantum numbers. To this aim we will use the following decomposition:

$$\begin{aligned} \langle l, m, L_{\text{ion}}, M_{\text{ion}} | \hat{z} | L_{\text{at}}, M_{\text{at}} \rangle &= \\ &= \sum_{L_{\text{tot}}, M_{\text{tot}}} \langle l, m, L_{\text{ion}}, M_{\text{ion}} | l, L_{\text{ion}}, L_{\text{tot}}, M_{\text{tot}} \rangle \langle l, L_{\text{ion}}, L_{\text{tot}}, M_{\text{tot}} | \hat{z} | L_{\text{at}}, M_{\text{at}} \rangle \\ &= \sum_{L_{\text{tot}}, M_{\text{tot}}} G_{m M_{\text{ion}} L_{\text{tot}} M_{\text{tot}}}^{l L_{\text{ion}}} \langle l, L_{\text{ion}}, L_{\text{tot}}, M_{\text{tot}} | \hat{z} | L_{\text{at}}, M_{\text{at}} \rangle. \end{aligned} \quad (2.7)$$

We now have all the ingredients to write explicitly the dipole matrix elements providing angular

resolution:

$$\begin{aligned} D(\mathbf{p}, L_{\text{ion}}, M_{\text{ion}}, L_{\text{at}}, M_{\text{at}}) &= \langle \mathbf{p}, L_{\text{ion}}, M_{\text{ion}} | \hat{U}(+\infty, t) \hat{z} | g \rangle \\ &= \sum_{\substack{l, m, \\ L_{\text{tot}}, M_{\text{tot}}}} G_{m M_{\text{ion}} L_{\text{tot}} M_{\text{tot}}}^{l L_{\text{ion}}} c_{lm}^* \langle l, L_{\text{ion}}, L_{\text{tot}}, M_{\text{tot}} | \hat{z} | L_{\text{at}}, M_{\text{at}} \rangle, \end{aligned} \quad (2.8)$$

where  $\langle l, L_{\text{ion}}, L_{\text{tot}}, M_{\text{tot}} | \hat{z} | L_{\text{at}}, M_{\text{at}} \rangle$  are the matrix elements that we obtain from multi-electron atomic structure calculations. The summation in Eq. (2.8) actually runs over a smaller set of quantum numbers: dipole selection rules restrict the possible final states, and Clebsch-Gordan coefficients are non-zero just for some combination of angular quantum numbers. We will discuss in detail the allowed transitions for specific cases.

Using Eq. (2.8) and the Coulomb Volkov approximation, we rewrite the probability amplitude Eq. (2.2) in a form which allows a direct numerical calculation:

$$a_{i,f}(\mathbf{p}) = -i \int_{-\infty}^{+\infty} dt D_{i,f}(\mathbf{p} + \mathbf{A}(t)) E_x(t) e^{-i\mathcal{E}_g t} e^{-i\phi(\mathbf{p}, t)}, \quad (2.9)$$

where we have shortened the initial and the final state of the ion with *i* and *f*. In principle the integration extends from  $-\infty$  to  $\infty$ , but for all practical purposes its extrema coincide with those of the envelope of the XUV pulse  $E_x$ . For simplicity we can consider this envelope to be always peaked on  $t = 0$ ; in order to simulate streaking we will consider different delays  $\tau$  of the XUV pulse with respect to the NIR pulse, using the shifted field  $E_x(t - \tau)$ . With this convention, a positive delay corresponds to delaying the XUV pulse w.r.t the streaking field. The transition probability  $s$  is the modulus square of the probability amplitude,

$$s_{i,f}(\mathbf{p}, \tau) = \left| \int_{-\infty}^{+\infty} dt D_{i,f}(\mathbf{p} + \mathbf{A}(t)) E_x(t - \tau) e^{-i\mathcal{E}_g t} e^{-i\phi(\mathbf{p}, t)} \right|^2, \quad (2.10)$$

and the actual probability  $S$  of observing an electron in a final state  $|\mathbf{p}\rangle$  is given by the sum over all possible final states of the ion:

$$S(\mathbf{p}, \tau) = \sum_f s_{i,f}(\mathbf{p}, \tau). \quad (2.11)$$

Note that all phase term in Eq. (2.10) not depending explicitly on time are canceled by the modulus.

The integral Eq. (2.10) is calculated numerically using an algorithm for rapidly oscillating functions. The quantity  $S(\mathbf{p}, \tau)$  is the streaking spectrogram (see Sec. 1.6.2), which we can process with the very same tools used to analyze the measured ones.

### 2.1.1 Neon

We have applied our analysis to the laser-dressed photionization of neon. It is frequently used in experiments, being a noble gas and thus remaining stable during the measurement; in addition

to that, it has a relatively high photoionization cross-section (see Fig. 2.2) resulting in a good signal-to-noise ratio. Binding energies  $E_b$  of outer shells are

$$\begin{aligned} E_b(2s) &= 1.78 = 48.46 \text{ eV} , \\ E_b(2p) &= 0.79 = 21.56 \text{ eV} , \end{aligned} \quad (2.12)$$

the difference of energy between the  $2s$  and the  $2p$  channel is

$$E_b(2s) - E_b(2p) \sim 27 \text{ eV} : \quad (2.13)$$

this allows a good resolution of these two channels in an ionization experiment, even if the bandwidth of the ionizing pulse is as large as  $\sim 10$  eV, which is common for an isolated attosecond pulse. At the same time neon is a relatively simple atom, having ten electrons and only shells of types  $s$  and  $p$ . We have numerically estimated the polarizability of neon, solving the (TDSE) on the basis of the eigenstates of  $H_{\text{at}}$  in the presence of the NIR pulse only: we have observed a negligible effect ( $\leq 0.01\%$ ), and we have excluded polarization effects and Stark shift due to the streaking field.

We consider ionization from the ground state, its electronic configuration in the outer shell is  $|g\rangle = |2s^2 2p^6\rangle$ . All the shells are complete and the atom has spherical symmetry: in terms of total angular momentum the ground state is  $|g\rangle = |L_{\text{at}} = 0, M_{\text{at}} = 0\rangle$ . For a dipole transition, selection rules restrict the allowed  $L_{\text{tot}}$  and  $M_{\text{tot}}$  of the final state. The transition  $0 \rightarrow 0$  is forbidden, therefore  $L_{\text{tot}} = 1$ ; since we are considering linear polarization of the field, total  $M$  is conserved and  $M_{\text{tot}} = 0$ . Thus, the angular quantum numbers of the final state happen to be uniquely defined. From the properties of the Clebsch-Gordan coefficients we derive some rules regarding the quantum numbers of the electron and the ion:

$$\begin{cases} |L_{\text{ion}} - l| \leq 1 \\ L_{\text{ion}} + l \geq 1 \\ m + M_{\text{ion}} = 0 \end{cases} . \quad (2.14)$$

Let us write explicitly all the states that belong to this subspace.

- $L_{\text{ion}} = 0$

This implies that also  $M_{\text{ion}} = m = 0$ , and from the second of Eqs. (2.14)  $l = 1$ . This final state corresponds to ionization from the  $s$ -shell, and to an outgoing electron in wave  $p$ .

**Final State:**  $|l = 1, L_{\text{ion}} = 0\rangle \equiv |2s 2p^6, e^- p\rangle$

- $L_{\text{ion}} = 1, M_{\text{ion}} = \pm 1$

Which implies  $m = \mp 1$ . The two cases contribute exactly in the same way. According to the Eqs. (2.14)  $l$  can be either 1 or 2. However, here the ionization occurs in the  $p$  shell, since the ion is left with  $L_{\text{ion}} = 1$ : therefore  $l = 1$  is forbidden because  $\Delta l \neq 0$ .

**Final State:**  $|l = 2, L_{\text{ion}} = 1\rangle \equiv |2s^2 2p^5, e^- d\rangle$

- $L_{\text{ion}} = 1, M_{\text{ion}} = 0$

Also in this case  $l = 1$  has to be discarded, for the same reason of the previous point; on

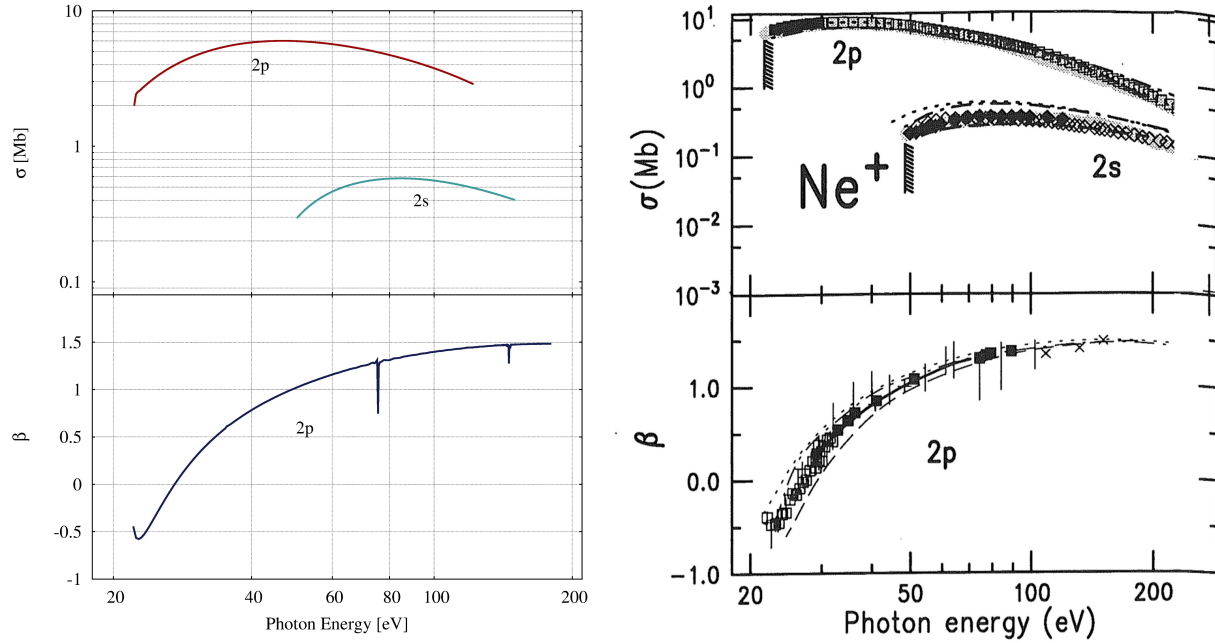


Figure 2.2: **Cross Section and  $\beta$ -parameter.** Comparison of the cross section  $\sigma$  and  $\beta$  parameter from SSEA data elaborated with our model (left panel) and from literature (right panel). The right panel is taken from [32], data points are the result of different experiments cited therein. Imperfections in the  $\beta$ -parameter come from numerical noise in the calculation of phases  $\delta_l$ .

the contrary  $l = 0$  is allowed because  $m = 0$ . This is the only case where the summation in Eq. (2.8) runs over more than one state: the dipole matrix elements will result from the interference of the two outgoing electron waves  $s$  and  $d$ .

**Final States:**  $|l = 0, L_{\text{ion}} = 1\rangle \equiv |2s^2 2p^5, e^-s\rangle$  and  $|l = 2, L_{\text{ion}} = 1\rangle \equiv |2s^2 2p^5, e^-d\rangle$

All the dipole matrix elements for these final states are obtained in multi-electron atomic structure calculations, together with phase shifts  $\delta_l$ : they are then suitably summed according to Eq. (2.8).

Our calculations are supposed to be quite accurate, and it is a primal request that they correctly reproduce known results of neon: we compare the cross sections obtained with our model with those measured in past experiments. The comparison of the partial cross section (see Sec. 1.6.1) involves just the modulus squared of dipole matrix elements. Nonetheless it is an important verification because it is done at the “magic” angle, and it is therefore sensitive to the way we obtain the angular dependent dipole matrix element; for the  $2p$ -channel the composition of different waves is crucial in determining the cross section at angles different from  $\theta = 0$ . Our tool reproduces very well the expected result, see Fig. 2.2. Even more meaningful is the comparison of the  $\beta$ -parameter which fully characterizes the angular distribution of ejected electrons. The very good agreement that we show in Fig. 2.2 is a strong validation of our approach: in fact this not only means that the mathematical theory of the previous section is correct, it also confirms that dipole matrix elements and phase-shifts  $\delta_l$  are very accurate. As we will see in the following, these phase-shifts play a very important role in the dynamics: we have tried to recalculate the  $\beta$ -parameter with some synthetic, wrong  $\delta_l$ , and observed that their degree of accuracy must

be quite high in order to provide meaningful results.

## 2.2 Delay in Photoemission

We have now a certain confidence in our model and in its applicability. In this section we will see how the correct calculation of dipole matrix elements Eq. (2.8) can already provide a fundamental insight into electron dynamics: it holds relevant pieces of information regarding the time response of the electron to the field during photoionization. These dynamics take place on an attosecond time-scale and measuring them is extremely challenging; however, already two different experiments have pushed the frontiers of research on these grounds, using attosecond streaking on neon [29] and RABBIT on argon [28]. These experiments point out a delay between different ionization channels: within our scheme we predict a delay for neon qualitatively similar to [29], but three times smaller than the measured one.

In the two years between the publication of the experimental result and now, many independent theoretical groups have tried to estimate the delay. An R-matrix approach is reported in [33], and electron correlations were taken into account within the random phase approximation in [34]; the discrepancy is slightly smaller than the one obtained in our scheme, but remains relevant. Several explanations have been suggested to account for the difference, all of them involving the contribution of the streaking field in affecting the measured delay. A possibility which we have immediately considered was the interplay of the intense laser field and the atomic potential, during the electron motion after ionization – usually referred to as “Coulomb-laser coupling”. It is indeed a weak point of our modeling not to take this interaction fully into account (it is approximated with the CVA instead). A paper was published [35], pointing out the possibility of a delay due to the combined effect of the field and Coulomb forces. A very recent paper, taking advantage of the exact solution of the TDSE for helium, discusses which information about the coupling of the field with bound and continuum states can be retrieved from streaking spectroscopy [36]. The effect of the field in polarizing initial and final states was also investigated by different groups. It was shown responsible for a big delay between two ionization channels in hydrogen [37]; however, we have already excluded the polarization to play any role in neon, because of its low polarizability. An interesting publication on the subject, which analyzes the question whether the streaking measurement can be disentangled from the process it measures is [38].

In my opinion, the complicated interaction between the ejected electron and the parent ion, taking place in the strong electric field, is likely to change the delay of few attoseconds. On the other hand, the measurement represents the current boundary of the timing of electron motion: the standard deviation reported from the measurement is 25% of the measured delay, and leaves quite some room for future adjustments. However, already two years after the publication, a non-zero delay in photoemission is almost certain: this is an extremely good achievement for such a groundbreaking, delicate experiment. I find important exactly the fact that such a fundamental effect has been detected, and that its investigation still requires improvement both on the theoretical and experimental side. This situation usually fosters a lot of good research, as has already happened in the last two years.



### 2.2.1 The Phase of Dipole Matrix Elements

Let us see how it is possible to extract information about the time evolution of the ionization process from the dipole matrix elements. The relation between their phase and the group delay of the emitted electron wavepacket has been discussed in [39, 40] and in detail in the SOM of [29], on which we base the subsequent discussion. For the moment let us consider the ionization through the interaction with the XUV pulse ignoring the NIR pulse; let  $|\psi(t)\rangle$  be the state of the composite system (electron + ion) at time  $t$ , with energy  $\left(\frac{p^2}{2} + \mathcal{E}_{\text{ion}}\right)$ . In this simplified case we can rewrite Eq. (2.9) in the following way (the Volkov phase reduces to the kinetic energy of the electron):

$$\langle \mathbf{p}, \text{ion} | \psi(t) \rangle = -i \int_{-\infty}^t dt' D(\mathbf{p}) E_x(t') e^{-i(t-t')\left(\frac{p^2}{2} + \mathcal{E}_{\text{ion}}\right)} e^{-it' \mathcal{E}_g}. \quad (2.15)$$

Considering a time  $t$  after the end of the interaction with the XUV pulse, the upper extreme of the integral above can be extended to  $+\infty$  without changing the result: we can thus express the result in terms of the Fourier transform of the XUV pulse  $\tilde{E}_x$ ,

$$\langle \mathbf{p}, \text{ion} | \psi(t) \rangle = -i D(\mathbf{p}) \tilde{E}_x \left( \frac{p^2}{2} + W \right) e^{-it\left(\frac{p^2}{2} + \mathcal{E}_{\text{ion}}\right)}, \quad (2.16)$$

where  $W = \mathcal{E}_{\text{ion}} - \mathcal{E}_g$  is the ionization potential. We can use this expression to write explicitly the decomposition of the global wavefunction on continuum states:

$$\begin{aligned} \psi(\mathbf{r}, t) = \langle \mathbf{r} | \psi(t) \rangle &= \int d^3\mathbf{p} \langle \mathbf{r} | \mathbf{p} \rangle \langle \mathbf{p} | \psi(t) \rangle = \\ &= -i \int d^3\mathbf{p} \langle \mathbf{r} | \mathbf{p} \rangle e^{-it\left(\frac{p^2}{2} + \mathcal{E}_{\text{ion}}\right)} D(\mathbf{p}) \tilde{E}_x \left( \frac{p^2}{2} + W \right). \end{aligned} \quad (2.17)$$

In this form, the relation between the phase of a dipole matrix element and a delay in the formation of an electron wavepacket is more evident. Let us assume for example that the phase of  $D(\mathbf{p})$  change with the kinetic energy of the electron,

$$D(\mathbf{p}) = |D(\mathbf{p})| e^{i\alpha \frac{p^2}{2}}; \quad (2.18)$$

the effect of such a phase on the photoelectron density can be written as

$$|\psi(\mathbf{r}, t)|^2 = \left| \int d^3\mathbf{p} \langle \mathbf{r} | \mathbf{p} \rangle e^{-i\frac{p^2}{2}(t-\alpha)} D(\mathbf{p}) \tilde{E}_x \left( \frac{p^2}{2} + W \right) \right|^2, \quad (2.19)$$

i.e. equivalent to that of delaying the wavepacket by  $\alpha$ . Using the same ansatz Eq. (2.18) for the dipole phase, we can also show that it will result in a shift of the spectrogram, if we include the streaking field. For simplicity let us assume a monochromatic, linearly-polarized streaking field  $A(t) = A_0 \cos(\omega t)$ , and the detection direction to be parallel to the polarization of the field: the momentum  $\mathbf{p}$  will then coincide with its modulus  $p$ . Let us rewrite Eq. (2.10) in this case, neglecting terms proportional to  $A_0^2$ ,

$$s(p, \tau) \approx \left| \int_{-\infty}^{+\infty} dt |D(p + A(t))| E_x(t - \tau) e^{i\left(\frac{p^2}{2} + W\right)t} e^{ipA_0\left(\alpha \cos(\omega t) + \frac{1}{\omega} \sin(\omega t)\right)} \right|^2; \quad (2.20)$$

all phase terms not independent on  $t$  are canceled by the modulus. We can see the last term as a time shift in the streaking field:

$$\alpha \cos(\omega t) + \frac{1}{\omega} \sin(\omega t) = \sqrt{\alpha^2 + \frac{1}{\omega^2}} \sin(\omega t + \arctan(\alpha\omega)) = \frac{\sqrt{1 + \alpha^2\omega^2}}{\omega} \sin(\omega(t + \tilde{\alpha})), \quad (2.21)$$

which we can rewrite as the integral of  $A(t + \tilde{\alpha})$ , with the time shift

$$\tilde{\alpha} = \frac{1}{\omega} \arctan(\alpha\omega) \approx \alpha. \quad (2.22)$$

Changing the integration variable in Eq. (2.21), it becomes evident that the spectrogram is shifted:

$$s(p, \tau) \approx \left| \int_{-\infty}^{+\infty} dt |D(p + A(t - \tilde{\alpha}))| E_x(t - \tau - \tilde{\alpha}) e^{i\left(\frac{p^2}{2} + W\right)t} e^{-ip\sqrt{1+\alpha^2\omega^2} \int_t^{+\infty} dt' A(t')} \right|^2. \quad (2.23)$$

In general the dependence of the dipole phase on the energy is non-linear: we define the group delay as

$$\alpha(\mathcal{E}) = \frac{d}{d\mathcal{E}} \arg [D(\sqrt{2\mathcal{E}})]. \quad (2.24)$$

The purpose of this section was to give a hint of how the phase of the dipole matrix elements plays a fundamental role in a streaking measurement. A genuine research on the subject, unveiling what is actually possible to retrieve from a streaking spectrum was published in [41].

### 2.2.2 Attosecond Streaking on Neon

The previous section demonstrates that the energy derivative of the quantum phase, which is closely related to the Wigner-Smith time delay [39, 42], can now be accessed by a time-resolved measurement of ionization; in return, a careful calculation of the dipole phase is the first step toward the theoretical modeling of a measurement of photoemission delay. In Fig. 2.3 we show the group delay defined in Eq. (2.24) from dipole matrix elements that we calculate, evaluated in the direction of the polarization of the laser (i.e.  $\mathbf{p}$  parallel to  $\mathbf{A}$ ). As discussed in Sec. 2.1.1, the ionization from the  $2s$ -shell corresponds to the final state  $|l = 1, L_{\text{ion}} = 0\rangle$ ; since we are interested in the direction of polarization, an outgoing  $d$  wave does not give any contribution and the ionization from the  $2p$ -shell corresponds to the final state  $|l = 0, L_{\text{ion}} = 1\rangle$ . Our model predicts a net time difference of few attoseconds between the electron ejected from the  $2p$ - and  $2s$ -shells. These results were used for direct comparison in [29], which reports streaking measurements of photoemission delay in neon. In the experiment, photoelectrons ejected from Ne atoms by 106-eV attosecond pulses and streaked by the electric field of near-single-cycle NIR pulses were recorded with a time-of-flight spectrometer versus the delay between the XUV and NIR pulses. To improve the signal-to-noise ratio of the electrons emitted from the  $2s$ -shell, the electron spectrometer was equipped with an electrostatic lens, enhancing electron counts in the spectral range between 40 and 70 eV. Electric fields were reconstructed from the spectrogram by the use of an algorithm, based on frequency-resolved optical gating (FROG) [22] [43]. An example of a

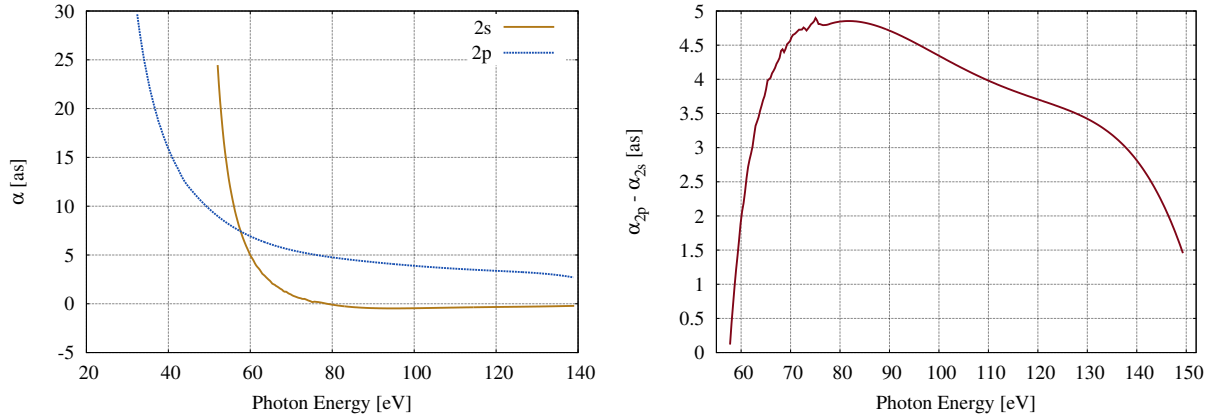


Figure 2.3: **Group delay in neon.** In the left panel the group delay of  $2s$  and  $2p$  dipole matrix elements of neon is shown: they are calculated in the framework discussed in Sec. 2.1. Phases had to be smoothed in order to calculate the derivative, because they contained some small numerical noise from atomic structure calculation. The right panel shows the difference between the group delays, which is supposed to result in a net time gap between the photoemission from the two shells. A little bit of numerical noise is still visible.

recorded streaking spectrogram is showed in Fig. 2.4: the shift between the  $2s$  and  $2p$  line provides a measurement of the delay. The streaking measurement was repeated many times, with sub-200 as XUV pulse, but also with longer pulses ( $\sim 400$  as) in order to spectrally resolve and exclude satellites from the analysis. The result of the experiment is reported in Fig. 2.5, a delay of  $21 \pm 5$  as was observed.

Our calculations predict a delay of  $\sim 4.5$  as for the photon energy used in the experiment. Intuitively, one expects that a delay in the formation of a wave packet causes a corresponding temporal shift of the streaking spectrogram. This holds true within the CVA (see Sec. 1.5.2). However, numerical simulations of the TDSE with an effective potential resulted in spectrograms shifted with respect to each other by 6.8 as, even though the difference in group delay was the same. The origin of this discrepancy lies in the fact that the photoelectron interacts with both the streaking field and the ion, resulting in a quantum motion that is not exactly described by known analytical approaches. Thus, for the current experimental parameters, the small deviations between the electrons exact motion and that modeled via the CVA give rise to a 2 as discrepancy in the relative delay. The difference between the theory and the experiment remains relevant. Many other independent groups, using different theoretical models, have obtained a delay between 7 and 10 as [33] [34]. Even though there is not yet a good agreement between theory and experiment, for us these other theoretical results are very important. The simulations used to obtain them are much more sophisticated than our tool, which is based on just a few dipole matrix elements: the good agreement with our result is a success for the theory derived in Sec.2.1.

Concerning the measurement, some doubts have raised about a possible systematic error introduced by the electron lens. The possibility that the measured shift of spectrograms could be affected by the electron lens was indeed carefully checked. We carried out simulations with the very tool described in Sec. 2.1, where the spectrogram was obtained from the integration of

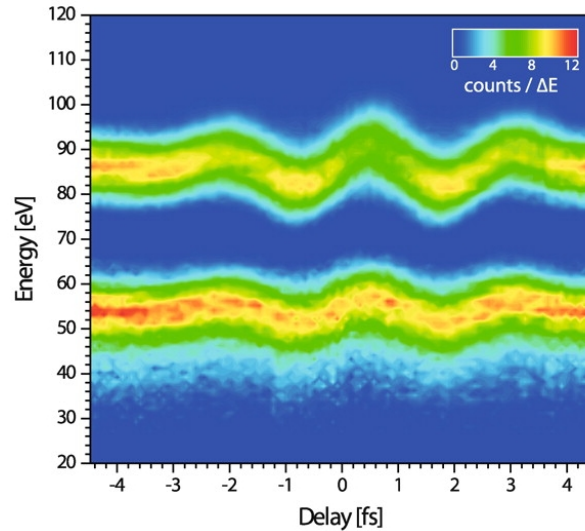


Figure 2.4: **Streaking spectrogram.** From [29]. Example of a streaking measurement on neon. The spectrograms are composed of a series of photoelectron energy spectra recorded by releasing  $2s$  and  $2p$  electrons from Ne with an attosecond XUV pulse in the presence of a strong NIR few-cycle laser field, as a function of the delay between the XUV and NIR fields.

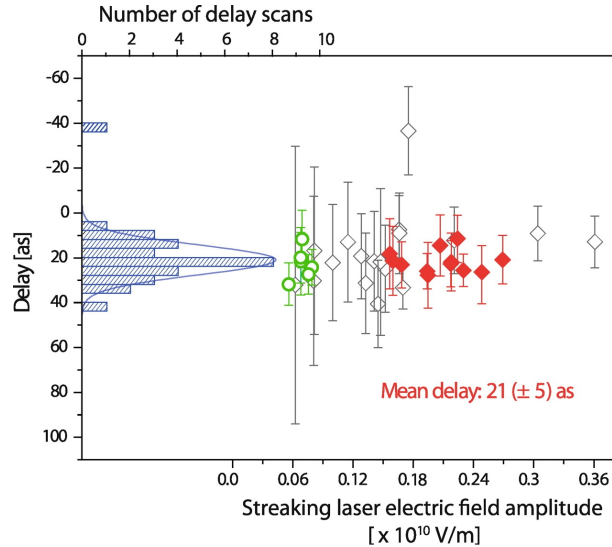


Figure 2.5: **Delay measurement.** From [29]. The relative delay between photoemission from the  $2p$ - and  $2s$ -shell of Ne atoms, induced by sub-200 as, near-100 eV XUV pulses. From the analysis of a set of spectrograms, the measured delays and associated retrieval uncertainties are plotted against the amplitude of the vector potential applied in the attosecond streak camera. Spectrograms measured in the presence of a satellite attosecond pulse were found to exhibit a less accurate retrieval of the delay value. When a subset of data (red diamonds) that represents scans with less than 3% satellite pulse content was evaluated, a mean delay value of 21 as with a standard deviation of  $\sim 5$  as was found. The green circles represent the result of analyzing spectrograms recorded with an XUV pulse with narrower bandwidth in order to exclude the potential influence of shakeup states contributing to the electron kinetic energy spectrum.

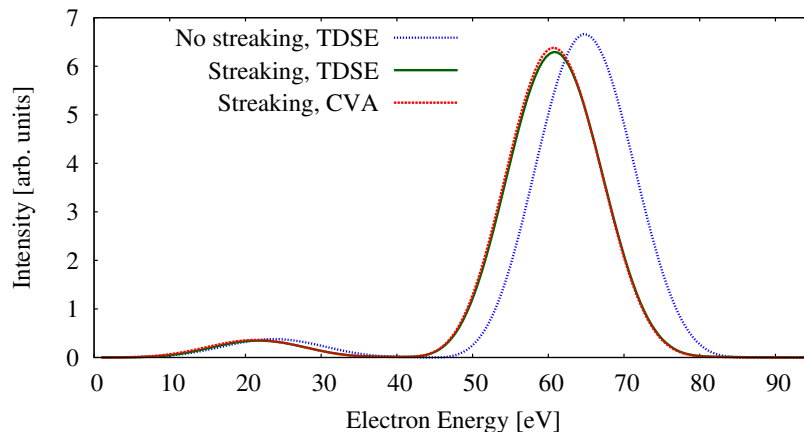


Figure 2.6: **Comparison of helium spectra.** Electron spectra for laser-dressed photoionization in helium, comparing our model based on the CVA and the exact solution of the TDSE [45].

the signal over a certain angle, in order to mimic the effect of the lens: these spectrograms were subsequently analyzed with the same process used for the measured ones, and the conclusion was that the angular integration did not introduce any shift. Recently, a careful investigation was carried on, studying the combined effect of the chirp present in the pulse, and the electron lens [44]. This characterization was not performed on the beamline used to measure the delayed photoemission, and also a different electron lens was used; nonetheless, a shift of the spectrogram due to the combination of the chirp and the lens was measured. It is not clear whether the electron lens has played any role in the experiment on neon. Thanks to technological improvements, it is now possible to repeat the experiment with an XUV pulse strong enough to make the use of the electron lens unnecessary: hopefully experiments in the near future will clarify the question.

## 2.3 Angular Streaking

The value of the delay calculated with our tool is in very good agreement with more refined multi-electron calculation. We have also run some calculations for the helium atom, because we had the opportunity to compare them with the exact solution of the TDSE <sup>1</sup>. The comparison showed in Fig. 2.6 is another proof that our simple tool performs very well in describing photoionization spectra. We want to investigate, up to which level of detail we can trust our calculations. We expect the interaction of the ejected electron with both the parent ion and the streaking field, to be the weak point of the model: we look for small modulations in electron distributions due to the streaking field, beyond the expected shift of momenta.

With our tool we are able to simulate streaking in three dimensions. We will apply it again to neon, whose ground state is spherically symmetric: the electron distribution will therefore have cylindrical symmetry, i.e. in reference to Fig. 2.1 it will not depend on  $\varphi$ . The problem is thus

<sup>1</sup>We are grateful to J. Burgdörfer, J. Feist, S. Nagele and R. Pazourek for providing us with results of their precious tool [45].

reduced to the study of a two-dimensional distribution (in momentum space), in the plane  $\varphi = 0$ : an example of such a distribution is reported in Fig. 2.10 (left panel). We will use both polar coordinates  $(p, \theta)$  and Cartesian coordinates  $(p_x, p_z)$  to describe the momentum distribution. The  $2p$  ionization line is the result of a non trivial interference of two channels and we will focus on its angular distribution, neglecting the  $2s$ : an additional reason is that there is no way to resolve the  $2s$  signal in the experiment, since it is very weak and covered by the ATI signal. The most evident effect of the streaking field will be to move the electron distribution in momentum space along the axis parallel to the polarization of the field. Let  $t$  be the moment of ionization, at  $t_f$  after the pulse is gone the momentum is  $p_z(t_f) = p_z(t) - A(t)$ . Our study wants to go beyond this classical effect. As discussed in previous sections, the ionization is a multi-electron phenomenon described by the dipole matrix element  $D(\mathbf{p})$ , and the interaction with the streaking field depends on both modulus and phase of this quantity. In principle this dependence should modulate the electron distribution according to the delay between the attosecond pulse and the streaking field. However, it is unclear whether describing the interaction with the streaking field by means of the Coulomb-Volkov approximation, accounts for such fine details. To answer this question, we need to define a figure of merit to isolate and quantify modulations due to the streaking field. A common choice to characterize a spatial distribution is to use the asymmetry parameter, which highlights modulations occurring in the electron count  $C$  in opposite directions. Formally it is defined as

$$\mathcal{A} = \frac{C_{\hat{v}} - C_{-\hat{v}}}{C_{\hat{v}} + C_{-\hat{v}}}, \quad (2.25)$$

where  $\hat{v}$  indicates a direction and  $-\hat{v}$  the opposite one w.r.t the center of the coordinate system. The asymmetry parameter is normalized to the total number of counts, and is zero if the counts are the same in the two directions. It would indeed be a relevant parameter for our purposes: it is zero in the absence of the streaking field and highlights to which extent the number of counts changes otherwise. We intentionally did not specify what we take as opposite directions: we actually have different choices. We can consider the number of electrons flying beneath an angle interval  $\theta_0 \pm \frac{\Delta\theta}{2}$  and compare them with those flying toward  $\theta_0 + \pi \pm \frac{\Delta\theta}{2}$  (Fig. 2.7, left panel). In this case the number of count is affected by the vertical shift of the distribution: in order to avoid artifacts, one should shift the origin of the system of coordinates in such a way that it matches the center of the electron distribution. It is not easy to follow this prescription for the analysis of experimental data, where the determination of the center of mass of the distribution suffers from experimental noise. A solution to this problem is to consider the number of electrons with a certain horizontal component of the momentum  $p_{x0} \pm \frac{\Delta p_x}{2}$  and calculate the asymmetry between those flying toward positive and negative values of  $p_z$  (Fig. 2.7, right panel).

To assess the validity of the Coulomb-Volkov approximation in correctly predicting these dynamics, we have compared the results of our model with the numerical solution of the TDSE<sup>2</sup>. Our tool is indeed more reliable in describing multi-electron dynamics, since the TDSE is solved for a single electron in a pseudo-potential; however, in the TDSE propagation, the interaction with the fields is exact. In order to compare just the effect of the field after the ionization, we

---

<sup>2</sup>We are grateful to N. Karpowicz for providing us with results of the TDSE of a single electron in a pseudo-potential, solved in three dimensions.

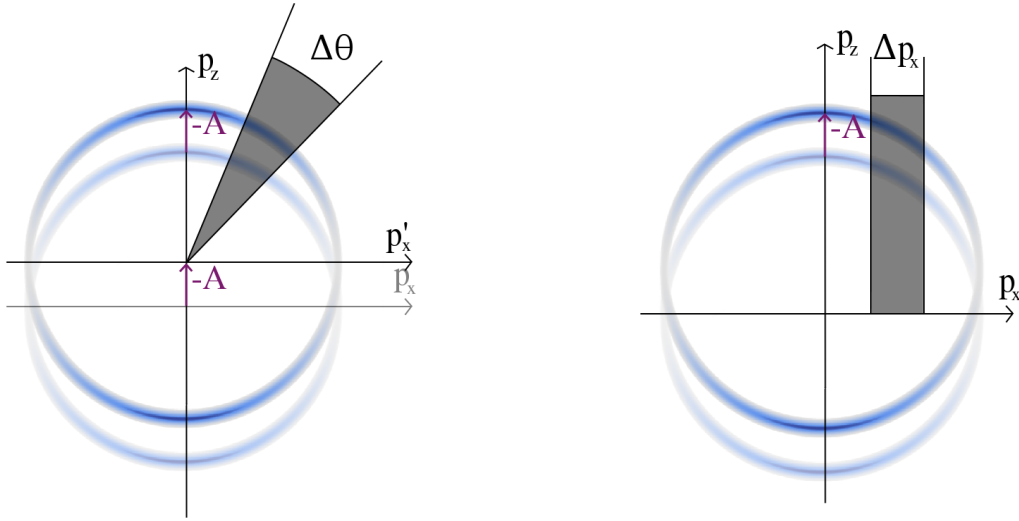


Figure 2.7: **Different definitions of the asymmetry parameter.** Calculating the asymmetry from an angular section (left panel) is potentially harmful: the shift due to the streaking field modifies the number of counts falling in this area for a pure geometrical reason. A proper shift of the frame of reference neutralizes this artifact, as shown in the figure. If instead the number of counts is defined starting from a rectangular area (right panel), the shift has no impact on the asymmetry.

have taken dipole matrix elements from TDSE calculations and used them in our code. We calculate the asymmetry parameter for  $\theta = 0$  as a function of the delay  $\tau$  between the XUV and the NIR pulse and show the comparison in Fig. 2.8. The amplitude of the asymmetry is the same in both cases; interestingly, a phase shift occurs, marking the inadequacy of the Coulomb-Volkov approximation in describing fine details of the interaction of the electron with the field.

### 2.3.1 Analysis of Experimental Data

Streaking measurement with a 3D resolution of electrons momenta are actually feasible, by means of the attosecond Velocity Map Imaging (VMI) [30]: this technique consists in focusing the streaked electrons against a screen detector (MCP-phosphor) which records their momenta (for details see [46]). The schematic of the VMI detector is outlined in Fig. 2.9. The VMI is better applied on symmetric atoms: in this case it is possible to reconstruct the 3D distribution from the 2D one, recorded on the screen. This is obtained with an iterative procedure based on the Abel inversion [47]. We have had access to attosecond VMI data for neon, and we have analyzed them in order to evaluate the asymmetry. An example of an electron distribution recorded from the VMI is showed in Fig. 2.10, in comparison with a result of our simulations. An ATI trace is present for low energies, and it extends up to the signal from the  $2p$  channel. The ionization from the  $2s$  shell is therefore not visible in the experimental data. Also the signal from the  $2p$  shell is not easy to isolate: an additional complication is the shift in the  $p_z$  direction due to the streaking field, which is different for scans measured at different delays. The NIR and the XUV polarizations were not exactly parallel. The polarization direction of the NIR pulse is given

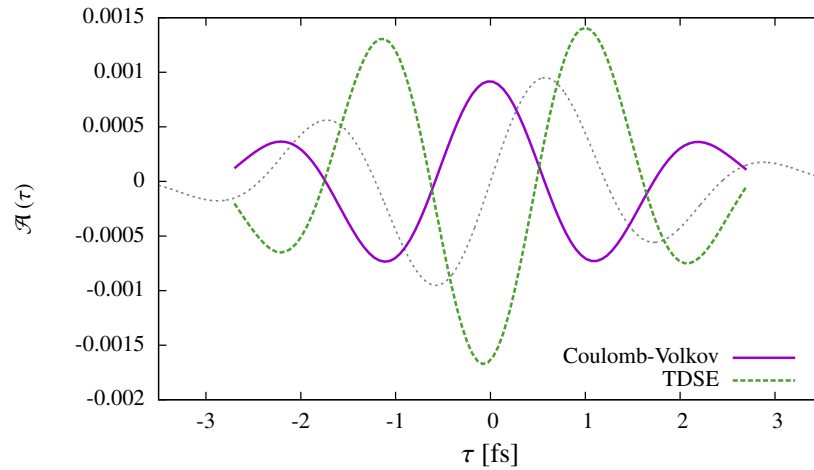


Figure 2.8: **Test of the Coulomb-Volkov approximation.** Asymmetry calculated at  $\theta = 0$ , as a function of the delay  $\tau$  between the XUV and the streaking pulse. The vector potential (in gray) is reported for reference, rescaled to fit into the picture. These results are obtained for a streaking field with intensity  $10^{11}$  W/cm<sup>2</sup>.

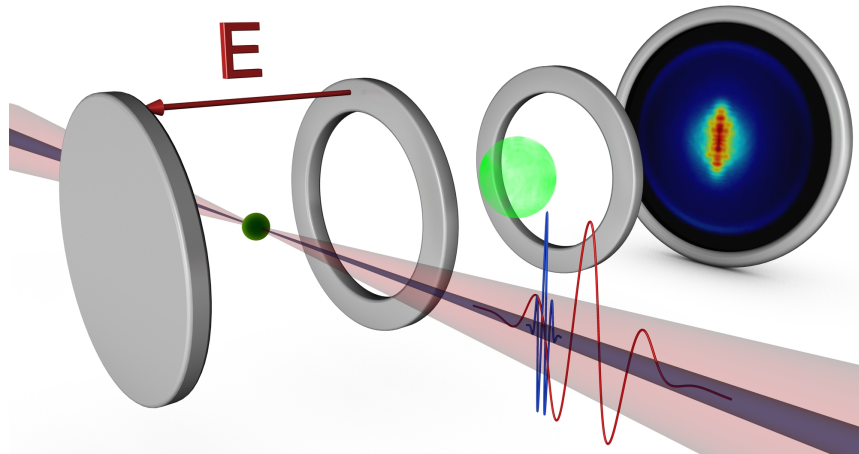


Figure 2.9: **Schematic of the attosecond VMI.** From [30]. Few-cycle NIR and XUV light fields have polarizations as indicated in the figure. The emitted electrons (green spheres) are focused by the electron optics onto an MCP-phosphor screen assembly, where an image of the projection of the electron momentum distribution is formed.



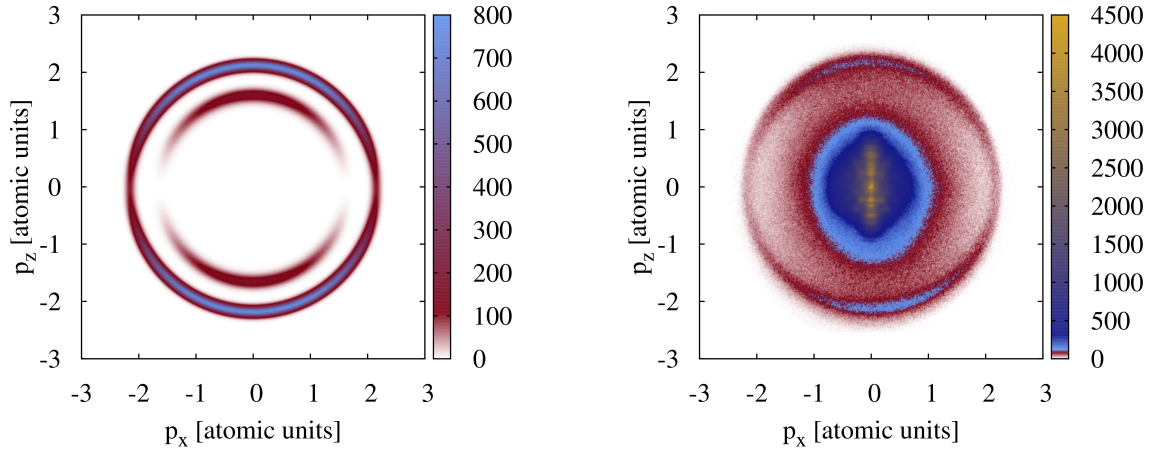


Figure 2.10: **Angular electron spectrum.** Electron distributions are peaked on the average kinetic energy, i.e. the XUV photon energy minus the binding energy  $\frac{p^2}{2} = \mathcal{E}_X - \mathcal{E}_b$ ; this is a circle in momentum space. Both for simulations and in the experiment an XUV pulse with central frequency 85 eV was used. **Left panel: Simulation.** The electron coming from the  $2s$  shell appears in the continuum with momentum  $p_{2s} = 1.6$ . As discussed in Sec. 2.1.1, it is a  $p$ -wave: its symmetry is clear in the simulation, it has zero probability to be measured at  $\theta = \pm\pi/2$ . The electron emitted from the  $2p$  shell has a momentum  $p_{2p} = 2.2$ . Its symmetry is less clear as it is the result of the interference of an  $s$ -wave and a  $d$ -wave. **Right panel: Raw experimental data.** ATI electrons completely cover the emission from the  $2s$  shell, but reveal us the polarization of the streaking field. We would expect to observe maxima of the  $2p$  emission at  $\theta = 0$  and  $\theta = \pi$  like in the simulation: the tilt may be due to an oblique polarization of the XUV pulse.

by the ATI distribution, and it coincides with the  $p_z$  axis of the detector. Electrons ejected in a single-photon interaction with the XUV pulse have a maximum in the direction of polarization of this field, because of the symmetry properties of the outgoing electron waves. Looking at the experimental data in Fig. 2.10 we draw the conclusion that probably the polarization of the XUV pulse was tilted by a few degrees. This might have introduced some artifact in the inverse Abel transform, since the symmetry axis of the electron distribution was not as expected. Another systematic error in the measurement arises from the non-uniform sensitivity of the detector; for our analysis we have established a procedure to compensate for it. We have used a cycle-averaged distribution of background electrons, which is supposed to be uniform. For each point  $(p_x, p_z)$  of this distribution we have considered the symmetric points  $(-p_x, p_z)$ ,  $(p_x, -p_z)$ ,  $(-p_x, -p_z)$  and we have defined the average of the distribution in these four points as the expected value if the detector were uniform. With the expected values we have built a “mask” to apply to data (see Fig. 2.11), in order to make them uniform. It is evident from the figure that the non-uniformity was substantial. Even though our procedure improves the uniformity of the data, we could apply it just after the Abel transform was performed. This implies that the non-uniformity of the detector might have spoiled the transform.

In spite of the possible flaws in the data we have evaluated the asymmetry from the measurement. Unfortunately it resulted to be two orders of magnitude larger than the evaluation of the TDSE and our calculations. The conclusion is that it is not possible yet to resolve in an experiment the small effects that we have highlighted from the simulations. The imperfections in

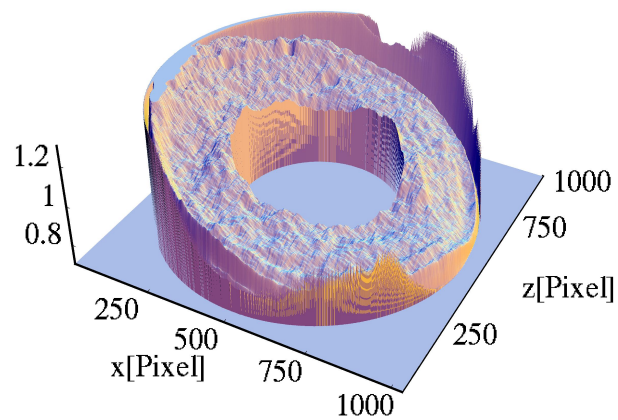


Figure 2.11: **“Mask” to account for the non-uniformity of the detector.** Using the measurement of a distribution which was supposed to be uniform, we have evaluated the non-uniformity of the detector and calculated a mask in order to adjust it. Each scan has to be multiplied by this mask: a value of 1 means that no correction is necessary.

the data that we have pointed out may have also played some role in hiding the details we were interested in.

# Chapter 3

## Overview of Field Interaction with Solids

The standard picture to describe the quantum state of an electron in a solid is the band model [48]. The potential of the ions is modeled as a regular 3D lattice. Every single well has a discrete energy spectrum  $\mathcal{E}_n$  and neighboring wells contribute to split the levels: in the limit of an infinite solid, levels are infinitely split and electrons can access continuous intervals of energy, called bands. A second quantum number  $\mathbf{k}$  labels the energy levels, determining the position of the electron in the band  $\mathcal{E}_n(\mathbf{k})$ . The quantum number  $\mathbf{k}$  is called “quasi-momentum”, but its relation with the momentum is not trivial and often misleading: it will be discussed in more detail in the following. Because of the exclusion principle, each state  $\mathcal{E}_n(\mathbf{k})$  can accommodate just two electrons with opposite spins: if an energy band has electrons occupying all the possible states (valence band), every perturbation occurring in that band will result just in an exchange of electron states, producing no net dynamic. The situation is different in a band where some states are free (conduction band): electrons in this band can access free states resulting in a non-zero average velocity, for example under the action of an external electric field.

While there are no doubts whether it is appropriate to use the band model for an isolated solid, questions have raised about the validity of this picture in the presence of an electric field. These questions are meaningful, because energy bands are defined for the unperturbed system, and in the presence of the electric field corresponding states are not eigenstates of the Hamiltonian anymore. An attempt to deal with this problem is to use Wannier-Stark states [49, 50], which are an approximation to eigenstates of the time-independent Hamiltonian. These different points of view will not take any part in the mathematical and numerical modelization of the system, but they will be the basis for different physical interpretation of the phenomena observed. Even though we understand the problem of defining proper “field-dressed states” like Wannier-Stark states, and we also investigate specifically this point (see Sec. 4.5), the physical picture underlying our interpretation will be expressed in terms of valence and conduction bands: the field distorts them but the concepts itself are still valid, and we find it more powerful in terms of heuristic advantages. At the same time, we have found the concept of localization of Wannier-Stark states somehow misleading in some situations.

The core of our investigation of electron dynamics in a solid will be the excitation of electrons from the valence to the conduction band of a dielectric. In this chapter we introduce concepts necessary for the subsequent analysis. Again, notions less relevant for the subsequent study will

not be treated completely, for a detailed coverage we refer the reader to [48, 51, 52].

### 3.1 Electrons in a Periodic Potential

In principle, the problem of an electron in a solid is a many-electron problem. However it is meaningful to consider the independent-particle approximation, where the interaction with other electrons is incorporated in an effective potential: we use this approximation here to introduce a fundamental theorem about the state of a particle in a periodic potential, and later to simplify numerical calculations. Let us consider an infinitely periodic potential  $U(\mathbf{r})$  with the structure of a Bravais lattice [48],

$$U(\mathbf{r} + \mathbf{R}) = U(\mathbf{r}), \quad (3.1)$$

for all Bravais lattice vectors  $\mathbf{R}$ , and the corresponding Hamiltonian

$$\hat{H} = -\frac{1}{2}\nabla^2 + U(\mathbf{r}). \quad (3.2)$$

According to the band model, energies of this Hamiltonian will be divided in continuous intervals  $\mathcal{E}_n(\mathbf{k})$  separated by forbidden regions; corresponding eigenstates are called ‘‘Bloch states’’

$$\hat{H} |\theta_{n\mathbf{k}}\rangle = \mathcal{E}_n(\mathbf{k}) |\theta_{n\mathbf{k}}\rangle. \quad (3.3)$$

**Bloch Theorem** The eigenstate  $|\theta_{n\mathbf{k}}\rangle$  of the one-electron Hamiltonian with periodic potential, can be chosen to have the form of a plane wave times a function with the same periodicity of the Bravais lattice:

$$\langle \mathbf{r} | \theta_{n\mathbf{k}} \rangle = e^{i\mathbf{k}\cdot\mathbf{r}} u_{n\mathbf{k}}(\mathbf{r}), \quad (3.4)$$

where  $u_{n\mathbf{k}}(\mathbf{r} + \mathbf{R}) = u_{n\mathbf{k}}(\mathbf{r})$  for all Bravais lattice vectors  $\mathbf{R}$ . In other terms

$$\theta_{n\mathbf{k}}(\mathbf{r} + \mathbf{R}) = e^{i\mathbf{k}\cdot\mathbf{R}} \theta_{n\mathbf{k}}(\mathbf{r}). \quad (3.5)$$

Writing the eigenvalue equation (3.3) for these states we obtain

$$\left[ \frac{1}{2}(-i\nabla + \mathbf{k})^2 + U(\mathbf{r}) \right] u_{n\mathbf{k}}(\mathbf{r}) = \hat{H}_{\mathbf{k}} u_{n\mathbf{k}}(\mathbf{r}) = \mathcal{E}_n(\mathbf{k}) u_{n\mathbf{k}}(\mathbf{r}). \quad (3.6)$$

The vector  $\mathbf{k}$  is not proportional to the electronic momentum. To show it we can calculate the average value of the momentum operator on a Bloch state:

$$\langle \theta_{n\mathbf{k}} | \hat{\mathbf{p}} | \theta_{n\mathbf{k}} \rangle = -i \int_{-\infty}^{+\infty} d^3\mathbf{r} e^{-i\mathbf{k}\cdot\mathbf{r}} u_{n\mathbf{k}}^*(\mathbf{r}) \nabla e^{i\mathbf{k}\cdot\mathbf{r}} u_{n\mathbf{k}}(\mathbf{r}) = \mathbf{k} + \int_{-\infty}^{+\infty} d^3\mathbf{r} u_{n\mathbf{k}}^*(\mathbf{r}) \nabla u_{n\mathbf{k}}(\mathbf{r}). \quad (3.7)$$

The quasi-momentum  $\mathbf{k}$  has indeed a dynamical significance close to the usual meaning of momentum: it will appear in the next section where we will study the interaction with an electric field. On the other hand, also the term in Eq. (3.7) has a relevant physical meaning. To prove

it, we evaluate the derivative  $\nabla_{\mathbf{k}}\mathcal{E}_n(\mathbf{k})$  following [48]. The derivative that we want to calculate appears in the expansion

$$\mathcal{E}_n(\mathbf{k} + \mathbf{q}) = \mathcal{E}_n(\mathbf{k}) + \nabla_{\mathbf{k}}\mathcal{E}_n(\mathbf{k}) \cdot \mathbf{q} + \dots ; \quad (3.8)$$

on the other hand, this is the eigenvalue of the Hamiltonian  $\hat{H}_{\mathbf{k}+\mathbf{q}}$  (see Eq. (3.6)). We can calculate the required term from the fact that

$$\hat{H}_{\mathbf{k}+\mathbf{q}} = \hat{H}_{\mathbf{k}} + \mathbf{q} \cdot (-i\nabla + \mathbf{k}) + \frac{q^2}{2}, \quad (3.9)$$

applying perturbation theory. Given a Hamiltonian  $\hat{H} = \hat{H}_0 + \hat{V}$ , perturbation theory provides us with an expansion for the eigenvalues of  $\hat{H}$  in terms of the eigenvalues of  $\hat{H}_0$ . Let us call  $\mathcal{E}_n^0$  these eigenvalues,

$$\hat{H}_0 |\theta_n\rangle = \mathcal{E}_n^0 |\theta_n\rangle ; \quad (3.10)$$

then to the first order in the perturbation  $\hat{V}$ , the corresponding eigenvalues of  $\hat{H}$  are

$$\mathcal{E}_n = \mathcal{E}_n^0 + \int_{-\infty}^{+\infty} d^3\mathbf{r} \theta_n^*(\mathbf{r}) V \theta_n(\mathbf{r}) + \dots . \quad (3.11)$$

Since we are looking for the coefficient of the linear term in  $q$  in the expansion (3.8), we can keep just the linear term in Eq. (3.9) and substitute it into (3.11). In this way, we find that

$$\nabla_{\mathbf{k}}\mathcal{E}_n(\mathbf{k}) = \langle \theta_{n\mathbf{k}} | \hat{\mathbf{p}} | \theta_{n\mathbf{k}} \rangle . \quad (3.12)$$

This equation indeed looks like the dispersion relation for a wavepacket: its physical interpretation will be discussed in the next paragraph.

## 3.2 Semiclassical Picture

Our investigation of electron dynamics in dielectrics during the interaction with a strong field will be based on a numerical solution of the TDSE. We present here a well known attempt to model these dynamics in a simplified way, which goes under the name of “semiclassical approach”. The predictive possibilities of this model are very limited, and it is not suitable to describe strong field dynamics; however it is a very useful starting point to understand some peculiarities of the electron motion in a lattice.

Let us consider an electron wavepacket in a lattice potential. We will consider this wavepacket as having a determined quasi-momentum, therefore we want the spread  $\Delta k$  to be small: this in turns translates into a big width in coordinate space, i.e. a wavepacket as large as many primitive cells. At the same time, we also require the electric field to vary slowly over the dimensions of the wavepacket, in order to consider it uniform at each moment. In this section we will consider just interactions with NIR fields: their wavelength ( $\sim 700$  nm) is orders of magnitude larger than a common lattice spacing ( $\sim 1$  nm), and we can assume it to be very large also with respect to a wavepacket spread over many primitive cells. We will formulate an ansatz to describe how the

position  $\mathbf{r}$  and quasi-momentum  $\mathbf{k}$  of the wavepacket evolve in the presence of an electric field, neglecting electron scattering on the lattice. The equations of motion will depend entirely on the band structure  $\mathcal{E}_n(\mathbf{k})$ : we will directly relate it to transport properties. If  $\mathbf{k}$  were the actual canonical momentum of the electron – or equivalently the wave vector of the wavepacket – the band structure would provide the dispersion relation for the wavepacket. In this hypothetical case, the group velocity would be

$$\frac{d}{dt}\mathbf{r} = \mathbf{v}_n(\mathbf{k}) = \nabla_{\mathbf{k}}\mathcal{E}_n(\mathbf{k}) . \quad (3.13)$$

In fact, we have proved in Eq. (3.12) that for an electron in a Bloch state  $\theta_{n\mathbf{k}}(\mathbf{r})$ ,

$$\nabla_{\mathbf{k}}\mathcal{E}_n(\mathbf{k}) = -\frac{i}{m} \int d^3\mathbf{r} \theta_{n\mathbf{k}}^*(\mathbf{r}) \nabla_{\mathbf{r}} \theta_{n\mathbf{k}}(\mathbf{r}); \quad (3.14)$$

the integral on the right can be read as the average of the velocity operator  $\hat{\mathbf{p}}/m$ , which turns out to be equal to our guess (3.13). We will also assume that the quasi-momentum  $\mathbf{k}$  evolves as if it were the actual momentum of a free, classical electron in the electric field:

$$\frac{d}{dt}\mathbf{k} = -[\mathbf{E}(t) + \mathbf{v}(\mathbf{k}) \times \mathbf{H}(t)] , \quad (3.15)$$

where  $\mathbf{H}$  is the magnetic field, which we will neglect with respect to the electric field. Equations (3.13) and (3.15) are the *semiclassical equations of motions* for an electron in a periodic lattice: they are called semiclassical because the effect of the lattice potential is considered quantum mechanically through the band structure, but the interaction with the field is classical. The role of the quasi-momentum is more clear in this picture: it resemble the momentum of a free electron and evolves accordingly, while the dispersion relation takes into account the band structure. Semiclassical equations assign a velocity to each electron, depending just on the state it occupies in energy bands. However, they confirm that electrons in a completely filled band do not contribute to the current: since the total current is obtained from the contribution of all  $\mathbf{k}$ s occupied, in a full band contributions from different state will cancel each other giving zero net current.

From the semiclassical equations we can derive an equation of motion for the electron in the band structure. Its “acceleration” would be

$$\frac{d^2}{dt^2}\mathbf{r} = \frac{d}{dt}\mathbf{v}(\mathbf{k}) = \nabla_{\mathbf{k}}\mathbf{v}(\mathbf{k}) \cdot \frac{d}{dt}\mathbf{k} = \sum_{u,w} \hat{e}_u \frac{\partial^2 \mathcal{E}_n(\mathbf{k})}{\partial k_u \partial k_w} \frac{d}{dt}k_w = \sum_{u,w} \hat{e}_u (m^*)_{uw}^{-1} F_w , \quad (3.16)$$

where  $\hat{e}_u$  is the unit vector in cartesian direction  $u$ .  $F_w$  is the  $w$  component of the “force” acting on the quasi-momentum in Eq. (3.15). The equation that we have obtained resemble a Newton equation with a mass tensor

$$(m^*)_{uw}^{-1} = \frac{\partial^2 \mathcal{E}(\mathbf{k})}{\partial k_u \partial k_w} \quad (3.17)$$

which is a property of the band structure only. This quantity in principle depends on  $\mathbf{k}$  except for parabolic bands (i.e. free electrons) where it is constant: however it is a common practice to make estimations including the effects of the band structure just through a constant effective mass, evaluated at the center of the Brillouin zone.

### 3.3 Interband Transitions

In the semiclassical picture, the excitation of electrons between two bands was not taken into account: its aim is to describe the motion of charge carriers already present in a band. The model is suitable if we are not interested in the creation of charge carriers, or in interband excitation. Metals always have electron in the conduction band, independently on background conditions; semiconductors usually have charge carriers at room temperature because of thermal excitation. Interband transitions can occur in these materials but they will not drastically change properties of the medium. The band gap in semiconductors is on the order of  $\sim 1$  eV: visible light is therefore absorbed by single-photon transitions.

The topic of the next chapter will be a detailed investigation of interband excitation in dielectrics. This class of materials are insulators and do not have charge carriers: they can be created if an electron from the valence band overcomes the band gap, acquiring the possibility to be accelerated in the conduction band and leaving a hole behind. Such an excitation will modify all the optical and electrical properties of the medium. Since the band gap of insulators is as large as many eV (9 eV for silicon dioxide, reference for our investigation) the excitation process is usually referred to as “interband tunneling”: as argued in the pioneer paper of Zener [53], in a constant electric field energy levels and energy gaps depend on spatial coordinate, so that an electron may tunnel from a band into another, which would lie at higher energies if the field were absent. In the same paper the (cycle-averaged) tunneling rate  $w$  is calculated in terms of the band-gap  $\Delta$  and the field  $E$ . The calculation is based upon a semiclassical approach, where energies in the gap region are assigned to a complex quasi-momentum. The excitation rate have been subsequently calculate by Keldysh [54] and Kane [55]. Different approaches obtain different results, but we are not interested in a detailed study of the electron rate, and we will rather highlight common characteristics. The form obtained is similar for all the derivations

$$w \propto \frac{E^\alpha}{\Delta^\beta} \exp\left(-C \frac{\Delta^\delta}{|E|}\right), \quad (3.18)$$

where  $\alpha, \beta$  and  $\delta$  are positive rational numbers and  $C$  is a constant which contains the effective mass of the electron. The electric field  $E$  does not depend time, because results are obtained for constant or cycle-averaged field.

### 3.4 Current and Polarization

In the classical case, the current density is defined as the density of charge carriers  $\rho = N/V$  multiplied by their average velocity, and the polarization as the average dipole moment  $\mathbf{d}$  per unit volume; assuming negative charge

$$\mathbf{J} = -\rho \mathbf{v} \quad \text{and} \quad \mathbf{P} = \frac{\langle \mathbf{d} \rangle}{V}. \quad (3.19)$$

We can write the dipole moment in terms of the displacement  $\mathbf{s}$

$$\mathbf{P} = \frac{\langle \mathbf{d} \rangle}{V} = -\frac{N}{V} \mathbf{s} = -\rho_b \mathbf{s}, \quad (3.20)$$

where the subscript  $b$  underlines that these charges are bound. It is clear that a non-constant polarization corresponds to a movement of charge, and therefore to a current

$$\frac{d}{dt}\mathbf{P} = -\rho_b \frac{d}{dt}\mathbf{s} = -\rho_b \mathbf{v} = \mathbf{J}_b . \quad (3.21)$$

In this framework it is easy to tell apart the current due to free charges  $\mathbf{J}_f$  and to bound charges; the total current is

$$\mathbf{J} = \mathbf{J}_f + \frac{d}{dt}\mathbf{P} + \nabla \times \mathbf{M} , \quad (3.22)$$

where for completeness we have included the magnetization current as last term.

In the quantum picture there is no clear distinction between free and bound charges. Indeed electrons in valence bands resemble bound electrons – as they do not really conduct current but can be displaced from their equilibrium positions – and electrons in conduction bands behave more like free carriers; however, our goal is to study interband excitation, where these concepts become blurry. If the valence band is depleted, qualitative response to the field of conduction band electrons is indistinguishable from that of valence band electrons, even if they have a lower mobility; in addition to that, we will be dealing with a wavefunction representing an electron in a superposition of states in different bands. To clarify the matter we analyze here the quantum expressions for the current and the polarization and find the relation between them; for simplicity we will restrict ourselves to one spatial dimension, expecting qualitative similar results in the 3D case. We define the average polarization as the displacement of the center of mass of the wavefunction in the single cell, multiplied by the charge:

$$\langle P \rangle = -\frac{1}{a} \int_{-\frac{a}{2}}^{\frac{a}{2}} dx x |\psi(x)|^2 , \quad (3.23)$$

where  $a$  is the lattice spacing. Let us consider the time derivative of this quantity

$$\frac{d}{dt} \langle P \rangle = \frac{i}{a} \int_{-\frac{a}{2}}^{\frac{a}{2}} dx x \psi^*(x) \hat{H} \psi(x) + c.c. , \quad (3.24)$$

where we have substituted the TDSE for the time derivative of the wavefunction. We consider the velocity gauge Hamiltonian Eq. (1.15), and notice that any potential  $U(x)$  would cancel out with its complex conjugate:

$$\frac{d}{dt} \langle P \rangle = \frac{A}{a} \int_{-\frac{a}{2}}^{\frac{a}{2}} dx x \psi^*(x) \frac{\partial}{\partial x} \psi(x) - \frac{i}{2a} \int_{-\frac{a}{2}}^{\frac{a}{2}} dx x \psi^*(x) \frac{\partial^2}{\partial x^2} \psi(x) + c.c. . \quad (3.25)$$

Let us treat the two terms separately. The first term is easily integrated by parts

$$\begin{aligned} & \frac{A}{a} \int_{-\frac{a}{2}}^{\frac{a}{2}} dx x \psi^*(x) \frac{\partial}{\partial x} \psi(x) + c.c. = \\ & \frac{A}{a} \left[ x |\psi(x)|^2 \Big|_{-\frac{a}{2}}^{\frac{a}{2}} - \int_{-\frac{a}{2}}^{\frac{a}{2}} dx |\psi(x)|^2 - \int_{-\frac{a}{2}}^{\frac{a}{2}} dx x \frac{\partial}{\partial x} \psi^*(x) \psi(x) \right] + c.c. = \\ & A \left| \psi \left( \frac{a}{2} \right) \right|^2 - \frac{A}{a} , \end{aligned} \quad (3.26)$$



where we have recognized the last term of the integration by parts as the complex conjugate of the whole element. We proceed in a similar way for the second term

$$\begin{aligned}
& -\frac{i}{2a} \int_{-\frac{a}{2}}^{\frac{a}{2}} dx x \psi^*(x) \frac{\partial^2}{\partial x^2} \psi(x) + c.c. = \\
& -\frac{i}{2a} \left[ x \psi^*(x) \frac{\partial}{\partial x} \psi(x) \Big|_{-\frac{a}{2}}^{\frac{a}{2}} - \int_{-\frac{a}{2}}^{\frac{a}{2}} dx \psi^*(x) \frac{\partial}{\partial x} \psi(x) - \int_{-\frac{a}{2}}^{\frac{a}{2}} dx x \frac{\partial}{\partial x} \psi^*(x) \frac{\partial}{\partial x} \psi(x) \right] + c.c. = \\
& \text{Im} \left[ \psi^* \left( \frac{a}{2} \right) \frac{\partial \psi}{\partial x} \left( \frac{a}{2} \right) \right] - \frac{1}{a} \int_{-\frac{a}{2}}^{\frac{a}{2}} dx \text{Im} \left[ \psi^*(x) \frac{\partial}{\partial x} \psi(x) \right] = \langle J \rangle - J \left( \frac{a}{2} \right), \tag{3.27}
\end{aligned}$$

where the last term of the integration by part is purely imaginary and cancels out with its complex conjugate. We have used the equality  $-iw + c.c. = 2 \text{Im}[w]$ . The current is considered for a negative charge as in Eq. (1.20) and its average in the primitive cell is defined in the usual way. Assembling the two terms we finally obtain

$$\frac{d}{dt} \langle P \rangle = \langle J \rangle - J \left( \frac{a}{2} \right) + A \left| \psi \left( \frac{a}{2} \right) \right|^2 - \frac{A}{a}, \tag{3.28}$$

or in terms of the velocity gauge current Eq. (1.23)

$$\langle J_V \rangle = \frac{d}{dt} \langle P \rangle + J_V \left( \frac{a}{2} \right). \tag{3.29}$$

We can draw a parallel between this relation and Eq. (3.22). We can interpret the border term  $J_V \left( \frac{a}{2} \right)$  as the actual charge traveling outside the primitive cell, and therefore through the whole solid: in this regard it plays the role of free charge, while the derivative of the polarization is the contribution from the bound charge.

## 3.5 Classical Light-Matter Interaction

The interaction of an electric field with a medium can be dealt with in several ways, according to the assumptions that we do on the sample (linearity, homogeneity, dispersive/absorbing) and the degree of complexity (ray optics, electromagnetic optics, quantum optics). We introduce here some notions of classical, electromagnetic optics about the response of a material to an electric field [51, 52]: they will be the basis for the subsequent analysis.

### 3.5.1 Nonlinear, Noninstantaneous Response

Nonlinear optical phenomena occur if the incident field is intense enough to modify the optical properties of the material. The typical response function is the polarization  $P(t)$ : the response to the incident field  $E(t)$  is linear and instantaneous if

$$P(t) = P_L(t) = \epsilon_0 \chi_1 E(t), \tag{3.30}$$

where the constant of proportionality  $\chi_1$  is the linear susceptibility. The relative permittivity  $\epsilon_r$  of a linear, homogeneous, isotropic dielectric is defined through Eq. (3.30), by writing the electric displacement field as

$$D = \epsilon_0 E + P = \epsilon_0(1 + \chi_1) E = \epsilon_0 \epsilon_r E, \quad (3.31)$$

where  $\epsilon_r = 1 + \chi_1$ . The electric field in the medium obeys the wave equation with velocity  $v = (\epsilon_0 \epsilon_r \mu_0)^{-1/2}$ ; since the speed of light in vacuum is  $c = (\epsilon_0 \mu_0)^{-1/2}$  we can express the velocity in the medium as

$$v = \frac{c}{\sqrt{\epsilon_r}} = \frac{c}{n}, \quad (3.32)$$

where  $n = \sqrt{\epsilon_r} = \sqrt{1 + \chi_1}$  is the refractive index.

If the response is nonlinear, Eq. (3.30) has to be generalized as a power series in the field strength

$$P(t) = \epsilon_0 \chi_1 E(t) + \epsilon_0 \chi_2 E^2(t) + \epsilon_0 \chi_3 E^3(t) + \dots \quad (3.33)$$

The quantities  $\chi_2$  and  $\chi_3$  are the second- and third-order nonlinear susceptibilities. We have taken  $P(t)$  and  $E(t)$  as scalar quantities; in general they are vectors and  $\chi_1$  is a second-rank tensor,  $\chi_2$  is a third-rank tensor, and so on.

The response of the system always occurs after a certain delay; if this delay is extremely short in comparison with other times of interest, we can assume that the response is instantaneous and, via the Kramers-Kronig relation, that the material is lossless and dispersionless. In general we have to take into account the time elapsing between the signal and the response: the response at a time  $t$  will be affected by the signal  $E(\tau)$  at  $\tau \leq t$ . In the linear case the response function is readily evaluated as a sum over all the past effects of the signal:

$$P_L(t) = \epsilon_0 \int_{-\infty}^t d\tau \chi_1(t - \tau) E(\tau) = \epsilon_0 \int_{-\infty}^{+\infty} d\tau \chi_1(\tau) E(t - \tau). \quad (3.34)$$

In the first integral causality is ensured by the integration limit  $t$ , and in the second integral by the assumption that  $\chi_1(t) = 0$  for  $t < 0$ : this condition expresses the fact that  $P(t)$  depends only on past and not on future values of  $E(t)$ . Introducing Fourier transforms of the polarization  $P(\omega)$ , the susceptibility  $\chi_1(\omega)$  and the field  $E(\omega)$  we take advantage of the convolution theorem and rewrite Eq. (3.34) as

$$P(\omega) = \epsilon_0 \chi_1(\omega) E(\omega). \quad (3.35)$$

In a similar manner it is possible to introduce non-instantaneous, nonlinear polarization response. For example the second order contribution to the polarization can be represented as

$$P_2(t) = \epsilon_0 \int_0^{+\infty} d\tau_1 \int_0^{+\infty} d\tau_2 \chi_2(\tau_1, \tau_2) E(t - \tau_1) E(t - \tau_2), \quad (3.36)$$

where the causality condition requires that  $\chi_2(\tau_1, \tau_2) = 0$  if either  $\tau_1$  or  $\tau_2$  is negative.

Eq. (3.35) shows that in case of non-instantaneous response, the susceptibility depends on the frequency: this implies that the medium is dispersive. The non-instantaneous expression of the

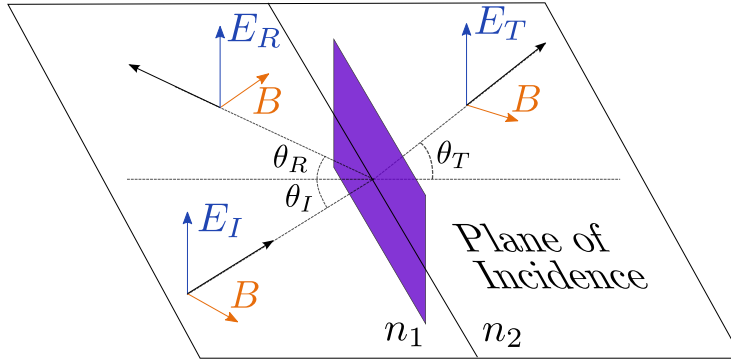


Figure 3.1: **Reflection and Transmission.** Geometrical outline of the reflection and transmission at the boundary of two media with different refractive index.

susceptibility also shows that in general it is a complex quantity, obeying the Kramers-Kronig relations:

$$\operatorname{Re} [\chi_1(\omega)] = \frac{1}{\pi} \int_{-\infty}^{\infty} d\omega' \frac{\operatorname{Im} [\chi_1(\omega')]}{\omega' - \omega}, \quad (3.37)$$

$$\operatorname{Im} [\chi_1(\omega)] = -\frac{1}{\pi} \int_{-\infty}^{\infty} d\omega' \frac{\operatorname{Re} [\chi_1(\omega')]}{\omega' - \omega}. \quad (3.38)$$

Since the refractive index is defined in terms of the susceptibility, in this case it is also frequency-dependent and complex valued. The dispersion relation between the wave vector  $k$  and the frequency  $\omega$  happens to be  $k(\omega) = \frac{\omega}{c} (n(\omega) + i\kappa(\omega))$ . A plane wave traveling in the medium is described by a complex amplitude proportional to  $e^{ikz}$ : since  $k$  is complex both magnitude and phase of the wave vary with  $z$ . The amplitude of the wave scales as  $|e^{ikz}|^2 = e^{-2\frac{\omega}{c}\kappa z}$  so that  $\kappa(\omega)$  represents the absorption coefficient.

### 3.5.2 Reflection and Transmission

Let us now examine the reflection and transmission of an incident pulse, traveling from a medium with refractive index  $n_1$  to a medium with refractive index  $n_2$ . The media are assumed to be linear, homogeneous, isotropic, nondispersive, and nonmagnetic. We consider the case of electromagnetic radiation polarized normal to the plane of incidence (called s-polarized, or transverse electric), see Fig. 3.1. The angle of reflection is equal to the angle of incidence  $\theta_R = \theta_I$ ; the angle of transmission satisfies Snell's law

$$n_1 \sin \theta_I = n_2 \sin \theta_T. \quad (3.39)$$

In order to relate electric field strengths of different beams we use the joint conditions at the boundary of a medium. The electric field is perpendicular to the plane of incidence, and therefore parallel to the interface:

$$E_I + E_R = E_T, \quad (3.40)$$

because the parallel component is conserved. The incident magnetic field forms an angle  $\theta_I$  with the interface and the transmitted magnetic field an angle  $\theta_T$ :

$$(B_I - B_R) \cos \theta_I = B_T \cos \theta_T , \quad (3.41)$$

because we are considering nonmagnetic materials. The relation between magnetic and electric field amplitude is  $B = \frac{n}{c} E$ , thus in terms of the electric field we have

$$n_1 (E_I - E_R) \cos \theta_I = n_2 E_T \cos \theta_T . \quad (3.42)$$

Substituting Eq. (3.40) into Eq. (3.42), once for  $E_R$  and once for  $E_T$  we obtain Fresnel equations

$$\frac{E_R}{E_I} = \frac{n_1 \cos \theta_I - n_2 \cos \theta_T}{n_1 \cos \theta_I + n_2 \cos \theta_T} \quad (3.43)$$

$$\frac{E_T}{E_I} = \frac{2n_1 \cos \theta_I}{n_1 \cos \theta_I + n_2 \cos \theta_T} . \quad (3.44)$$

We will often consider normal incidence ( $\theta_I = \theta_R = 0$ ) at the boundary air-dielectric ( $n_1 \approx 1$ ); in this particular case, Fresnel equations reduce to

$$\frac{E_R}{E_I} = \frac{1 - n_2}{1 + n_2} \quad (3.45)$$

$$\frac{E_T}{E_I} = \frac{2}{1 + n_2} . \quad (3.46)$$

# Chapter 4

## Interaction of a Dielectric with a Strong Field

Light-matter interaction is one of the main branches of modern physics, comprehending a huge number of phenomena and physical processes. The possibility of systematically investigating the nature of matter with a coherent source is the basis of our current understanding of solid systems, and it has paved the way to a large fraction of the technological innovations which shaped the last century. Properties of (doped) semiconductor devices triggered the information technology revolution. Dielectrics, with their large band gap offer a less interesting response to electric fields: polarization with extremely low conductivity at low fields and breakdown at high fields. However, recent innovations in the generation of ultrashort, very strong laser pulses, is opening the way to a brand new field of research on these materials, enabling valence band electrons to overcome the band gap without the breakdown of the sample. Recent experiments [56, 57] show the feasibility of this operation and propose for the first time the use of dielectrics for electronic signal processing. All these new opportunities demand a sound theoretical foundation. Interband electron excitation and the tunneling process in solids have indeed already been studied, and theories were established to describe them (see Sec.3.3), but these regimes were not accessible by experiments, and a detailed analysis is now required. Moreover, a deeper theoretical understanding may lead to a better control of electronic dynamics and the conception of novel techniques.

The goal of this chapter is to theoretically investigate the physical processes happening in a dielectric when it interacts with a strong electric field. To a big extent, dielectrics are characterized by their band gap: in the following we will consider a band gap of approximately 9 eV, close to that of silicon dioxide ( $\text{SiO}_2$ ). Even though we will not take advantage of any atomic structure calculation, parameters of our model system will be chosen as close as possible to those of  $\text{SiO}_2$ : not only the band gap, but also the band structure and the dielectric response will be adjusted to mimic the response of this material. “Strong field” is intended in comparison to the band gap: in other words we will consider intensities comparable with those necessary to excite electrons through the band gap, from valence to conduction bands. Such intensities, ranging from  $0.001 \text{ PW/cm}^2$  to a fraction of  $1 \text{ PW/cm}^2$ , are very close to the breakdown threshold of the sample: in order to realistically carry on an experiment with these intensities, the laser pulse

must be extremely short. We will consider few-cycle near-infrared (NIR) pulses, as short as few femtosecond, with the intensities mentioned above.

The main tool of our theoretical study is a numerical solver of the TDSE for a single particle in a lattice potential, which we will use to simulate electron dynamics in bulk solid: it will be described in detail in the next section. We will use it in the first place (Sec. 4.2) to calculate the current induced in the dielectric when the field is so strong that the sample starts conducting, and to analyze how the total charge transferred during the process depends on laser parameters. This is one of the first matters which were approached experimentally.

In a context of more fundamental questions we will wonder whether a signature of the interband transition is left in the electromagnetic radiation emitted by the dielectric (Sec. 4.3) and whether it appears in the reflected pulse (Sec. 4.4). This would allow an experimental detailed study of the tunneling excitation in solids.

Finally, from a purely mathematical point of view, we will approach the riddle of finding an approximate definition for eigenstates of the Hamiltonian, when it explicitly depends on time through the electric field (Sec. 4.5). A similar definition would have often come handy, and sometimes crucial, during our research.

## 4.1 Numerical Solver of the Time Dependent Schrödinger Equation in a 1D Lattice

There are many ways to approach the numerical simulation of electron dynamics in a solid ([58, 59]) under the effect of an electric field. We tackle this problem with some approximations, to reduce the complexity of the numerical solution of the TDSE.

- We consider single-particle dynamics, neglecting collective effects: this means that the particle will feel the external electric field, but the field created of by the other electrons will be included in the pseudo-potential, and therefore will not depend on the incident pulse. This is not a big trouble as long as we want to investigate the interaction with a certain field, without wondering how the field in the material is related to the incident laser pulse; alternatively we can assume a linear relation (Fresnel formula Eq. (3.45)) to describe the screening effect of other electrons. However in Sec. 4.4 where we focus explicitly on the relation between the incident and the transmitted field, we find a way to work around this problem.
- The calculation is restricted to one dimension: this reduces a lot the computational demand and the complication of the problem. At the same time it is a crude approximation, which becomes more severe if dynamics in different directions are strongly coupled. We do not expect this to happen in the examined cases, where the field will be linearly polarized in the direction of the lattice; nevertheless our model has few chances to reach a quantitative agreement with observations. The calculation of three dimensional quantities from the 1D result follows from the assumption that dynamics in different directions are decoupled: if it were the case the 3D result would be proportional to the 1D. We adjust the proportionality

parameter in such a way that the linear response of the system to a low field corresponds to the one of silicon dioxide.

- We model the ion lattice as a perfectly periodic, “frozen” potential: therefore our description will not include phonon dynamics or scattering. This is one of the major drawbacks of our tool, as scattering rate is supposed to be  $\sim 0.5 \text{ fs}^{-1}$  [60], comparable with the frequency of the laser field. In addition to that, electron dynamics are supposed to quickly fade away after the laser pulse is gone, due to relaxation effects (dephasing, scattering). We can include similar processes phenomenologically, but in most of our simulations electronic dynamics will just live indefinitely.

Even restricting the problem to a single particle moving in a periodic potential, we still have freedom in the choice of the gauge, the boundary conditions, and the calculation of the band structure and dipole matrix elements. We have implemented our tool following [61], we recall here the main characteristics of the approach.

**The Lattice Potential and the Band Structure** The potential is modeled as a single well  $U_c(x)$  with periodic boundary conditions

$$U(x) = \sum_j U_c(x + ja), \quad (4.1)$$

where  $a$  is the period of the lattice, and the first unit cell extends from  $-a/2$  to  $a/2$ ; we have used  $a = 0.5 \text{ nm}$ , close to dimension of the unit cell of  $\text{SiO}_2$  [62]. The single well potential  $U_c(x)$  is symmetric in the unit cell and goes to zero at the boundaries,  $U(-a/2) = U(a/2) = 0$ . Eq. (4.1) is the best approximation to an infinite solid: our calculation will not depend on a particular choice of the potential at the edge of the bulk, and the Hamiltonian will be exactly periodic. On the other hand, some attention is required when handling quantities calculated with periodic boundary conditions: for example the wave function is not normalizable in the whole space and is conventionally normalized on one period length  $a$ . This implies that fundamental theorems of quantum mechanics have to be taken with a grain of salt, checking whether they actually apply and under which conditions. A common choice different from Eq. (4.1) is to use a potential with  $N$  wells and infinite walls at the boundary (or absorbing boundary condition). We did not follow this approach but we will use it to check our result.

The field-free Hamiltonian of the single electron is

$$\hat{H}_0 = -\frac{1}{2} \frac{\partial^2}{\partial x^2} + U(x); \quad (4.2)$$

we diagonalize it in order to obtain energy bands  $\mathcal{E}_n(k)$  of the chosen potential

$$\hat{H}_0 \theta_n(x, k) = \mathcal{E}_n(k) \theta_n(x, k), \quad (4.3)$$

where  $\theta_n(x, k)$  are Bloch states. The diagonalization is carried out numerically and it is natural to perform it in Fourier space, where the momentum operator is diagonal. Since the potential is

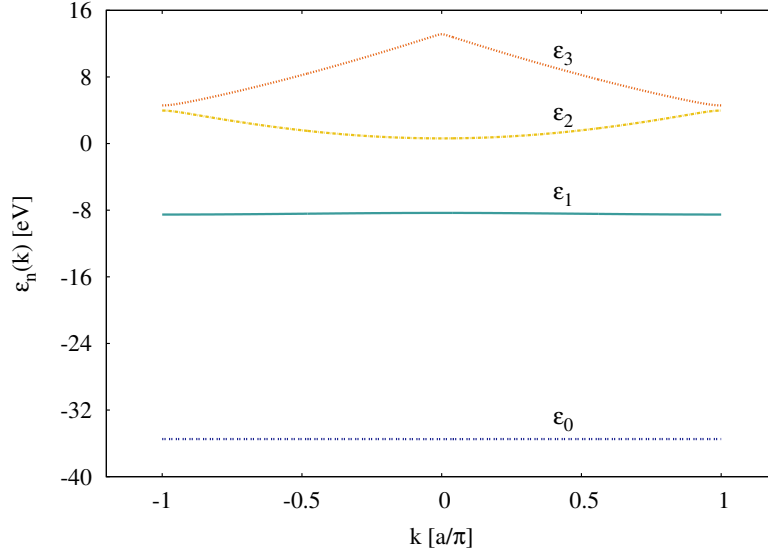


Figure 4.1: **Band Structure.** Two valence bands and two conduction bands are shown, in the first Brillouin zone. The first conduction band has positive energies, electrons occupying these states will have a behavior similar to free charges.

periodic, it admits a discrete Fourier decomposition

$$U(x) = \sum_{j=0}^{N_{\max}} U_j e^{iG_j x}, \quad (4.4)$$

where  $G_j = (j - \frac{N_{\max}}{2}) \frac{2\pi}{a}$  are the reciprocal lattice vectors and  $N_{\max} + 1$  is the number of plane waves used in the basis. Fourier components of the potential are

$$U_j = \frac{1}{a} \int_{-\frac{a}{2}}^{\frac{a}{2}} e^{-iG_j x} U_c(x) dx, \quad (4.5)$$

and given the symmetry of the potential,  $G_j$  and  $-G_j$  will give the same  $U_j$ . Considering the properties of the eigenstates of a periodic potential (see Bloch states Eq. (3.4)) they have the following Fourier decomposition

$$\theta_n(x, k) = e^{ikx} \sum_{j=0}^{N_{\max}} C_{j,n}(k) e^{iG_j x}. \quad (4.6)$$

For each  $k$ , the Hamiltonian  $H_0$  is represented in Fourier space by a matrix  $(N_{\max} + 1) \times (N_{\max} + 1)$  containing Fourier components of the potential, and kinetic energy terms  $(G_j + k)^2/2$  on the diagonal; the diagonalization of this matrix provides us with energy levels  $\mathcal{E}_n(k)$  as eigenvalues and Bloch states coefficients  $C_{j,n}$  as eigenvectors. We normalize Bloch states in such a way that

$$\int_{-\frac{a}{2}}^{\frac{a}{2}} |\theta_n(x, k)|^2 dx = 1, \text{ or in other terms } \sum_j |C_{n,j}|^2 = \frac{1}{a}. \quad (4.7)$$



In our simulations we have used  $N_{\max} = 50$ : this number of plane waves is more than necessary for convergence, but since it comes into play just for the diagonalization of the Hamiltonian its cost in terms of computational time is negligible. For the diagonalization of the Hamiltonian (which is a large complex matrix) we have used an algorithm contained in LAPACK libraries.

The potential  $U_c(x)$  is adjusted to reproduce the band gap of  $\text{SiO}_2$ . We regard bands  $n = 0$  and  $n = 1$  as valence bands and  $n \geq 2$  as conduction bands: the band gap is  $\sim 8.9$  eV, and the effective mass of the electron in the first conduction band (in the center of the first Brillouin zone, where the band is approximately parabolic) is  $m^* = [\mathcal{E}''(k = 0)]^{-1} \approx 0.36$ . These values are very close to those of  $\text{SiO}_2$ , which has the same band gap and similar effective mass; the value of the effective mass is estimated between 0.3 and 0.5 [63, 64, 65], depending on the crystalline structure. Valence bands and the first two conduction bands are shown in Fig. 4.1. The comparison of our dipole matrix elements with those obtained with Density Functional Theory suggests that we overestimate them, in spite of the correct band-gap. Together with the lack of scattering effects, this probably leads to an overestimation of excitation probabilities and strong-field-induced electric current in our simulations.

**The Gauge Choice** Incorporating the interaction with the electric field into the Hamiltonian, we have the freedom to choose between the length and the velocity gauge (see Sec. 1.3). Even though the two choices must produce exactly the same values for physical observables, the length gauge provides a more intuitive picture of physical phenomena, being related to the frame of reference of the laboratory; dynamics in the velocity gauge are less immediate to interpret, as the reference system moves according to the vector potential  $A(t)$ . Nonetheless, for our purposes it is better to use velocity gauge. The reason is that the interaction operator in the length gauge  $\hat{x}$  couples Bloch states with different  $k$ , while the interaction operator in the velocity gauge  $\hat{p}$  is diagonal on  $k$ . This can easily be seen calculating the momentum matrix element between two Bloch states, assuming that our solid is made of  $N$  cells:

$$\begin{aligned} \langle \theta_m(k) | \hat{p} | \theta_n(q) \rangle &= \frac{1}{N} \int_{-N\frac{a}{2}}^{N\frac{a}{2}} \theta_m(x, k)^* \left( -i \frac{\partial}{\partial x} \right) \theta_n(x, q) dx = \\ &= \frac{1}{N} \sum_{j,l} C_{l,m}(k)^* C_{j,n}(q) (q + G_j) \int_{-N\frac{a}{2}}^{N\frac{a}{2}} e^{i(q-k)x} e^{i(j-l)\frac{2\pi}{a}x} dx, \end{aligned}$$

where we have substituted the Fourier expansion of Bloch states from Eq. (4.6). We consider the limit of an infinite solid,  $N \rightarrow \infty$  and the integral above is non-zero just if  $(k - q) = \nu \frac{2\pi}{a}$  where  $\nu$  is an integer; reducing everything to the first Brillouin zone,

$$p_{m,n}(k) = \langle \theta_m(k) | \hat{p} | \theta_n(q) \rangle = a \delta_{k,q} \sum_j C_{l,m}(k)^* C_{j,n}(k) (k + G_j). \quad (4.8)$$

In other words the momentum operator only couples Bloch states with the same  $k$ . This is extremely important for us, because we will use Bloch states as a basis for solving the TDSE: the  $\delta_{k,q}$  in Eq. (4.8) will decouple the system of differential equations, allowing the calculation of each  $k$  separately (see next paragraph).

Since we have chosen the velocity gauge, we have to be aware of its weak points and develop the modelization accordingly. In the first place, we will use the expression for the current density Eq. (1.23) which will cancel the non-physical contribution coming from the gauge. In the second place we must be very careful in the description of quantum states and the calculation of momentum matrix elements: the reason is that an infinitesimal small field distorts the initial state to a larger extent in the velocity gauge than in the length gauge. Let's consider the evolution of a quantum state which is initially in the unperturbed eigenstate  $|\theta_{n_0}\rangle$ , under the action of a very small field  $E(t)$  with vector potential  $A(t)$ : let's say that we want to represent its evolution in the basis of the other Bloch states and compare it in the two gauges. In the length gauge we expect the field to slightly distort the initial state, in such a way that we need few other states of the basis to describe it; if the field is small enough it may not couple different states, providing the initial state just with a phase factor. In the velocity gauge, let us consider the wavefunction for a small field  $A(t) \rightarrow 0$

$$|\psi\rangle = e^{-iA(t)x} |\theta_{n_0}\rangle \approx (1 - iAx) |\theta_{n_0}\rangle : \quad (4.9)$$

the decomposition of this state on the basis of Bloch states (see next paragraph) will require non-trivial coefficients, no matter how small the field is. We will have to carefully check the dimension of the basis and we will not be allowed to use any ansatz or reasonable guess for the momentum matrix elements: we will stick strictly to those calculated from Eq. (4.8).

**Numerical Solution of the TDSE** The goal is to calculate the evolution of the wavefunction  $|\psi(t)\rangle$  in the potential  $U(x)$  under the effect of the field, described by the vector potential  $A(t)$ . This is formally described by the TDSE

$$i \frac{\partial}{\partial t} |\psi(t)\rangle = \hat{H} \psi , \quad (4.10)$$

where the interaction Hamiltonian in the velocity gauge is

$$\hat{H} = \hat{H}_0 + A(t)\hat{p} . \quad (4.11)$$

We use the eigenstates of  $\hat{H}_0$  (Bloch states) as a basis for solving the TDSE: since they are eigenstates of a Hermitian operator, they are orthogonal and form a complete basis in the Hilbert space of the single particle. As explained in the previous paragraph, in the velocity gauge different  $k$  remain decoupled, and we can treat the solution of the TDSE separately for wavefunctions corresponding to different  $ks$ . For each quasi-momentum  $k$  we decompose the single-particle wavefunction on this basis:

$$|\psi(k, t)\rangle = \sum_{n=1}^{N_b} \alpha_n(k, t) |\theta_n(k)\rangle , \quad (4.12)$$

dropping the time dependence on coefficients  $\alpha_n(k, t)$ . In principle all the (infinite) states of the basis have to be included in this decomposition in order to cover the whole Hilbert space; in practice we extend the summation up to a finite number  $N_b$  and we check that  $|\alpha_{N_b}(t)|^2$  remains negligible ( $< 1^{-10}$ ) during the time evolution for high intensities. Already  $N_b = 10$  satisfies

this requirement. Substituting the decomposition Eq. (4.12) in the TDSE Eq. (4.10) and taking advantage of the orthogonality of Bloch states, we obtain equations of motion for  $\alpha$ -coefficients as a linear system of coupled differential equations:

$$i \frac{\partial}{\partial t} \alpha_n(k, t) = \mathcal{E}_n(k) \alpha_n(k, t) + A(t) \sum_m p_{n,m}(k) \alpha_m(k, t). \quad (4.13)$$

For each  $k$  the program calculates energy bands  $\mathcal{E}_n(k)$  and momentum matrix elements  $p_{n,m}$  from the potential, and solves the above system of equations computing coefficients  $\alpha_n(k, t)$ . In most cases there is no reason to compose back the wavefunction as in Eq. (4.12), since we can express many physical quantities in terms of  $\alpha$ -coefficients. The general rule is that we can express in this way all the quantities which do not depend on the coordinate  $x$ . For example we can consider the electric current, averaged over the unit cell (taking into account the gauge term):

$$J_k(t) = - \int_{-\frac{a}{2}}^{\frac{a}{2}} \text{Im} [\psi_k(x, t)^* \partial_x \psi_k(x, t)] dx - A(t), \quad (4.14)$$

and using Eq. (4.12) rewrite it as

$$J_k(t) = -\text{Re} \left[ \sum_{n,m} \alpha_n(k, t)^* \alpha_m(k, t) p_{n,m} \right] - A(t). \quad (4.15)$$

For what concerns the electron population  $p_n$  in band  $n$ , one could naively assume (we did it for several months before realizing the problem) that it is just

$$p_n = |\alpha_n(k, t)|^2. \quad (4.16)$$

In general this is wrong because the coefficient  $\alpha_n$  represents just the probability amplitude of being in the Bloch state  $n$ : Bloch states are eigenstates of the field-free Hamiltonian  $\hat{H}_0$ , and in the presence of the field they are just a basis, with no direct physical meaning. The only thing that we can claim is that Eq. (4.16) is true after the pulse is gone. For a deeper analysis of a proper definition of field-dressed states, representing Bloch states distorted by the field, see Sec 4.5.

In an actual calculation we have to take into account contributions from all  $k$ s and from both valence bands. We will therefore consider  $2N_k$  initial conditions (where  $N_k$  is the number of grid points in the first Brillouin zone) and add up the results. For example, if  $J_k^0(t)$  is the current density calculated for an electron in a state of the lowest valence band with a quasi-momentum  $k$ , and  $J_k^1(t)$  is the current density for an electron that starts in the upper valence band, we define the net current density as

$$J(t) = J^0(t) + J^1(t) = c \int_{-\frac{\pi}{a}}^{\frac{\pi}{a}} J_k^0(t) dk + c \int_{-\frac{\pi}{a}}^{\frac{\pi}{a}} J_k^1(t) dk. \quad (4.17)$$

In integrating over  $k$  in the first Brillouin zone we should include the factor  $c$  relating the one-dimensional result with the 3D one. Instead we will take it as a free parameter and adjust it

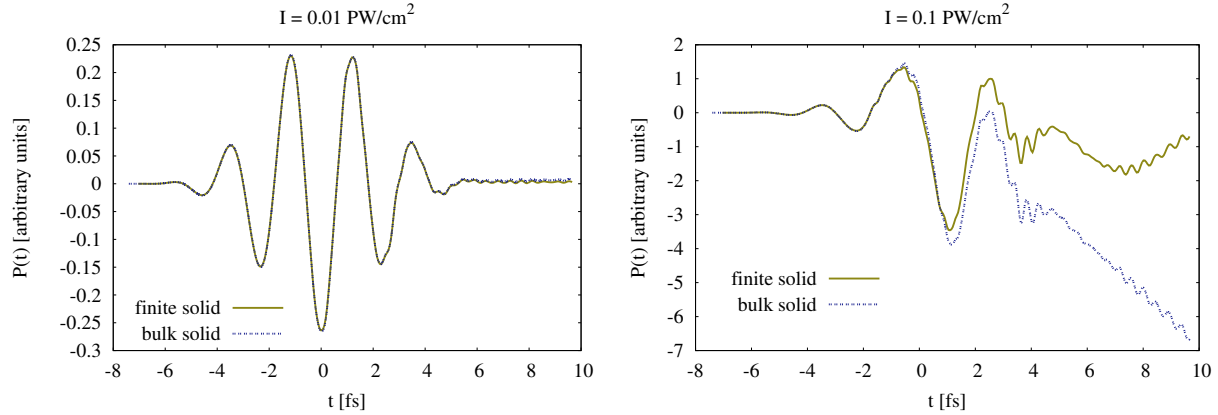


Figure 4.2: **Finite and bulk solid.** Comparison of the numerical solution of the TDSE with  $M = 51$  wells (finite solid) and with periodic boundary conditions (bulk solid). The quantity chosen for the comparison is the polarization  $P(t)$ ; for the finite solid it is evaluated in the central cell. If the intensity is not too high the agreement is perfect. For very high intensities the differences of the two models become evident. With periodic boundary conditions, in absence of relaxation terms the current just keep flowing; in the finite solids it reaches the boundary and starts oscillating.

to obtain the expected linear response of  $\text{SiO}_2$  for a low field. We evaluate the polarization response from the current  $P(t) = \int_{-\infty}^t J(t') dt'$  (see Sec. 3.4) and adjust  $c$  in such a way that  $P(t) = \epsilon_0 \chi_{\text{SiO}_2} E(t)$  for low intensities; the susceptibility of silicon dioxide at the central NIR frequency is  $\chi_{\text{SiO}_2}(750 \text{ nm}) = 1.13$  [66].

We have tested our code on different grounds. We have checked that in the limit of zero potential  $U(x) = 0$ , it predicts the dynamics of a free electron accelerated by the field i.e. the Volkov solution (see Sec. 1.5.1). We have compared the electric current calculated from our tool with the one obtained from a more complex code, which solved the von Neumann equations for the density matrix: in principle the density matrix approach is suitable to study many-particle dynamics and to include scattering phenomena, but we have checked that in the limit of the single particle the result agrees with our TDSE solution. Finally, we have considered the numerical solution for the dynamics of an electron in a potential with  $M$  identical wells. For intensities not too high the current in the central cell is the same that we obtain with our periodic boundary conditions, as it should (see Fig. 4.2). At higher intensities, results become sensitive to the differences of the models.

## 4.2 Steering Current in a Dielectric

The leading thread in this chapter is the possibility to excite electrons from valence bands of a dielectric to its conduction bands, donating it the characteristics of a metal for a short period of time. The most striking change, and also the most straightforward one to study, is its sudden ability to conduct electric current. A deep comprehension of this phenomenon is important, as this points in the direction of the signal processing with dielectrics; on the other hand it also has its own fundamental interest, as it is directly connected to some concepts not completely

understood yet, like the sub-cycle excitation rate and transport properties of dielectrics.

We use our numerical tool to calculate the current induced in the sample, and we systematically investigate how we can steer it acting on the intensity and the CEP of the laser pulse (Sec. 4.2.1). We also had the opportunity to compare our result with an experiment where an NIR laser pulse was actually shone on a SiO<sub>2</sub> sample, and the total charge transferred during the interaction was measured. Even though our model will not fully describe the measurement device and in spite of approximations made, several features of the experiment are reproduced in our calculations (Sec. 4.2.2).

### 4.2.1 Theoretical Analysis

We simulate the dynamics of a single electron in the periodic potential discussed above, in response to an electric pulse  $E(t)$ . We do not take into account the field created by other electrons self-consistently; we include it as a collective screening effect given by the Fresnel formula Eq. (3.45). Therefore if we calculate the response to a field with an amplitude  $E_0$ , we will regard the incident laser field as having an amplitude  $E_{I0} = \frac{1+n}{2}E_0$  and an intensity  $I = \frac{\epsilon_0 c}{2}E_{I0}^2$ . All the results in this section are expressed in terms of the incident field or intensity in order to directly compare them with the experiment. Since we solve the TDSE in one dimension we have no choice but to consider an electric field linearly polarized. The electric field applied in the simulations is a few-cycle laser pulse

$$E(t) = E_0 f(t) \cos(\omega_0 t + \phi) , \quad (4.18)$$

where  $\phi$  is the Carrier Envelope Phase (CEP). The square of the envelope  $f^2(t)$  has a full width half maximum (FWHM) of 3.7 fs, and the pulse central wavelength is 746 nm (i.e. the period is  $T \sim 2.5$  fs and the central frequency is  $\omega_0 \sim 0.061 = 1.63$  eV). We evaluate the net surface charge transferred through the single cell as the integral of the current density:

$$\sigma(t) = \int_{-\infty}^t J(t') dt' , \quad (4.19)$$

where  $J$  is evaluated as in Eq. (4.17). In order to calculate the charge transferred we have to multiply it by the effective section where the current can flow. Note that the transferred charge density corresponds to the polarization  $\sigma(t) = P(t)$  (see Eq. (3.29)). The superposition of electrons in conduction and valence states creates high-frequency oscillations in the current, due to quantum beating between the levels. These oscillation will be studied in details in Sec. 4.3: here we focus on the net transfer of charge, and we do not want these high-frequency components to spoil our analysis. For this purpose we apply a low-pass Fourier filter to the current before integrating it. A comparison of  $\sigma(t)$  obtained with and without filtering is shown in Fig. 4.3. Another problem in the analysis is that the current would keep on flowing, due to the lack of relaxation effects in our model. In reality the current has a fast relaxation time [60]: we account for this, freezing the charge at a certain time  $t_f$  after the laser pulse is gone. The arbitrariness of this final time will change a bit the final value of the charge, but not its qualitative dependence on the CEP and on the intensity. We will regard  $S = \sigma(t_f)$  as the total charge transferred during the interaction with the laser field, and it will be our main observable in this section.

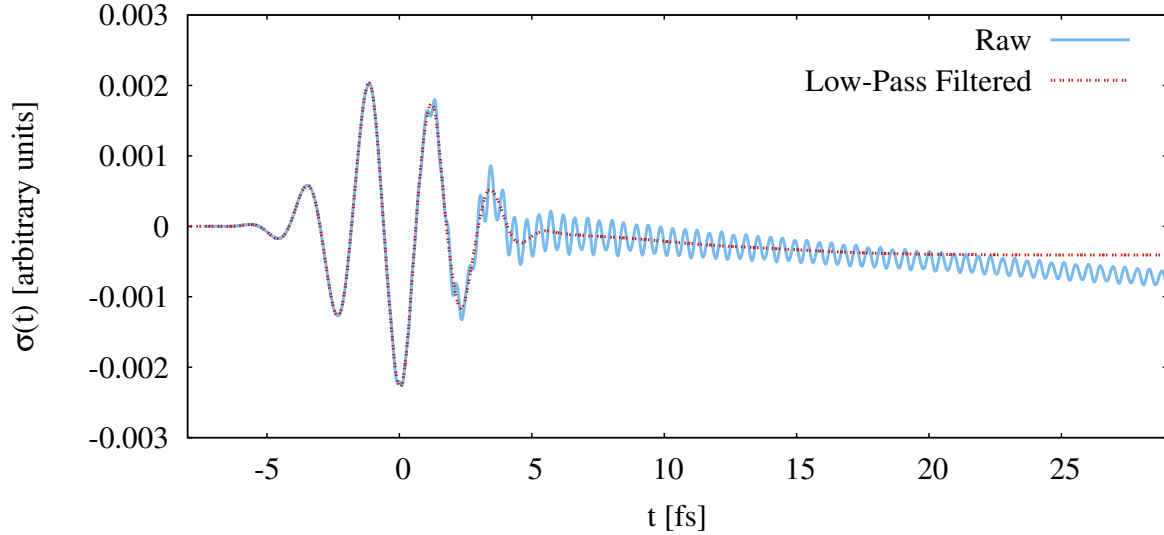


Figure 4.3: **Effect of the low-pass filter.** Comparison of the transferred charge  $\sigma(t)$  before and after the Fourier filtering. In our calculation the charge would flow indefinitely but the Fourier-filtered one stops, because of the multiplication by a soft window in the time domain. This simulation was done for a laser intensity  $I = 0.03 \text{ PW/cm}^2$ .

Adding  $\pi$  to the CEP is exactly equivalent to changing the sign of the electric field, and the sign of  $J(t)$  together with it. It is therefore evident that the current will depend on the CEP  $\phi$ , and that it will oscillate as we change  $\phi$  from 0 to  $2\pi$ . For the same reason also the total charge transferred during the whole interaction  $S(\phi) = \sigma(t_f, \phi)$  will oscillate as a function of  $\phi$ : this is shown for different intensities in Fig. 4.4. Operating on the CEP is therefore a way to control the amount of charge displaced in a solid sample on a fs timescale. This evidence is full of promises: on one hand it is a first realistic hint on ultrafast signal processing, on the other hand it suggests the possibility to realize a solid state device able to measure the CEP. The reason why in our calculation  $S(\phi)$  has its maximum at different phases for different intensities is not yet totally clear. An experiment is currently devoted to the detailed study of the CEP dependence, and the comparison of different theoretical models may shed light on the cause of the shift. We will have to pay attention to the proper way of comparing  $S$  for different intensities, so that they are not affected by the CEP: we will always consider the maximum over the CEP,  $S_{\max} = \max_{\phi \in (0, 2\pi)} |S(\phi)|$ .

The different attempts to provide an analytical description of the tunneling process in solids (see Sec. 3.3) predict a (cycle-averaged) tunneling rate growing exponentially with the amplitude of the field  $|E|$ , with a characteristic shape  $e^{-\frac{1}{|E|}}$  (see Eq. (3.18)). For low intensities, before we enter the tunneling regime, we would expect the density of excited electrons to show a polynomial dependence on the field, characterizing the multi-photon excitation. These excitation regimes are not reflected in the displaced charge. Our data analysis (see Fig. 4.5) shows that  $S_{\max}$  grows exponentially with the field amplitude, and that this growth is best fit by  $e^{|E|}$ , with no sign of the multiphoton regime. On the contrary, the dependence seems to become sub-exponential at higher intensities. These unexpected regimes are also observed experimentally, as discussed in

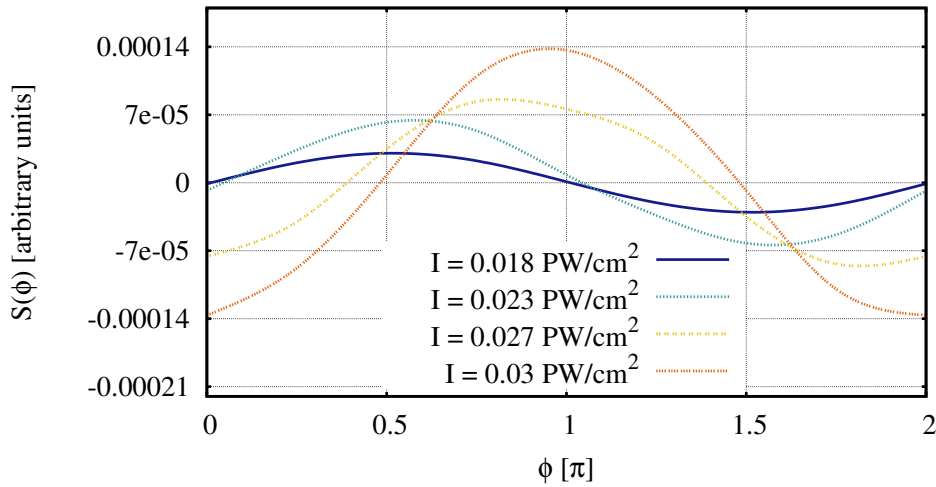


Figure 4.4: **CEP dependence.** The displaced charge  $S$  oscillates with the CEP of the incident pulse. The amplitude of oscillations grows with the intensity: this growth is analyzed in detail in the following. The reason of the shift with growing intensity is not clear yet and it is currently subject of investigation.

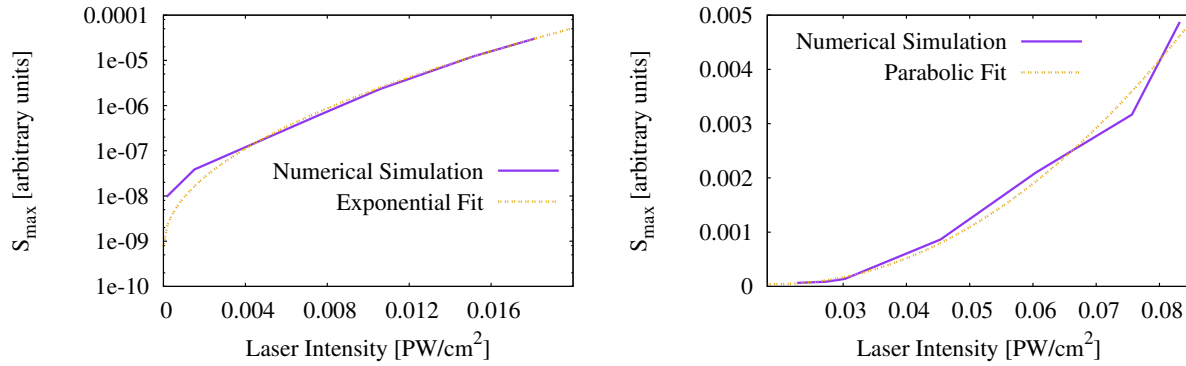


Figure 4.5: **Intensity dependence of the displaced charge.** A figure with a unified intensity range is reported in Fig. 4.7. **Left Panel:** Even at low intensities, the displaced charge grows as  $\sim e^{|E|}$ : the fit is exponential in the field, thus in the squared root of the intensity. **Right Panel:** For higher intensities the dependence is sub-exponential. The fit is parabolic in the intensity.

the next section.

## 4.2.2 Comparison with the Experiment

In the experiment [56], a fused silica sample was exposed to a strong few-cycle laser pulse  $E(t)$  with frequency  $\omega_0 \sim 0.062 = 1.7$  eV. Two gold electrodes were connected to the sample for collecting the current induced by the strong field: a schematic view of the metal-dielectric-metal junction is shown in Fig. 4.6. The sample was  $\sim 100$  nm tall and  $\sim 100$   $\mu\text{m}$  wide; we obtain a section  $\Sigma = 10^7$   $\text{nm}^2$  which we use to calculate the charge from the surface density  $S$ . The

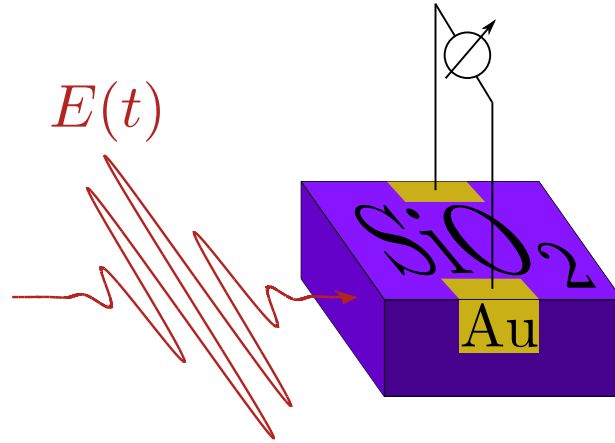


Figure 4.6: **Schematic of the metal-dielectric nanojunction.** Displaced charge is accumulated in the gold contacts and discharges through the current detector.

laser intensity was reduced with an iris (waist  $\sim 50$  nm), and the CEP was shifted upon changing the propagation length in a pair of thin fused silica wedges. In the measurement the result of different polarizations was studied, but for the comparison with our 1D model we will consider just the polarization perpendicular to the metal-dielectric interface. Unfortunately it was not possible to time-resolve the current during the interaction with the electric field, because the time scale of the detector was several orders of magnitude slower than the period of the laser pulse. Therefore we are not able to directly compare the current, we will rather compare the charge  $Q$  transferred between the electrodes during the whole interaction: we will assume that all the charge which reached the boundaries of the sample (i.e. the current flowing in the single cell of our model) contributes to the charge measured. In order to compare our data with the measurement, we had to rescale them because we overestimated the current by three orders of magnitude: this can be due to the overestimation of the matrix elements and to the absence of scattering and lattice dynamics in our model. Nonetheless the qualitative comparison is very interesting (Fig. 4.7). For lower intensities the exponential growth observed in the measurement is correctly reproduced by our calculation: for higher intensities both the numerical simulation and the experiment show a sub-exponential dependence on the field but with a different slope. On the other hand, experimental data are less reliable at high intensity, as the large error bars testify. The steep dependence of the current on the intensity has been employed to steer the current with a second CEP-stabilized laser pulse; this was accomplished in the same experiment presented in this section.

### 4.3 Highly Nonlinear Polarization Response

Within the model presented in Sec. 4.1 we are able to calculate the response to the field  $E$  of electrons moving in a periodic potential. In this section we study the dielectric response of the material to an intense electric field. Electrons excited to the conduction band drastically change the electric properties of the material: not only do they have a different mobility and



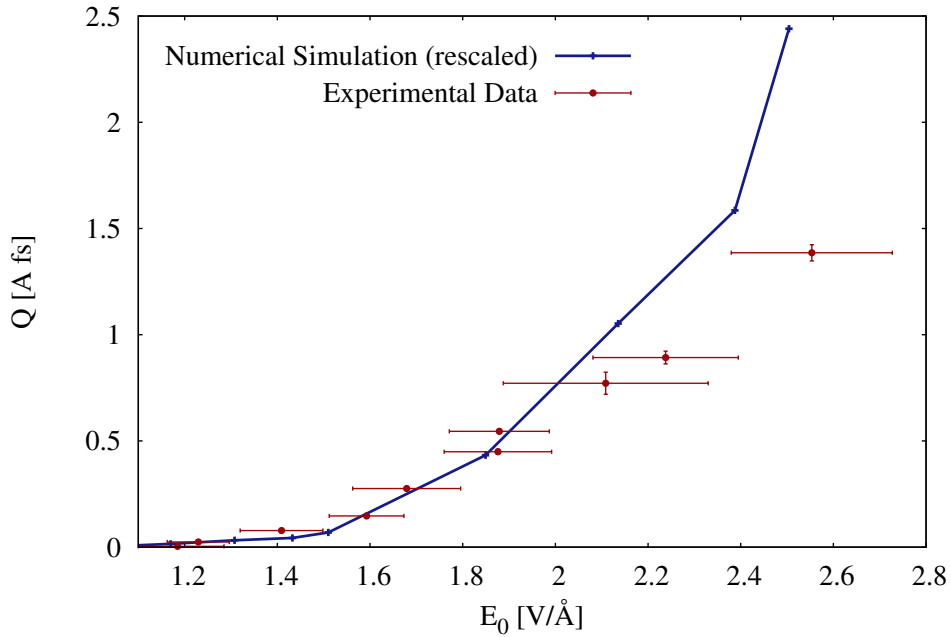


Figure 4.7: **Comparison with experimental result** In the figure we directly compare the displaced charge predicted numerically with the experimental result. The numerical result had to be rescaled by a factor  $\sim 1000$ .

hence a different response to the field, but the coherent superposition of electron wavepackets in valence and conduction bands results in quantum beats, which are expected to emit a peculiar electromagnetic signal. It is meaningful to wonder, whether signs of the interband excitation are present in the radiation emitted by the sample in response to the external field, and whether it is possible to measure them.

As the intensity increases, the simple picture of electrons displaced from their parent ions creating a nonzero dipole moment (Eq. (3.19)) is no longer reliable: even higher order expansion describing the response in terms of growing power of the field are supposed to break down, since the tunnel excitation is governed by an exponential law. In this section we focus on this partially unexplored regime: we will explain the nonlinear response in terms of physical phenomena related to the interband excitation, and retrieve some information about these dynamics which would otherwise remain inaccessible.

We will consider the electron response to an electric field  $E(t)$ : we will assume that this is the field in the material and we do not investigate how this is related to the incident field  $E_I(t)$ . This is a good starting point to understand what are the most important phenomena triggered by interband tunneling. In the next Sec. 4.4 we will focus on the problem of relating the incident, transmitted, and reflected field, carrying our analysis closer to what could actually be measurable.

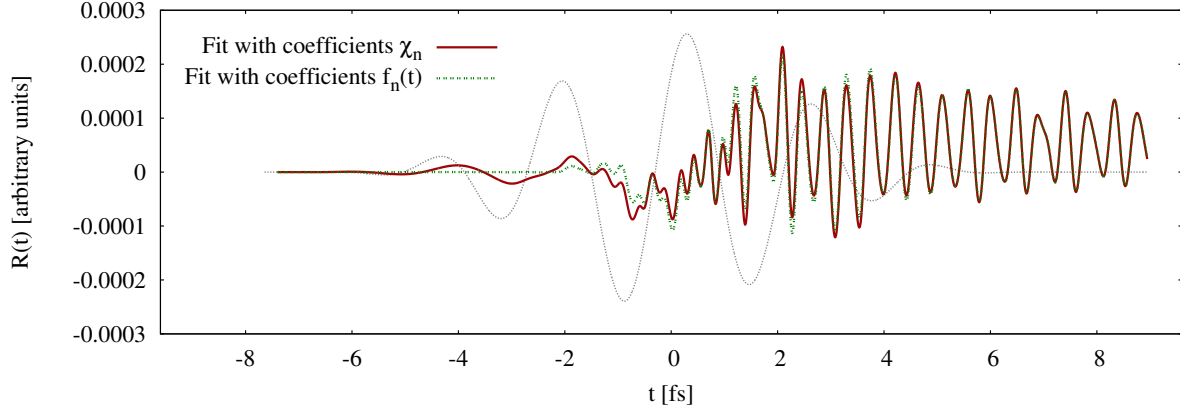


Figure 4.8: **Isolating  $R(t)$ .** The electric field (dotted in the figure) is reported for reference, rescaled to fit into the plot. If  $R(t)$  is simply defined as what remains out of the polynomial fit in Eq. (4.21) (red curve), some low-frequency contributions show up for the whole duration of the pulse. Taking into account the non-instantaneous response as in Eq. (4.22) (green curve) makes these contributions disappear and  $R(t)$  is exactly zero before the interband excitation takes place. This calculations was done for an electric field amplitude  $E_0 = 0.73 \text{ V/\AA}$

### 4.3.1 Real Time Interband Excitation

We calculate the current response  $J(t)$  (averaged over the unit cell, see Eq. (4.17)) with our numerical tool: we obtain the polarization response as  $P(t) = \int_{-\infty}^t J(t') dt'$ . The polarization is expected to have a term linear in the field, a non-linear one, and a term holding the interband excitation response:

$$P(t) = P_L(t) + P_{NL}(t) + R(t). \quad (4.20)$$

The main problem that we face in the analysis is to separate the term relevant for us  $R(t)$  from the rest. If the response were instantaneous we could fit  $P(t)$  with a power expansion in the field, and define  $R(t)$  as the difference between the total polarization and the fit:

$$P(t) = \epsilon_0 \chi_1 E(t) + \epsilon_0 \chi_3 E^3(t) + \epsilon_0 \chi_5 E^5(t) + \dots + R(t); \quad (4.21)$$

coefficients of even powers are zero because the potential is symmetric. Unfortunately this system is not effective in isolating the signal from excited electrons, and some contribution appear  $R(t)$  before the field has any chance to trigger the inter-band excitation (see Fig. 4.8): the reason is that Eq. (4.21) assumes an instantaneous response, leaving some non-instantaneous contributions in  $R(t)$ . The non-instantaneous response is usually described in frequency domain (see Sec. 3.5.1) but we can find a shortcut not to do a Fourier analysis (which would introduce some artifacts). Eq. (3.36) shows that the  $n$ th term in the non-instantaneous expansion is proportional to  $E_0^n$ , where  $E_0$  is the amplitude of the applied electric field. The non-instantaneous polarization response therefore can be written as

$$P(t) = f_1(t) E_0 + f_3(t) E_0^3 + f_5(t) E_0^5 + \dots + R(t), \quad (4.22)$$

where time dependent functions  $f_n(t)$  take the place of susceptibilities in Eq. (4.21); they fully describe the linear and nonlinear part  $P_L + P_{NL}$  of the polarization response. In order to determine

these time-dependent coefficients, we assume that  $R(t) = 0$  if the amplitude of the field is low enough not to trigger any tunneling process; we consider two amplitudes  $E_a$  and  $E_b = \alpha E_a$  both of them very low such that

$$\begin{aligned} P_a(t) &= E_a f_1(t) + E_a^3 f_3(t) \\ P_b(t) &= E_b f_1(t) + E_b^3 f_3(t). \end{aligned} \quad (4.23)$$

We can calculate  $P_a(t)$  and  $P_b(t)$  using our numerical tool and obtain the unknown functions from them,

$$\begin{aligned} f_3(t) &= \frac{1}{(\alpha^3 - \alpha) E_a^3} (P_b(t) - \alpha P_a(t)) \\ f_1(t) &= \frac{1}{(\alpha^3 - \alpha) E_a} (\alpha^3 P_a(t) - P_b(t)). \end{aligned} \quad (4.24)$$

In principle this procedure can be applied to calculate higher order  $f_n$  – employing the polarization responses to  $n$  different (low) amplitudes – but the two terms in Eq. (4.24) are actually enough for our calculations. The comparison between the two different approaches is showed in Fig. 4.8: it is clear that using the second procedure the term  $R(t)$  is zero until the peak of the field excites something, as expected.

We will show in the rest of this section that the quantity  $R(t)$  carries quite some information about the excitation process. The coherent superposition of valence and conduction band states beats with frequency equal to the band gap, and it is reasonable to expect the amplitude of these oscillations to be proportional to the excited population; we perform a time-frequency analysis of  $R(t)$  to obtain an insight into the time-evolution of the tunneling excitation. For the analysis we have Fourier transformed a slice of the signal, applying a temporal window with constant width  $\Delta t \sim 1$  fs centered on  $t_0$ . Moving  $t_0$  through the whole signal give the analysis shown in (Fig. 4.9), where the Fourier transform is reported on vertical lines and the horizontal axis is  $t_0$ . The signal appears when the electric field is strong enough to excite electrons, and it is centered around the frequency approximately corresponding to the band gap:  $8.9$  eV  $\approx 5.4 \omega_0$ , where  $\omega_0 = 0.061$  is the frequency of the laser pulse. The bandwidth of the signal is due to the integration over  $k$  (see Eq. (4.17)), because different band gaps correspond to different  $ks$ . Our analysis shows that if it were possible to detect those high-frequency oscillations, a measurement of the emitted field would convey data about electron dynamics taking place in the dielectric during inter-band excitation. On the other hand, similar calculations can also be used to evaluate the portion of electrons excited as a function of time, and in the presence of the field: this piece of information can be extremely important in the area of “field dressed states” (see Sec. 4.5), where it can be used as test ground for different mathematical descriptions of states in the presence of the field.

Peculiarities of electron response after the excitation show up also in the phase of the polarization, which was neglected in the above analysis, where we considered just its modulus. Wavepackets in higher energy states are less bound and respond differently to the field. Our polarization response comes from the interplay of electrons in different bands, with different binding strength: this produces a non-trivial phase dependence on the intensity, showed in detail in Fig. 4.10. We analyze the spectral phase of the polarization response and compare it with the one calculated for a very low intensity, where excitation effects are not supposed to play any role. The phase shift is significant (reaching values up to a fraction of  $\pi$ ) and could trigger a measurable effect, since the polarization response is the source of the reflected field and directly

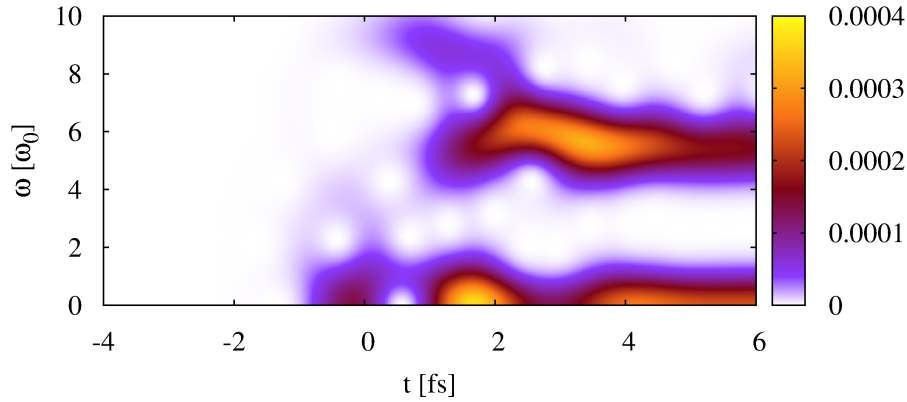


Figure 4.9: **Time-frequency analysis of  $R(t)$** . In this figure we show the time-frequency analysis of  $R(t)$  plotted in Fig. 4.8. Frequencies are measured in unit of the laser frequency  $\omega_0$ . This kind of analysis provides us with real-time information about the tunneling process: high-frequency components are centered on the band gap and their intensity is proportional to the fraction of electron excited. This component would never disappear, because in our model no relaxation or dephasing effect is taken into account. Low-frequency components ( $\sim 1 \omega_0$ ) in the center of the pulse are mainly due to excited electrons moving in the conduction band accelerated by the field; low-frequency noise after the pulse is created by the non-zero offset of the oscillations.

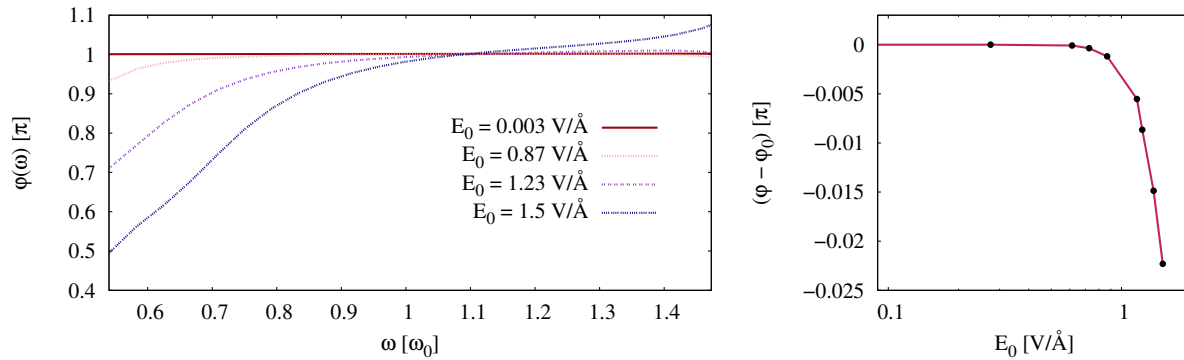


Figure 4.10: **Phase shifted electron response**. Superposition of low- and high-energy electronic states produces a non-trivial phase response to the field. In the left panel we report the spectral phase of the polarization response  $P(t)$  around the central frequency of the laser pulse  $\omega_0$ , for different intensities: the change of phase experienced increases with the field. This behavior is summarized in the right panel where we plot the change of phase (averaged around  $\omega_0$ ): the scale of the horizontal axis is logarithmic to show the behavior on a longer range. The reference phase  $\varphi_0$  is chosen at the amplitude  $E_0 = 0.003 \text{ V/\AA}$ .

affects the transmitted field: the mechanisms governing these processes will be discussed in the next section.

## 4.4 Transmitted and Reflected Field

In general the field  $E$  (transmitted field) results from the interplay between the external incident field  $E_I$  and the electrons themselves. As we have seen, interband tunneling triggers peculiar electron dynamics which will play a non trivial role in modifying the incident field. In this section we construct a procedure to self-consistently relate the transmitted field  $E$  and reflected field  $E_R$  to the motion of electrons.

Yabana et al. [67] have studied modifications occurring in the reflectivity of crystalline silicon using the Time Dependent Density Functional Theory (TDDFT) approach. They have found that after a certain intensity of the incident field, the reflectivity steeply increases: this is consistent with the picture of charge carriers excited to the conduction band, marked by a larger mobility and polarizability. We investigate similar effects with our tool, focusing on the qualitative changes occurring in the reflected pulse: our goal is to explicitly relate these effects with the electron dynamics responsible for them.

### 4.4.1 Approximate Solution of the Scalar Wave Equation

Consistently with our 1D model we will consider the normal incidence of a linearly polarized field (see Fig. 4.11). The exact solution to the problem of calculating the transmitted and reflected field would be provided by the *scalar wave equation*,

$$\partial_z^2 E(z, t) - \frac{1}{c^2} \partial_t^2 E(z, t) = \frac{1}{\epsilon_0 c^2} \partial_t [J(z, t) + \partial_t P(z, t)] ; \quad (4.25)$$

this equation relates the propagation of the field to the current  $J$  and the polarization  $P$  which the field itself generates inside the material. We want to avoid a direct numerical solution of Eq. (4.25) and in the following we will try instead to use it to derive a simple relation between the transmitted field and the current; The current  $J$  is usually understood as the result of free moving charges, the polarization  $P$  of bound charges. As discussed in Sec. 3.4, current and polarization are closely related ( $J = \partial_t P$ ), and since in our model there is no clear distinction between free and bound electrons, we will consider only the current as the source term. In order to approach the analytical solution of the above differential equation we need the initial condition for the transmitted field, which we can obtain from the theory of dielectrics: the tangential component of the electric field (which is the only non-zero component in our case) is continuous across the boundary  $z = 0$ ,

$$E_I(0, t) = E(0, t) - E_R(0, t) , \quad (4.26)$$

and the magnetic field is continuous as well

$$B_I(0, t) = B(0, t) - B_R(0, t) . \quad (4.27)$$

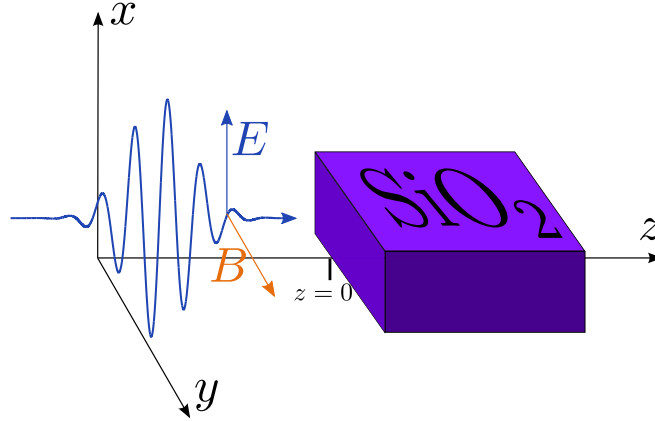


Figure 4.11: Outline of the system.

Taking advantage of the Maxwell equation  $\nabla \times \mathbf{E} = \partial_z E_x = \partial_t B_y$ , we can convert Eq. (4.27) in a boundary equation for the electric field:

$$\partial_z E_I(0, t) = \partial_z E(0, t) - \partial_z E_R(0, t). \quad (4.28)$$

Outside the dielectric ( $z < 0$ ) the electric field is a wave propagating with the speed of light,  $E_{I/R}(t, z) = E_{I/R}(t \mp \frac{z}{c})$ ; therefore its time and space derivative are connected by the relation  $\partial_z E_{I/R}(t, z) = \mp \frac{1}{c} \partial_t E_{I/R}$ . Substituting them into Eq. (4.28) and Fourier transforming it we obtain

$$\partial_z E(0, \omega) = \frac{i\omega}{c} (E_I(0, \omega) - E_R(0, \omega)), \quad (4.29)$$

where the Fourier transform of a function is simply indicated by its explicit dependence on  $\omega$ . Combining Eq. (4.29) and Eq. (4.26) we finally get the condition relating the transmitted field and the incident field at the boundary:

$$\partial_z E(0, \omega) = \frac{i\omega}{c} (2E_I(0, \omega) - E(0, \omega)). \quad (4.30)$$

Knowing the initial condition for the transmitted field we can now approach an approximate, analytical solution of (4.25), starting with its Fourier transform

$$\partial_z^2 E(z, \omega) + \frac{\omega^2}{c^2} E(z, \omega) = -\frac{i\omega}{\epsilon_0 c^2} J(z, \omega). \quad (4.31)$$

The velocity of the field in the medium is dictated by the refractive index  $n = c/v$ . We can thus consider a quantity comoving with the field

$$U(z, \omega) = E(z, \omega) e^{-i\frac{z}{v}\omega}; \quad (4.32)$$

in terms of this quantity the scalar wave equation reads

$$\partial_z^2 U(z, \omega) + \frac{2i\omega}{v} \partial_z U(z, \omega) - \omega^2 \left( \frac{1}{v^2} - \frac{1}{c^2} \right) U(z, \omega) = -\frac{i\omega}{\epsilon_0 c^2} e^{-i\frac{\omega}{v}z} J(z, \omega). \quad (4.33)$$

In the so-called *slowly-evolving-wave approximation* [68] the second derivative of  $U$  is neglected: this would not be appropriate here because the field can develop low-frequency components during the evolution, making all the terms proportional to  $\omega$  negligible. Instead we will assume that the current simply propagates with the same velocity of the field  $J(z, \omega) = J(0, \omega) e^{i\frac{z}{v}\omega}$ , so that the right hand side of Eq. (4.33) is independent on  $z$ : this is the case for example if the response is linear. Within this approximation Eq.(4.33) can be solved exactly

$$U(z, \omega) = e^{-i\frac{z}{v}\omega} \left[ c_1 e^{-i\frac{z}{c}\omega} + c_2 e^{i\frac{z}{c}\omega} \right] + \frac{i}{\epsilon_0 c} \left( \frac{v^2}{c^2 - v^2} \right) J(\omega), \quad (4.34)$$

where  $c_1$  and  $c_2$  are constants, to be determined from the boundary conditions. This solution clearly shows a contribution from waves propagating in two opposite directions (in square brackets). We can determine the coefficient for the forward-propagating wave using the condition (4.30): unfortunately there is no way to determine the coefficient of the back-propagating wave without the exact solution of Eq. (4.25), because we would need to know either the value of the field at  $z \neq 0$  or its derivative at  $z = 0$ , which is itself determined by the reflected field. We are therefore forced to drop the back-propagating wave, imposing  $c_1 = 0$ . At low intensities this approximation is exact because the field propagates just in the forward direction, all the back-propagating waves interfering destructively. As the intensity is increased, more and more electrons are excited to conduction bands: this in turn increases the plasma frequency which is proportional to the density of electrons contributing to the oscillations. When the plasma frequency approaches the frequency of the injected field, this approximation becomes critical because the evanescent field can not be described without back-propagating waves. The appearance of plasma oscillations, as it happens in our calculations, is showed in Fig. 4.12.

The coefficient  $c_2$  is readily evaluated from the initial condition in terms of the field at the boundary of the dielectric; we write the solution for the transmitted field,

$$E(z, \omega) = E(0, \omega) e^{i\frac{z}{c}\omega} + \frac{iJ(\omega)}{\epsilon_0 \omega} \left( \frac{v^2}{c^2 - v^2} \right) \left[ e^{i\frac{z}{v}\omega} - e^{i\frac{z}{c}\omega} \right]. \quad (4.35)$$

Since we are not interested in the propagated field but just in the modification occurring in the reflected and transmitted field at the boundary, we restrict our analysis to  $z = 0$ . In order to relate the incident and transmitted field we consider the first derivative of the above equation and take advantage of Eq. (4.30) obtaining:

$$E(0, \omega) = E_I(0, \omega) - \frac{iJ(\omega)}{2\epsilon_0 \omega (1 + n(\omega))}. \quad (4.36)$$

As expected, this equation relates the transmitted field and the current, which is in turn generated by the transmitted field itself. Ignoring the dependence of the refractive index on the frequency may prevent us from correctly including many physical effects in our model, but is the only direct way to write the equation back in the time domain:

$$E(t) = E_I(t) - \frac{1}{2\epsilon_0 (1 + n)} \int_{-\infty}^t J(t') dt'. \quad (4.37)$$

In case of linear response  $P(t) = \int_{-\infty}^t J(t') dt' = \epsilon_0 \chi E(t)$ , this equation reduces to Fresnel equation as it is supposed to do.

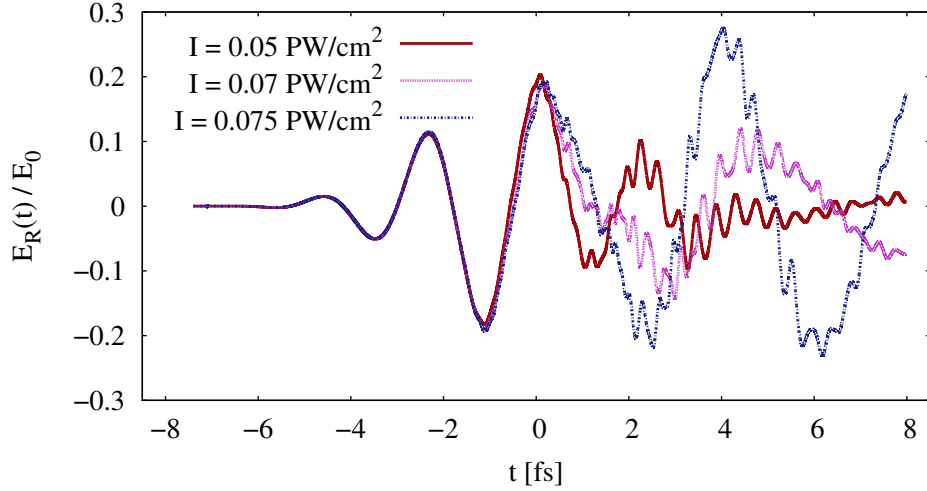


Figure 4.12: **Reflected field.** Reflected fields  $E_R$  for different intensities of the incident field  $E_I$ : curves were rescaled with the amplitude of the incident field  $E_0$ . As long as the electric field is not large enough to excite electrons, the response is linear; after the excitation (at  $\sim -1$  fs) the reflected pulse gets distorted. High frequencies appear due to quantum beating (see Sec. 4.3), plasma oscillations acquire amplitude and frequency increasing with the intensity, and a small phase shift is visible.

#### 4.4.2 Self Consistent Calculation

We have calculated the transmitted field solving Eq. (4.37) self-consistently. For the self-consistent calculation we have included two additional equations to the system Eq. (4.13), describing the relation between the self-consistent vector potential and the current:

$$\begin{cases} \partial_t A(t) = \partial A_I(t) + \frac{1}{2\epsilon_0(1+n)} P(t) \\ \partial_t P(t) = J(t) \end{cases} \quad (4.38)$$

where we have indicated with  $A_I$  the vector potential of the incident field. The whole system of differential equations was solved numerically with a second-order Runge-Kutta algorithm, updating  $J$  and  $P$  at each intermediate step. The solution provides us with the self-consistent field  $E(t)$  and hence the reflected field evaluated from Eq. (4.26). As expected, as long as the intensity is small ( $I < 0.001$  PW/cm<sup>2</sup>) the response is linear, and since we have adjusted the numerical model accordingly, the evaluated polarization agrees with the dielectric constant of SiO<sub>2</sub>. Approaching higher intensities  $I \approx 0.01$  PW/cm<sup>2</sup>, the reflected pulse does carry signs of the excitation occurred in the sample (see Fig. 4.12): the high-frequency components discussed in Sec. 4.3 come into play modifying the reflected pulse, low-frequency components get distorted, and plasma oscillations appear. The frequency of plasma oscillations

$$\omega_p = \sqrt{\frac{\rho}{m^* \epsilon_0}} \quad (4.39)$$

is proportional to the density of free electrons  $\rho$ , therefore to the intensity of the incident field.

As explained in the derivation of Eq. (4.37), when the plasma frequency approaches the frequency of the laser pulse, results of our calculations are not completely reliable anymore. In



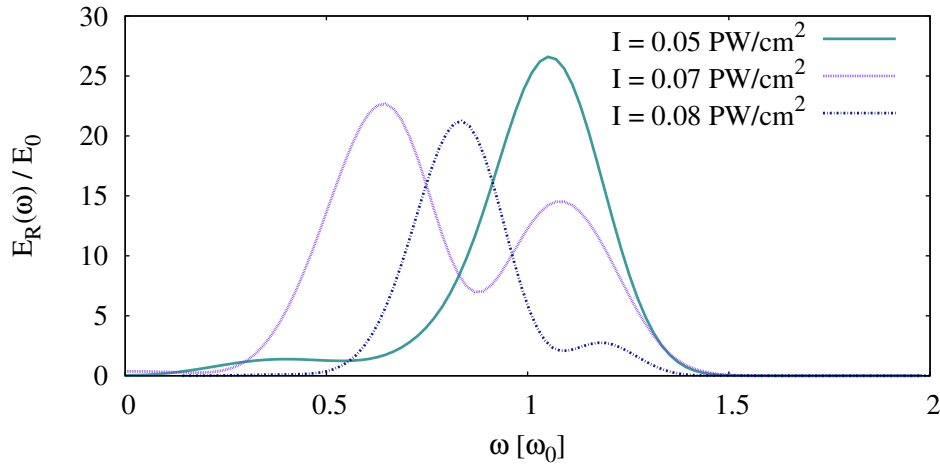


Figure 4.13: **Plasma frequency.** Spectra of the reflected pulse, for intensities of the incident field approaching the intrinsic limit of our calculations. Spectra are rescaled according to the amplitude of the field and frequencies are measured in units of the laser frequency. While at  $I = 0.05 \text{ PW/cm}^2$  plasma oscillations result just in a long tail at low frequencies, for  $I = 0.07 \text{ PW/cm}^2$  there is already some overlap with the pulse, and at  $I = 0.08 \text{ PW/cm}^2$  the plasma frequency is comparable with the laser frequency.

order to determine the range where our simulations do not suffer too much from plasma oscillations, we check at which intensity the spectrum of plasma oscillations starts overlapping with the spectrum of the laser pulse: spectra of the reflected pulse are shown in Fig. 4.13. Already at  $I = 0.07 \text{ PW/cm}^2$  plasma oscillations are clearly visible, but at this intensity they are still quite separated from the pulse; at  $I = 0.08 \text{ PW/cm}^2$  we are close to the critical point. This steep growth is due to the exponential dependence of the number of excited electrons on the intensity, while the plasma frequency increases with the number of electrons. Therefore there is a limited intensity range where the effects of interband tunneling become significant and the plasma frequency is still not too large; we will show how already in this regime the reflectivity changes and the pulse is modified, to an extent which suggests the feasibility of a measurement. The reflectivity was evaluated in a limited spectral range to avoid artifacts: we have compared the intensity of the reflected and incident pulse for frequency in the interval  $0.04 < \omega < 0.027$  corresponding to  $0.7 \omega_0 < \omega < 1.9 \omega_0$ , filtering out the beating of valence and conduction band states, and plasma oscillations. Results of this analysis are presented in Fig. 4.14. Even though the allowed range of intensities is limited, it is already possible to identify two regimes. As the plasma frequency approaches the laser frequency, the reflectivity drops because the energy is efficiently absorbed by plasma oscillations. For higher intensities our model predicts a net increase in the reflectivity, consistent with the presence of electrons in the conduction bands providing the dielectric with the properties of a metal. A similar effect is pointed out in TDDFT calculations [67], where a multiphoton excitation mechanism is investigated.

For the observation of the non-trivial behavior of the reflectivity, it should be enough to spectrally resolve the reflected power emitted by the sample. In order to detect finer details, like the phase shift and the modification in the reflected pulse showed in Fig. 4.12, it is necessary to

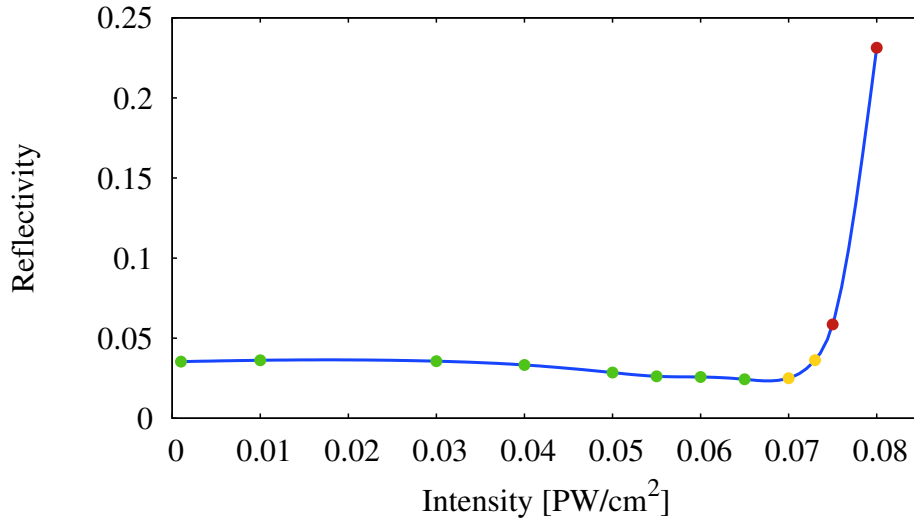


Figure 4.14: **Reflectivity.** The reflectivity is calculated in a limited frequency range, to avoid artifacts and filter out high-frequency components. Different point colors (green, yellow, red) symbolize the proximity to a critical intensity where our model is not completely reliable anymore. It is visible an initial decrease of the reflectivity, due to efficient absorption, and a steep increase when the dielectric starts showing metallic behavior: unfortunately points at high intensities are at the limit of our model.

time-resolve the reflected field; nowadays tools allow a streaking measurement (see Sec. 1.6.2) for this purpose.

## 4.5 Field Dressed States

In previous sections we have taken advantage of a numerical tool to calculate the single electron wavefunction  $\psi(x, t)$  in a periodic potential, interacting with an electric field. When the field is intense enough, part of the electron wavepacket is excited to the conduction band: we have seen the effect of this superposition in modifying the physical properties of the dielectric. In this chapter it was mentioned several times that even if we know the wavefunction, we are not able to tell apart the portion of wavepacket excited in a band  $n$ ; as a consequence, we are not able to calculate the instantaneous excitation probability in that band. In Sec. 3.3 we have reported different attempts to calculate the interband excitation rate and we have underlined that the rate was always meant for a stationary (constant field) or quasi-stationary (time-periodic field) situation. The quantum mechanical prescription to calculate the probability amplitude  $a_n$  to find a particle with wavefunction  $|\psi\rangle$  in the state  $|n\rangle$  is to project the wavefunction on this state  $a_n = \langle n | \psi \rangle$ . However, in the presence of the field, the Hamiltonian is explicitly time dependent, and it is not possible to define proper eigenstates. Let us write the Hamiltonian in the general form

$$\hat{H}(t) = \hat{H}_0 + \hat{V}(t) : \quad (4.40)$$

$\hat{H}_0$  is the Hamiltonian including the lattice potential, and  $\hat{V}(t)$  is the interaction with the field, in the length or in the velocity gauge. Bloch states  $|\theta_n\rangle$  (eigenstates of  $\hat{H}_0$ , see Eq. (4.3)) in the presence of the field become nothing more than a basis, and the projection of the wavefunction on them has no physical meaning. Therefore, even if the wavefunction ensures us the highest possible knowledge of the electron state, we do not have the right tools to *interpret* it. In this section we will try to define an orthonormal, complete set of time-dependent “field-dressed” states  $|\xi_n(t)\rangle$  which could represent the electron states distorted by the field. Once we have a proper set of similar states we can define the instantaneous excitation probability as

$$p_n(t) = |\langle \xi_n(t) | \psi(t) \rangle|^2. \quad (4.41)$$

Similar attempts are well known in different branches of physics under the name of adiabatic or quasi-static approximation, and are described in a more general framework in [69]; a similar study for atomic ionization was published in [70].

### 4.5.1 Kane and Houston Functions

A common approach to the problem is to start considering the interaction with a constant field  $E_0$ : in this case the Hamiltonian is not time dependent, and it makes sense to evaluate its eigenstates as a function of the field  $|\xi_n(E_0)\rangle$ . The key assumption to go from the static case  $E = E_0$  to the dynamic one  $E = E(t)$  is the adiabaticity: the period of the field must be much longer than the time it takes electrons to respond to it. If it is the case, one can assign the time dependence to the field-dressed states from the field and assume that  $|\xi_n(t)\rangle = |\xi_n(E(t))\rangle$  properly represents  $|\theta_n\rangle$  distorted by the field. However, even before starting an accurate quantitative analysis, we can raise a problem about this approach. Let us consider a slowly-varying field, which respects the requirement of adiabaticity: at a zero-crossing of the field, the system is supposed to be in the unperturbed equilibrium state corresponding to the field-free case. Nonetheless, we expect the particle to have been accelerated in the previous half-cycle, and therefore to have non-zero velocity – resulting in a non-trivial phase. This phase can not be described by the field-dressed states defined following above prescriptions.

Let us analyze a few well-known attempts to overcome these problems; a good summary for the case of interband tunneling is [71], where the author also apply them to the calculation of the tunneling rate. Let us consider the Hamiltonian in the length gauge

$$\hat{H} = \hat{H}_0 + E_0 x, \quad (4.42)$$

sometimes called Wannier-Stark Hamiltonian. We notice that the electric field breaks the periodicity of the potential: as a consequence we expect discrete energy levels, and we expect them to depend on the cell index. We will now calculate approximate eigenstates of (4.42), known as Kane states. Let us express a general eigenstate of this Hamiltonian in terms of Bloch states

$$|\zeta\rangle = \sum_n \sqrt{\frac{a}{2\pi}} \int_{-\frac{\pi}{2a}}^{\frac{\pi}{2a}} dk \tilde{\zeta}_n(k) |\theta_n(k)\rangle : \quad (4.43)$$

the sum over  $n$  is necessary because in principle bands are coupled by the field and we can not operate in subspaces of a single band. The substitution of this ansatz into the eigenvalue equation gives

$$\sum_n \int_{-\frac{\pi}{2a}}^{\frac{\pi}{2a}} dk \left[ \mathcal{E}_n^{(0)}(k) + E_0 x \right] \tilde{\zeta}_n(k) |\theta_n(k)\rangle = \sum_n \int_{-\frac{\pi}{2a}}^{\frac{\pi}{2a}} dk \tilde{\zeta}_n(k) \mathcal{E} |\theta_n(k)\rangle, \quad (4.44)$$

where we have indicated with  $\mathcal{E}_n^{(0)}(k)$  the energy structure of the unperturbed Hamiltonian  $H_0$ , i.e. eigenvalues of Bloch states. In order to obtain an equation for the coefficients, we will need the following expression for matrix elements of the field operator:

$$\langle \theta_{n'}(k') | x | \theta_n(k) \rangle = \int_{-\infty}^{\infty} dx e^{-ik'x} u_{n'}(x, k')^* x e^{ikx} u_n(x, k), \quad (4.45)$$

where we have used the explicit form of Bloch states (3.4). We substitute the equality  $x e^{ikx} = -i \frac{d}{dk} e^{ikx}$  and rewrite the equation introducing the derivative of the whole integral:

$$\begin{aligned} \langle \theta_{n'}(k') | x | \theta_n(k) \rangle &= -i \frac{d}{dk} \int_{-\infty}^{\infty} dx e^{-ik'x} u_{n'}(x, k')^* e^{ikx} u_n(x, k) \\ &+ i \int_{-\infty}^{\infty} dx e^{i(k-k')x} u_{n'}(x, k')^* \frac{d}{dk} u_n(x, k). \end{aligned} \quad (4.46)$$

The first term is an internal product of Bloch waves, which are orthonormal. The second term can be written as a sum of integrals in the primitive cell between  $-a/2$  and  $a/2$ : while functions  $u$  are periodic, the exponentials are not and have to be translated. The result of the sum of exponentials is an expression of the Shah function. The final result reads

$$\langle \theta_{n'}(k') | x | \theta_n(k) \rangle = i \delta_{nn'} \frac{d}{dk} \delta(k' - k) + \delta(k' - k) Z_{nn'}(k), \quad (4.47)$$

where delta on the quasi-momentum have periodicity  $\frac{2\pi}{a}$  and we have introduced the quantity

$$Z_{nn'}(k) = \frac{i}{a} \int_{-\frac{a}{2}}^{\frac{a}{2}} dx u_n'(x, k')^* \frac{d}{dk} u_n(x, k). \quad (4.48)$$

Therefore, Eq. (4.44) becomes

$$\left[ \mathcal{E}_n^{(0)}(k) + E_0 \frac{d}{dk} \right] \tilde{\zeta}_n(k) + E_0 \sum_{n'} Z_{nn'}(k) \tilde{\zeta}_{n'}(k) = \mathcal{E} \tilde{\zeta}_n(k). \quad (4.49)$$

We can easily obtain an analytical solution neglecting coupling between different bands, imposing  $Z_{nn'} = 0$  if  $n \neq n'$ . This will also allow us to decouple solutions of the eigenvalue problem (4.43) and look for eigenstates associated with a determined band. The differential equation for coefficients  $\tilde{\zeta}_n(k)$  is

$$\frac{d}{dk} \tilde{\zeta}_n(k) = -\frac{i}{E_0} \left[ \mathcal{E} - \mathcal{E}_n^{(0)}(k) - E_0 Z_{nn}(k) \right] \tilde{\zeta}_n(k), \quad (4.50)$$

with boundary conditions  $\tilde{\zeta}_n(k) = \tilde{\zeta}_n(k + \frac{2\pi}{a})$ . The solution is readily evaluated as

$$\tilde{\zeta}_n(k) = \exp\left[-\frac{i}{E_0} \int_0^k dq \mathcal{E}_{nl} - \bar{\mathcal{E}}_n(q)\right], \quad (4.51)$$

where we have defined  $\bar{\mathcal{E}}_n(k) = \mathcal{E}_n^{(0)}(k) + E_0 Z_{nn}(k)$ . Boundary conditions have provided the quantization of the energy

$$\mathcal{E}_{nl} = E_0 a l + \frac{a}{2\pi} \int_{-\frac{\pi}{a}}^{\frac{\pi}{a}} dq \bar{\mathcal{E}}_n(q) : \quad (4.52)$$

this expression shows the typical Wannier-Stark ladder [50] i.e. a set of energies separated by  $aE_0$ , which is the energy difference between neighboring cells in the presence of the constant electric field  $E_0$ . Resulting functions

$$|\zeta_{nl}\rangle = \sqrt{\frac{a}{2\pi}} \int_{-\frac{\pi}{2a}}^{\frac{\pi}{2a}} dk \tilde{\zeta}_{nl}(k) |\theta_n(k)\rangle \quad (4.53)$$

are called Kane functions [55], they are orthonormal and complete.

There are different ways to adjust these states to the case of a time-dependent electric field. One possibility is to read the eigenvalue equation (4.49) as a Schrödinger equation and write the corresponding time-dependent evolution neglecting inter-band transitions

$$i \frac{d}{dt} \tilde{\zeta}_n(k, t) = \left[ \mathcal{E}_n^{(0)}(k) + E(t) Z_{nn}(k) + E(t) \frac{d}{dk} \right] \tilde{\zeta}_n(k). \quad (4.54)$$

In the case of a constant field, these states are sometimes called Wannier-Stark states: since we have solved the corresponding eigenvalue problem, their time-dependence is easily derived

$$|\zeta_{nl}(t)\rangle = e^{-i\mathcal{E}_{nl}t} |\zeta_{nl}\rangle. \quad (4.55)$$

Using the decomposition of a Bloch state on Kane states

$$|\theta_n(k_0)\rangle = \sum_l \langle \zeta_{nl} | \theta_n(k_0) \rangle |\zeta_{nl}\rangle = \sqrt{\frac{a}{2\pi}} \sum_l \tilde{\zeta}_n(k_0)^* |\zeta_{nl}\rangle, \quad (4.56)$$

we can derive a time-dependent Bloch function at a fixed  $k = k_0$ :

$$|\theta_n(k_0, t)\rangle = \sum_l \exp\left[\frac{i}{E_0} \mathcal{E}_{nl} k_0 - i\mathcal{E}_{nl}t - \frac{i}{E_0} \int_0^{k_0} dq \bar{\mathcal{E}}_n(q)\right] |\zeta_{nl}\rangle. \quad (4.57)$$

On the other hand, we can assume that the quasi-momentum of the electron follows the semiclassical motion (see Eq. (3.15))  $k(t) = k_0 - Et$  and write the corresponding time-dependent Bloch state as

$$|\theta_n(k(t))\rangle = \sum_l \exp\left[\frac{i}{E_0} \mathcal{E}_{nl} k_0 - i\mathcal{E}_{nl}t - \frac{i}{E_0} \int_0^{k(t)} dq \bar{\mathcal{E}}_n(q)\right] |\zeta_{nl}\rangle. \quad (4.58)$$

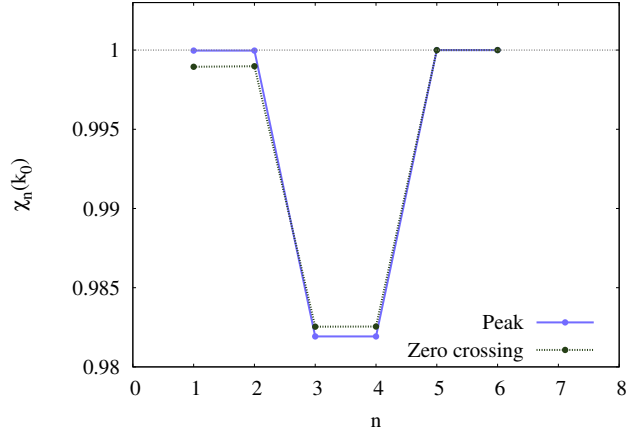


Figure 4.15: **Assessment of accelerated Bloch states.** Figure of merit for accelerated Bloch states relative to different bands  $n$  for two different times: at the peak of the field and at the zero crossing. It is calculated with a laser field intensity  $0.001 \text{ PW/cm}^2$  at  $k_0 = 0.1$ . As expected higher bands are represented almost perfectly: in the limit of the free electron, the description is supposed to be exact. Accelerated Bloch states are not perfect but the small discrepancy is the same at different points of the interaction: this suggests the absence of systematic errors in describing a certain part of the evolution, e.g. when the electron is maximally dislocated or when it has maximum velocity.

Writing the integral in the exponent as

$$\int_0^{k(t)} dq \bar{\mathcal{E}}_n(q) = \int_0^{k_0} dq \bar{\mathcal{E}}_n(q) + \int_0^t dt' \bar{\mathcal{E}}_n(k(t')), \quad (4.59)$$

we can express the time-dependent Bloch state as

$$|\theta_n(k_0, t)\rangle = \exp\left[-i \int_0^t dt' \bar{\mathcal{E}}_n(k(t'))\right] |\theta_n(k(t))\rangle. \quad (4.60)$$

We have obtained a Bloch state with a quasi-momentum which evolves semiclassically, and acquires a phase during the evolution: this kind of state is known in literature under the name of Houston function [72], or accelerated Bloch state. In the next section we will investigate their effectiveness as field-dressed states, and apply them in our numerical calculation.

## 4.5.2 Accelerated Bloch States

Let us consider the following field-dressed states

$$|\xi_n^L(k, t)\rangle = \exp\left[-i \int_{-\infty}^t dt' \mathcal{E}_n(k + A(t'))\right] |\theta_n(k + A(t))\rangle, \quad (4.61)$$

where  $|\theta_n(k)\rangle$  are Bloch states (4.3) and  $A(t)$  is the vector potential of the field. We notice an analogy between these states and Coulomb-Volkov states (1.55). In both cases we start from single-electron eigenstates of an unperturbed Hamiltonian: in the CV case they are Coulomb

wavefunctions, here they are Bloch wavefunctions. We assume that the electron accelerates according to a classical equation of motion, and translate this assumption on the momentum of the Coulomb wave or on the quasi-momentum of the Bloch wave. Accelerated states acquire a time-dependent phase during the acceleration. In both cases we are trying to guess the proper wavefunctions and nothing ensures that they will work as expected; however we are encouraged by the effectiveness of the Coulomb-Volkov approximation in describing electron dynamics.

We will use the field-dressed states to decompose the wavefunction calculated from our numerical tool in the velocity gauge; let us transform them properly

$$|\xi_n(k, t)\rangle = \exp\left[-i \int_{-\infty}^t dt' \mathcal{E}_n(k + A(t'))\right] |\theta_n(k + A(t))\rangle e^{-iA(t)x} e^{\frac{i}{2} \int_{-\infty}^t dt' A^2(t')}. \quad (4.62)$$

All phase factors independent on the coordinate have no effect on determining the probability (4.41), as they are canceled by the modulus. We need to assess the validity of states (4.62) as field-dressed states. They satisfy fundamental requirements: they are orthonormal (follows from orthonormality of Bloch states) and reduce to Bloch states when the field is zero. Orthonormality is necessary for them to provide physical interpretation: for example if at time  $t$  the electron has probability 1 to be in the state  $|\xi_n(k, t)\rangle$ , it must have zero probability to be in any other state. The characteristic which would make them suitable field-dressed state, is their ability to describe the distortion of the field-free states due to the interaction with the field: this consideration implies that for a field low enough not to induce any inter-band transition, the electronic wavefunction  $|\psi(t)\rangle$  should coincide with the field-dressed state at every time  $t$ . We define the figure of merit

$$\chi_n(t) = |\langle \xi_n(k, t) | \psi_k(t) \rangle|^2 \quad (4.63)$$

for an electron which is in the state  $|\theta_n(k)\rangle$  before the interaction with the field. From that we expect  $\chi$  to be equal to 1 during the interaction with a low field. In Fig. 4.15 we show the figure of merit for different starting bands at the peak and at the zero-crossing of the field: there is a small deviation ( $< 2\%$ ) but the overall outcome is quite good. We compare the probability of being in an accelerated Bloch state with that of being in a Bloch state. Let us define the two quantities

$$p_n^\xi(t) = |\langle \xi_n(t) | \psi(t) \rangle|^2 \quad \text{and} \quad p_n^\theta(t) = |\langle \theta_n(t) | \psi(t) \rangle|^2; \quad (4.64)$$

we perform an average over the quasi-momentum  $k$  which is not explicitly written. We know that  $p_n^\theta$  has no physical meaning in the presence of the field, while  $p_n^\xi$  should be close to the actual excitation probability in band  $n$ ; we plot these two quantities in Fig. 4.16. It is difficult to assess whether the predicted excited population is reliable or not; finer comparisons may be possible using the amplitude of quantum beats created by the superposition of conduction and valence band states (see Sec. 4.3).

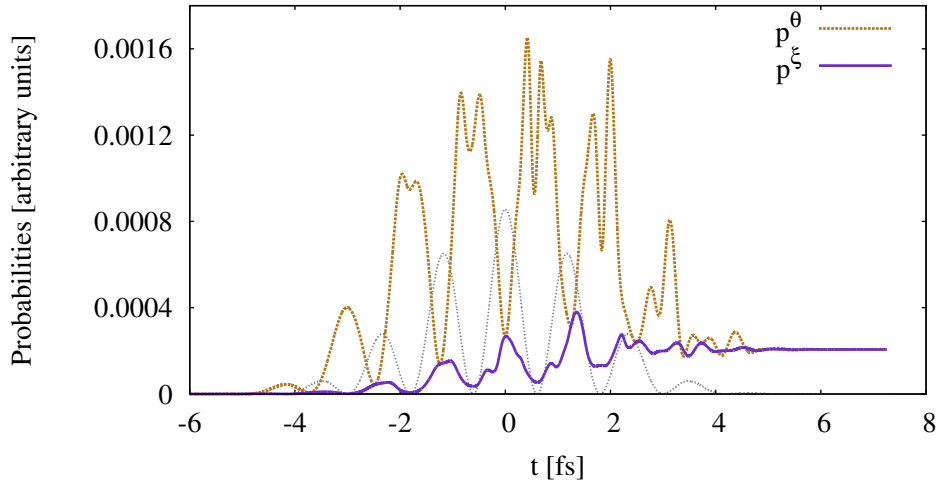


Figure 4.16: **Comparison of Probabilities.** We compare probabilities  $p_n^\xi(t)$  and  $p_n^\theta(t)$  for the first conduction band (i.e.  $n = 2$  in reference to Fig. 4.1): we have used an intensity  $I = 0.03 \text{ PW/cm}^2$  and we have averaged over  $k$  in the first Brillouin zone. The modulus of the electric field is reported for reference (in gray), rescaled to fit into the plot. As expected  $p^\theta$  can not be interpreted as excitation probability during the laser pulse, showing a huge excited population which disappears after the interaction. The projection on accelerated Bloch states is closer to the expected behavior for the excitation: the population grows in steps at maxima of the electric field. The two probabilities are equal at these points, because they correspond to zero-crossings of the vector potential. This cast some doubts about the effectiveness of our field-dressed states, for the same reason discussed at the beginning of Sec. 4.5.1: at maxima of the electric field the electron is displaced from its equilibrium position, and this displacement is not accounted for.



# Conclusions

One achievement of this Thesis – which also made the work more rewarding – was not to limit the research to the application of known algorithms and data analysis for the measurements. The modeling of relevant phenomena and the interpretation of experiments have been fascinating tasks, involving the confrontation with different kinds of problems. This process of analysis has raised fundamental questions and suggested subjects for a deeper theoretical investigation.

We have developed a numerical tool to simulate laser-dressed photionization: it is a working proof that, using proper approximations, it is possible to simulate complicated multi-electron dynamics using just a few dipole matrix elements. In our case, these dipole matrix elements were obtained from advanced atomic structure calculations, accomplished by our collaborators. The model performs pretty well in reproducing results of more elaborate tools: it correctly describes the spectra of ejected electrons, and the delay between ionization channels. Nonetheless, the discrepancy between our estimation and a measurement of this delay remains significant. Independent calculations from different groups tend to validate our prediction, and we are waiting for more refined experiments. We have proceeded in investigating the capabilities of our model, checking whether it is suitable for the calculation of angle-resolved electron spectra. While we confirm that this is indeed the case, we also find that small modifications occurring in the electron distribution due to the laser field are not fully accounted for in our model. This is a limit of the Coulomb-Volkov approximation, which performs otherwise surprisingly well in our case.

Urged on by new exciting experiments, we have focused our research on the inter-band excitation in dielectrics. The first step was implementing a numerical propagator of the TDSE in a lattice potential and use it to simulate the creation and acceleration of charge carriers by means of a strong field. Both theory and experiment show that the induced current has a strong dependence on the characteristics of the pulse. This promises a high degree of control of the signal; at the same time, it also suggests the possibility of solid-state devices to characterize an optical pulse.

Once charge carriers are created, the conduction of current is just one of the drastic changes occurring in the dielectric. We have studied in detail the modifications in the properties of the sample, associating them to the characteristics of excited electrons. We have shown how these effects carry a signature of the excitation process and discussed possible ways how to measure them, and to take advantage of these effects in order to obtain an insight into electron dynamics.

Summarizing, this Thesis is an example of how sometimes it is worth to start from easy things approaching complex problems. Instead of using the most refined algorithm available we have tried to model the relevant features in the simplest way possible. In some case the simple

tool developed worked just fine, beyond the expectations; at other times, we had to improve it or to admit that it was not suitable to describe certain peculiarities. In any case, our analysis provided valuable pictures of dynamics involved and hints about where it is worth to deepen the investigation.

# Bibliography

- [1] E. Goulielmakis, M. Schultze, M. Hofstetter, V. S. Yakovlev, J. Gagnon, M. Uiberacker, A. L. Aquila, E. M. Gullikson, D. T. Attwood, R. Kienberger, F. Krausz, and U. Kleineberg. Single-cycle nonlinear optics. *Science*, **320**(5883):1614–1617, JUN 20 2008.
- [2] T Fuji, J Rauschenberger, A Apolonski, VS Yakovlev, G Tempea, T Udem, C Gohle, TW Hansch, W Lehnert, M Scherer, and F Krausz. Monolithic carrier-envelope phase-stabilization scheme. *OPTICS LETTERS*, **30**(3):332–334, FEB 1 2005.
- [3] A. Wirth, M. Th. Hassan, I. Grguras, J. Gagnon, A. Moulet, T. T. Luu, S. Pabst, R. Santra, Z. A. Alahmed, A. M. Azzeer, V. S. Yakovlev, V. Pervak, F. Krausz, and E. Goulielmakis. Synthesized light transients. *Science*, **334**(6053):195–200, OCT 14 2011.
- [4] L Landau and E Lifshitz. *Quantum Mechanics, Non-Relativistic Theory*. Pergamon Press, 1991.
- [5] B. H. Brandsen and J. Joachain, C. *Quantum Mechanics*. Pearson Prentice Hall, 2000.
- [6] W. Becker, A. Lohr, M. Kleber, and M. Lewenstein. A unified theory of high-harmonic generation: Application to polarization properties of the harmonics. *Phys. Rev. A*, **56**:645–656, Jul 1997.
- [7] M. J. Seaton and G. Peach. The determination of phases of wave functions. *Proc. Phys. Soc.*, **79**:1296, 1962.
- [8] A. Burgess. The determination of phases and amplitudes of wave functions. *Proc. Phys. Soc.*, **81**:442, 1963.
- [9] J. J. Sakurai. *Modern Quantum Mechanics*. Addison Wesley, 1993.
- [10] D M Volkov. *Z. Phys.*, **94**:250, 1935.
- [11] W Gordon. *Z. Phys.*, **40**:117, 1926.
- [12] Manoj Jain and Narkis Tzoar. Compton scattering in the presence of coherent electromagnetic radiation. *Phys. Rev. A*, **18**:538–545, Aug 1978.

- [13] G. Duchateau, E. Cormier, and R. Gayet. Coulomb-volkov approach of ionization by extreme-ultraviolet laser pulses in the subfemtosecond regime. *Phys. Rev. A*, **66**:023412, Aug 2002.
- [14] G Duchateau, C Illescas, B Pons, E Cormier, and R Gayet. Ionization dynamics in interactions of atoms with ultra-short and intense laser pulses. *Journal of Physics B: Atomic, Molecular and Optical Physics*, **33**(16):L571, 2000.
- [15] A. Jaroń, J. Z. Kamiński, and F. Ehlotzky. Stimulated radiative recombination and x-ray generation. *Phys. Rev. A*, **61**:023404, Jan 2000.
- [16] Shu-Min Li, Yan-Gang Miao, Zi-Fang Zhou, Ji Chen, and Yao-Yang Liu. Antihydrogen formation in laser-assisted positron-antiproton scattering. *Phys. Rev. A*, **58**:2615–2616, Sep 1998.
- [17] A S Kornev and B A Zon. Testing of coulomb-volkov functions. *Journal of Physics B: Atomic, Molecular and Optical Physics*, **35**(11):2451, 2002.
- [18] O Smirnova, A S Mouritzen, S Patchkovskii, and M Yu Ivanov. Coulomblaser coupling in laser-assisted photoionization and molecular tomography. *Journal of Physics B: Atomic, Molecular and Optical Physics*, **40**(13):F197, 2007.
- [19] Olga Smirnova, Michael Spanner, and Misha Ivanov. Analytical solutions for strong field-driven atomic and molecular one- and two-electron continua and applications to strong-field problems. *Phys. Rev. A*, **77**:033407, Mar 2008.
- [20] J. Zhou, J. Peatross, M. M. Murnane, H. C. Kapteyn, and I. P. Christov. Enhanced high-harmonic generation using 25 fs laser pulses. *Phys. Rev. Lett.*, **76**:752–755, Jan 1996.
- [21] J. Itatani, F. Quéré, G. L. Yudin, M. Yu. Ivanov, F. Krausz, and P. B. Corkum. Attosecond streak camera. *Phys. Rev. Lett.*, **88**:173903, Apr 2002.
- [22] Y. Mairesse and F. Quéré. Frequency-resolved optical gating for complete reconstruction of attosecond bursts. *Phys. Rev. A*, **71**:011401, Jan 2005.
- [23] Rick Trebino and Daniel J. Kane. Using phase retrieval to measure the intensity and phase of ultrashort pulses: frequency-resolved optical gating. *J. Opt. Soc. Am. A*, **10**(5):1101–1111, May 1993.
- [24] R Trebino. *Frequency-Resolved Optical Gating: The Measurement of Ultrashort Laser Pulses*. Springer, 2002.
- [25] R Kienberger, E Goulielmakis, M Uiberacker, A Baltuska, V Yakovlev, F Bammer, A Scrinzi, T Westerwalbesloh, U Kleineberg, U Heinzmann, M Drescher, and F Krausz. Atomic transient recorder. *Nature*, **427**(6977):817–821, Feb 26 2004.

- [26] J. Gagnon, E. Goulielmakis, and V.S. Yakovlev. The accurate frog characterization of attosecond pulses from streaking measurements. *Applied Physics B: Lasers and Optics*, **92**:25–32, 2008. 10.1007/s00340-008-3063-x.
- [27] M Hentschel, R Kienberger, C Spielmann, GA Reider, N Milosevic, T Brabec, P Corkum, U Heinzmann, M Drescher, and F Krausz. Attosecond metrology. *Nature*, **414**(6863):509–513, NOV 29 2001.
- [28] D. Guénot, K. Klünder, C. L. Arnold, D. Kroon, J. M. Dahlström, M. Miranda, T. Fordell, M. Gisselbrecht, P. Johnsson, J. Mauritsson, E. Lindroth, A. Maquet, R. Taïeb, A. L’Huillier, and A. S. Kheifets. Photoemission-time-delay measurements and calculations close to the  $3s$ -ionization-cross-section minimum in ar. *Phys. Rev. A*, **85**:053424, May 2012.
- [29] M. Schultze, M. Fiess, N. Karpowicz, J. Gagnon, M. Korbman, M. Hofstetter, S. Neppl, A. L. Cavalieri, Y. Komninos, Th. Mercouris, C. A. Nicolaides, R. Pazourek, S. Nagele, J. Feist, J. Burgdoerfer, A. M. Azzeer, R. Ernstorfer, R. Kienberger, U. Kleineberg, E. Goulielmakis, F. Krausz, and V. S. Yakovlev. Delay in photoemission. *Science*, **328**(5986):1658–1662, JUN 25 2010.
- [30] S Zherebtsov, A Wirth, T Uphues, I Znakovskaya, O Herrwerth, J Gagnon, M Korbman, V S Yakovlev, M J J Vrakking, M Drescher, and M F Kling. Attosecond imaging of xuv-induced atomic photoemission and auger decay in strong laser fields. *Journal of Physics B: Atomic, Molecular and Optical Physics*, **44**(10):105601, 2011.
- [31] Cleanthes A. Nicolaides. The state-specific approach to the solution of problems of electronic structure and dynamics involving excited states. *International Journal of Quantum Chemistry*, **60**(1):119–129, 1996.
- [32] U Becker and D A Shirley. *VUV and Soft X-Ray Photoionization*. Plenum Press, 1996.
- [33] L. R. Moore, M. A. Lysaght, J. S. Parker, H. W. van der Hart, and K. T. Taylor. Time delay between photoemission from the  $2p$  and  $2s$  subshells of neon. *Phys. Rev. A*, **84**:061404, Dec 2011.
- [34] A. S. Kheifets and I. A. Ivanov. Delay in atomic photoionization. *Phys. Rev. Lett.*, **105**:233002, Dec 2010.
- [35] C.-H. Zhang and U. Thumm. Electron-ion interaction effects in attosecond time-resolved photoelectron spectra. *Phys. Rev. A*, **82**:043405, Oct 2010.
- [36] Renate Pazourek, Johannes Feist, Stefan Nagele, and Joachim Burgdörfer. Attosecond streaking of correlated two-electron transitions in helium. *Phys. Rev. Lett.*, **108**:163001, Apr 2012.
- [37] Jan Conrad Baggesen and Lars Bojer Madsen. Polarization effects in attosecond photoelectron spectroscopy. *Phys. Rev. Lett.*, **104**:043602, Jan 2010.

- [38] Misha Ivanov and Olga Smirnova. How accurate is the attosecond streak camera? *Phys. Rev. Lett.*, **107**:213605, Nov 2011.
- [39] Eugene P. Wigner. Lower limit for the energy derivative of the scattering phase shift. *Phys. Rev.*, **98**:145–147, Apr 1955.
- [40] C.A.A. de Carvalho and H.M. Nussenzveig. Time delay. *Physics Reports*, **364**(2):83 – 174, 2002.
- [41] V. S. Yakovlev, J. Gagnon, N. Karpowicz, and F. Krausz. Attosecond streaking enables the measurement of quantum phase. *Phys. Rev. Lett.*, **105**:073001, Aug 2010.
- [42] Felix T. Smith. Lifetime matrix in collision theory. *Phys. Rev.*, **118**:349–356, Apr 1960.
- [43] J. Gagnon, E. Goulielmakis, and V.S. Yakovlev. The accurate frog characterization of attosecond pulses from streaking measurements. *Applied Physics B: Lasers and Optics*, **92**:25–32, 2008. 10.1007/s00340-008-3063-x.
- [44] Stefan Neopl. *Attosecond Time-Resolved Photoemission from Surfaces and Interfaces*. PhD thesis, Technische Universität München, 2012.
- [45] J. Feist, S. Nagele, R. Pazourek, E. Persson, B. I. Schneider, L. A. Collins, and J. Burgdörfer. Nonsequential two-photon double ionization of helium. *Phys. Rev. A*, **77**:043420, Apr 2008.
- [46] O. Ghafur, W. Siu, P. Johnsson, M. F. Kling, M. Drescher, and M. J. J. Vrakking. A velocity map imaging detector with an integrated gas injection system. *Review of Scientific Instruments*, **80**(3), MAR 2009.
- [47] MJJ Vrakking. An iterative procedure for the inversion of two-dimensional ion/photoelectron imaging experiments. *Review of Scientific Instruments*, **72**(11):4084–4089, NOV 2001.
- [48] Ashcroft and Mermin. *Solid State Physics*. Thomson Learning, 1975.
- [49] Maxim Durach, Anastasia Rusina, Matthias F. Kling, and Mark I. Stockman. Metallization of nanofilms in strong adiabatic electric fields. *Phys. Rev. Lett.*, **105**:086803, Aug 2010.
- [50] Gregory H. Wannier. Wave functions and effective hamiltonian for bloch electrons in an electric field. *Phys. Rev.*, **117**:432–439, Jan 1960.
- [51] B. E. A. Saleh and M. C. Teich. *Fundamentals of Photonics*. John Wiley & Sons, 1991.
- [52] R. W. Boyd. *Nonlinear Optics*. Academic Press, 2008.
- [53] C. Zener. A theory of the electrical breakdown of solid dielectrics. *Proc. R. Soc. London, Ser. A*, **145**(855):523–529, 1934.

- [54] L.V. Keldysh. Ionization in the field of a strong electromagnetic wave. *Soviet Physics JETP*, **20**(5):1307, 1964.
- [55] E.O. Kane. Zener tunneling in semiconductors. *Journal of Physics and Chemistry of Solids*, **12**(2):181 – 188, 1960.
- [56] A. Schiffrin, T. Paasch-Colberg, N. Karpowicz, V. Apalkov, D. Gerster, S. Mühlbrandt, M. Korbman, J. Reichert, M. Schultze, S. Holzner, J. Barth, R. Kienberger, R. Ernstorfer, V. S. Yakovlev, M. I. Stockman, and F. Krausz. Optical field-induced current in dielectrics. Submitted to Nature.
- [57] M. Schultze, E. Bothschafter, A. Sommer, S. Holzner, M. Schweinberger, W. Fiess, M. Hofstetter, R. Kienberger, V. Apalkov, V. S. Yakovlev, M. I. Stockman, and F. Krausz. Optical field-induced current in dielectrics. Submitted to Nature.
- [58] R. Benzi, S. Succi, and M. Vergassola. The lattice boltzmann equation: theory and applications. *Physics Reports*, **222**(3):145 – 197, 1992.
- [59] Francesco Sottile, Valerio Olevano, and Lucia Reining. Parameter-free calculation of response functions in time-dependent density-functional theory. *Phys. Rev. Lett.*, **91**:056402, Jul 2003.
- [60] M. V. Fischetti, D. J. DiMaria, S. D. Brorson, T. N. Theis, and J. R. Kirtley. Theory of high-field electron transport in silicon dioxide. *Phys. Rev. B*, **31**:8124–8142, Jun 1985.
- [61] H. Bachau, A. N. Belsky, P. Martin, A. N. Vasil’ev, and B. N. Yatsenko. Electron heating in the conduction band of insulators irradiated by ultrashort laser pulses. *Phys. Rev. B*, **74**:235215, Dec 2006.
- [62] E. Gnani, S. Reggiani, R. Colle, and M. Rudan. Band-structure calculations of sio<sub>2</sub> by means of hartree-fock and density-functional techniques. *Electron Devices, IEEE Transactions on*, **47**(10):1795 – 1803, oct 2000.
- [63] S. Zafar, K. A. Conrad, Q. Liu, E. A. Irene, G. Hames, R. Kuehn, and J. J. Wortman. Thickness and effective electron mass measurements for thin silicon dioxide films using tunneling current oscillations. *Applied Physics Letters*, **67**(7):1031–1033, 1995.
- [64] Philip M. Schneider and W. Beall Fowler. Band structure and optical properties of silicon dioxide. *Phys. Rev. Lett.*, **36**:425–428, Feb 1976.
- [65] James R. Chelikowsky and M. Schlüter. Electron states in  $\alpha$ -quartz: A self-consistent pseudopotential calculation. *Phys. Rev. B*, **15**:4020–4029, Apr 1977.
- [66] Gorachand Ghosh. Dispersion-equation coefficients for the refractive index and birefringence of calcite and quartz crystals. *Optics Communications*, **163**(13):95 – 102, 1999.

- [67] K. Yabana, T. Sugiyama, Y. Shinohara, T. Otobe, and G. F. Bertsch. Time-dependent density functional theory for strong electromagnetic fields in crystalline solids. *Phys. Rev. B*, **85**:045134, Jan 2012.
- [68] Thomas Brabec and Ferenc Krausz. Nonlinear optical pulse propagation in the single-cycle regime. *Phys. Rev. Lett.*, **78**:3282–3285, Apr 1997.
- [69] Denys I. Bondar, Wing-Ki Liu, and Gennady L. Yudin. Adaptation of the modified adiabatic approximation to strong-field ionization. *Phys. Rev. A*, **79**:065401, Jun 2009.
- [70] V.S. Yakovlev, M. Korbman, and A. Scrinzi. Dressed bound states for attosecond dynamics in strong laser fields. *Chemical Physics*, 2012. In Press.
- [71] S. Glutsch. Nonresonant and resonant zener tunneling. *Phys. Rev. B*, **69**:235317, Jun 2004.
- [72] W. V. Houston. Acceleration of electrons in a crystal lattice. *Phys. Rev.*, **57**:184–186, Feb 1940.



# Data Archiving

Results of the numerical calculations for the figures appearing in this Thesis can be found on the Data Archive Server of the Laboratory for Attosecond Physics at the Max Planck Institute of Quantum Optics. The paths are given below. Each folder contains the data and a Gnuplot script to produce the figure; the README file contains the location of the source code used to obtain the data and the location of the original output directory of that code.

- **Figure 2.2**  
\$Pictures/Neon/beta  
and  
\$Pictures/Neon/CS
- **Figure 2.3**  
\$Pictures/Delay/GD
- **Figure 2.6**  
\$Pictures/Angular/He
- **Figure 2.8**  
\$Pictures/Angular/cfr\_TDSE
- **Figure 2.10**  
\$Pictures/Angular/distribution
- **Figure 2.11**  
\$Pictures/Angular/mask
- **Figure 4.1**  
\$Pictures/SolidTDSE/bands\_DeepV
- **Figure 4.2**  
\$Pictures/SolidTDSE/Bulk\_Wells
- **Figure 4.3**  
\$Pictures/Steering\_Current/filtering
- **Figure 4.4**  
\$Pictures/Steering\_Current/CEP

- **Figure 4.5**  
\$Pictures/Steering\_Current/regimes
- **Figure 4.7**  
\$Pictures/Steering\_Current/comparison
- **Figure 4.8**  
\$Pictures/Nonlinear\_Polarization/NonIstant\_DeepV
- **Figure 4.9**  
\$Pictures/Nonlinear\_Polarization/timefreq\_DeepV
- **Figure 4.10**  
\$Pictures/Nonlinear\_Polarization/phase\_DeepV
- **Figure 4.12**  
\$Pictures/Transmitted\_Reflected/ERs\_DeepV
- **Figure 4.13**  
\$Pictures/Transmitted\_Reflected/plasma\_freq\_DeepV
- **Figure 4.14**  
\$Pictures/Transmitted\_Reflected/reflectivity\_DeepV
- **Figure 4.15**  
\$Pictures/FieldDressed/overlap
- **Figure 4.16**  
\$Pictures/FieldDressed/probs

# Acknowledgement

First of all, I am grateful to Dr. Vladislav Yakovlev, for the time he dedicated to me and guiding my research, for being always willing to discuss any problem, at any time. What I have learned in these years, I owe it in the first place to him: in the unnumbered times we have addressed a problem together, he has taught me the importance of considering it from different perspectives, and of identifying what is a relevant question and what is not.

I want to express my thanks to Prof. Dr. Ferencz Krausz for giving me the opportunity to work as a PhD student in the outstanding research environment that he has created at the Max Planck Institut für Quantenoptik. Under his direction, frontiers of science are pushed forward everyday, and working here as a theorist is a unique experience.

I would like to thank Dr. Nicholas Karpowicz for his support: thanks to his experience both in experimental and theoretical physics, he was an irreplaceable help. Discussions with him were always valuable and he has supported many of the results presented in this Thesis with his numerical calculations.

I would also like to thank Dr. Justin Gagnon and Dr. Stanislav Kruchinin for sharing with me not just the office, but also their thinkings and interesting discussions.

During the investigation of angular streaking I have worked together with Prof. Dr. Matthias Kling and Dr. Sergey Zherebtsov: their help was fundamental, and I would like to thank them for being patient enough to work with a theorist.

Working in a pleasant and functioning environment makes of course a big difference: I think that Frau Wild is the main person to thank for that, taking care of all the bureaucratic and organizational conditions.

## Michael Korbman

WORK ADDRESS Max-Planck-Institut für Quantenoptik  
Hans-Kopfermann-Straße 1  
D-85748 Garching, Germany

HOME ADDRESS Clemensstraße 16  
D-80803 München, Germany

T +49 176 61597852 – mobile  
T +49 89 32905 637 – work  
F +49 89 32905 649  
✉ [michael.korbman@mpq.mpg.de](mailto:michael.korbman@mpq.mpg.de)

Name: Michael Korbman  
Born: January 7 1985, in Milan, Italy  
Nationality: Italian  
Marital Status: Single  
Driving License: B

### CURRENT POSITION

*Ph.D. candidate*, Max-Planck-Institut für Quantenoptik ([www.mpq.mpg.de](http://www.mpq.mpg.de))

Student of the International Max Planck Research School ([www.mpq.mpg.de/APS](http://www.mpq.mpg.de/APS))

Theoretical and computational physics: • Offering theoretical support to experiments (analysis of the system, software implementation, interpretation of results) • Developing independent research

### AREAS OF SPECIALIZATION

- Skills in problem solving and modeling of complex problems
- Software development
- Implementation of high-level mathematical instruments
- Conversant with state-of-the-art scientific texts
- Active partnership and task planning in a team
- Public speaking and presentation of project results

---

## Education

9/2012 Ph.D. scholarship in theoretical and computational physics.  
↑  
9/2008 Max-Planck-Institut für Quantenoptik, Garching, Germany  
Ludwig-Maximilians-Universität, München, Germany

7/2008 M.Sc. in Physics, curriculum of Condensed Matter Physics  
↑  
10/2006 *Final grade:* 110/110 cum laude  
Università degli Studi di Milano, Milan, Italy

7/2006 Bachelor in Physics  
↑  
10/2003 *Final grade: 110/110 cum laude*  
Università degli Studi di Milano, Milan, Italy

---

## Publications

---

- A. Schiffrin, T. Paasch-Colberg, N. Karpowicz, V. Apalkov, D. Gerster, S. Mühlbrandt, M. Korbman, J. Reichert, M. Schultze, S. Holzner, J. Barth, R. Kienberger, R. Ernstorfer, V. S. Yakovlev, M. I. Stockman, and F. Krausz. *Optical field-induced current in dielectrics*. Submitted to Nature.
- 1/2012 V.S. Yakovlev, M. Korbman, and A. Scrinzi. *Dressed bound states for attosecond dynamics in strong laser fields*. Chemical Physics, in press.
- 5/2011 S. Zherebtsov, A. Wirth, T. Uphues, I. Znakovskaya, O. Herrwerth, J. Gagnon, M. Korbman, V. S. Yakovlev, M. J. J. Vrakking, M. Drescher, and M. F. Kling. *Attosecond imaging of xuvinduced atomic photoemission and auger decay in strong laser fields*. J. Phys. B **44** 105601 (2011).
- 6/2010 M. Schultze, M. Fiess, N. Karpowicz, J. Gagnon, M. Korbman, M. Hofstetter, S. Neppl, A. L. Cavalieri, Y. Komninos, Th. Mercouris, C. A. Nicolaides, R. Pazourek, S. Nagele, J. Feist, J. Burgdorfer, A. M. Azzeer, R. Ernstorfer, R. Kienberger, U. Kleineberg, E. Goulielmakis, F. Krausz, and V. S. Yakovlev. *Delay in photoemission*. Science, **328** 1658 (2010).
- 10/2008 C. Invernizzi, M. Korbman, L. Campos Venuti and M. G. A. Paris. *Optimal quantum estimation in spin systems at criticality*. Phys. Rev. A **78**, 042106 (2008).
- 4/2007 L. Salasnich, N. Manini, F. Bonelli, M. Korbman, and A. Parola. *Self-induced density modulations in the free expansion of Bose-Einstein condensates*. Phys. Rev. A **75**, 043616 (2007).

---

## Computer skills

---

- Operating systems: GNU/Linux, Windows
- Programming languages: C++, Python, Bash
- Tools: Microsoft Office, Mathematica,  $\LaTeX$ , GNUPlot, Gimp, Inkscape

---

## Language skills

---

- **English**: fluent (CEF level: C1 / C2). Worked in English in the last four years.  
12/2007 TOEFL overall grade: 103/120
- **German**: good (CEF level: B2), learned in Germany. Accustomed to everyday conversations.
- **Italian**: native speaker

---

## Other Activities

---

Active contribution in the organization of a conference with international speakers (IMPRS interdisciplinary symposium 2010) • Private lessons for high school students • Climbing • Swimming • Playing piano



